High Angular Resolution Radio Observations of Luminous Infrared Galaxies

Submitted by

Naím Ramírez Olivencia

Thesis Advisor

Dr. Miguel Ángel Pérez Torres
Dr. Antonio María Alberdi Odriozola

Departamento de Radioastronomía y Estructura Galáctica

A thesis submitted to the Universidad de Granada in fulfillment of the requirement for the degree of Doctor of Physics and Mathematics.
Programa de Doctorado en Física y Matemáticas

UNIVERSIDAD DE GRANADA

2021

Editor: Universidad de Granada. Tesis Doctorales
Autor: Naím Ramírez Olivencia
ISBN: 978-84-1306-949-4
URI: http://hdl.handle.net/10481/69673

Abstract

Departamento de Radioastronomía y Estructura Galáctica

Doctor of Physics and Mathematics

High Angular Resolution Radio Observations of Luminous Infrared Galaxies

by Naím Ramírez Olivencia

El objetivo general de esta tesis ha sido mejorar nuestra comprensión de los procesos de emisión y absorción en radio que tienen lugar en las galaxias luminosas y ultraluminosa en el infrarrojo (U/LIRGs) del universo local, utilizando radiointerferómetros de última generación que ofrecen una alta resolución angular (mejor que 1 segundo de arco) y gran sensibilidad en múltiples frecuencias. Estas observaciones radiointerferométricas permiten caracterizar la distribución de energía espectral en el rango de frecuencias de GHz, donde se sabe que la emisión sincrotrón, así como la emisión térmica libre-libre, contribuyen de modo significativo (Condon, 1992).

He presentado resultados de la muestra e-MERLIN LIRGI, cuyo objetivo global es caracterizar la evolución fenomenológica del núcleo de un brote de formación estelar (starburst). Uno de los objetivos inmediatos es desvelar la fuente responsable del calentamiento del polvo y el gas en las regiones nucleares de estas galaxias (AGN o brote de formación estelar). Aunque aquí presentamos resultados preliminares de LIRGI en la banda de 5 GHz, los resultados evidencian el enorme potencial del uso de la radiointerferometría con resoluciones mejores que el segundo de arco para el estudio de brotes y regiones nucleares en el universo local.

En la primera parte de este trabajo realizamos un estudio exhaustivo de la LIRG Arp 299, donde presentamos las primeras combinando observaciones del Jansky Very Large Array (JVLA) a frecuencias entre 1.4 y 8.4 GHz con las primeras observaciones de esta LIRG obtenidas con el LOw Frequency ARray (LOFAR), incluyendo las estaciones internacionales. Este trabajo engloba un estudio detallado del campo magnético, la *emission measure* y por lo tanto su correspondiente densidad electrónica, de su índice espectral, y de las características estructurales de los regiones nucleares de Arp 299 a estas frecuencias.

Uno de los resultados más importantes obtenidos a partir de las observaciones de LOFAR, en combinación las del JVLA a varias frecuencias, es la caracterización del medio interestelar en los núcleos de las LIRGs. Para ello, ajustamos la distribución espectral de energía de los núcleos, entre 150 MHz y 8.4 GHz, utilizando dos modelos diferentes del gas térmico absorbente/emisor: en uno de los modelos, las partículas emisoras/absorbentes están distribuidas de modo uniforme (modelo continuo) (Condon, 1992), mientras que en el segundo se supone un medio con grumos (Conway, Elitzur, and Parra, 2018), donde la distribución del gas no es uniforme. Ambos modelos ajustan bien los datos existentes. El modelo continuo puede explicar la SED de los núcleos con una población estándar de electrones relativistas sometidos a pérdidas por sincrotrón, Bremsstrahlung e ionización , que se esperan sean significativas debido a las grandes densidades encontradas en las regiones centrales de las U/LIRG (Lacki, Thompson, and Quataert, 2010). El modelo de grumos puede explicar los datos mediante una población de electrones relativistas con pérdidas de energía insignificantes, y

predice fracciones térmicas que son más típicas de las galaxias con formación estelar, en comparación con el modelo continuo. Nosotros proponemos observaciones con LOFAR a frecuencias menores de 100 MHz, o bien observaciones con el uGMRT a $\sim$600 MHz para discernir entre ambos modelos. En cualquier caso, estos resultados ponen de manifiesto la relevancia de las observaciones de baja frecuencia y alta resolución angular para trazar el medio interestelar difuso en galaxias.

En la segunda parte de la tesis he abordado el estudio de las propiedades físicas de la muestra LIRGI, así como de la caracterización de los procesos de emisión y absorción en galaxias locales, donde podemos hacerlo con extraordinario detalle. Esto nos permitirá comprender mejor las propiedades de las galaxias con brotes de formación estelar a distancias cosmológicas (Magnelli et al., 2009), donde sabemos que fueron mucho más abundantes, pero la resolución angular no permite resolver las estructuras con el adecuado detalle.

Por último, he estudiado la función de luminosidad de los remanentes de supernova (SNR) en galaxias normales (Chomiuk and Wilcots, 2009), con el objetivo de construir una función de luminosidad universal. Para ello, escribí un código que utiliza un tamaño no uniforme del ”bin”, lo que evita introducir sesgos en el estudio debido al pequeño tamaño de algunas muestras de SNR. El resultado principal es la obtención de un nuevo (verdadero) límite de completitud en la muestra global debido a la presencia de galaxias con estallido de estrellas.

The overall goal of this thesis has been to improve our understanding of the radio emission and absorption processes taking place in luminous and ultra-luminous infrared galaxies (U/LIRGs) in the local Universe, using state-of-the-art radio interferometers that offer high angular resolution (better than 1 arcsecond) and sensitivity at multiple frequencies. These radio interferometric observations allow us to characterise the spectral energy distribution in the GHz frequency range, where synchrotron emission, as well as free-free thermal emission, is known to contribute significantly (Condon, 1992).

I have presented results from the e-MERLIN LIRGI sample, whose overall objective is to characterise the phenomenological evolution of the core of a starburst. One of the immediate goals is to reveal the source responsible for the heating of the dust and gas in the nuclear regions of these galaxies (AGN or starburst). Although we present here preliminary results from LIRGI in the 5 GHz band, the results show the enormous potential of using radio interferometry at resolutions better than arcsecond to study outbursts and nuclear regions in the local Universe.

In the first part of this paper we made a comprehensive study of the LIRG Arp 299, where we present the first observations of this LIRG from the Jansky Very Large Array (JVLA) at frequencies between 1.4 and 8.4 GHz combined with the first observations of this LIRG obtained with the LOw Frequency ARray (LOFAR), including the international stations. This work has included a study of its magnetic field, of its emission measure and therefore its corresponding electron density, of its spectral index, and of its structural characteristics at these frequencies.

One of the most important results obtained from LOFAR observations, in combination with JVLA observations at various frequencies, is the characterisation of the interstellar medium in the cores of LIRGs. For this purpose, we fit the spectral energy distribution of the cores, between 150 MHz and 8.4 GHz, using two different models of the absorbing/emitting thermal gas: in one model, emitting/absorbing particles are uniformly distributed (continuous model) (Condon, 1992), while in the second one we assume a clumpy medium (Conway, Elitzur, and Parra, 2018), where there is a non-uniform distribution. Both models fit the existing data well. The continuum model can account for the SED of nuclei with a standard population of relativistic electrons subject to synchrotron, Bremsstrahlung and ionisation losses, which are expected to be significant due to the large densities found in the central regions of the U/LIRGs (Lacki, Thompson, and Quataert, 2010). The clumpy model can explain the data by a relativistic electron population with negligible energy losses, and predicts thermal fractions that are more typical of star-forming galaxies, compared to the continuum model. We propose LOFAR observations at frequencies below 100 MHz, or uGMRT

observations at ∼600 MHz to discern between the two models. In any case, these results highlight the relevance of low-frequency, high angular resolution observations for tracing the diffuse interstellar medium in galaxies.

In the second part of the thesis I have addressed the study of the physical properties of the LIRGI sample, as well as the characterisation of the emission and absorption processes in local galaxies, where we can do so in extraordinary detail. This will allow us to better understand the properties of galaxies with outbursts of star formation at cosmological distances (Magnelli et al., 2009), where we know that they were much more abundant, but the angular resolution does not allow us to resolve the structures in adequate detail.

Finally, I studied the supernova remnant luminosity function (SNR) in normal (Chomiuk and Wilcots, 2009) galaxies, with the aim of constructing a universal luminosity function. To do so, I wrote a code that uses a non-uniform bin size, which avoids introducing biases in the study due to the small size of some SNR samples. The main result is to obtain a new (true) completeness limit on the global sample due to the presence of starburst galaxies.

Publications

1. MATTILA, S.; PÉREZ-TORRES, M.; EFSTATHIOU, A.; MIMICA, P.; FRASER, M.; KANKARE, E.; ALBERDI, A.; ALOY, M. Á.; HEIKKILÄ, T.; JONKER, P. G.; LUNDQVIST, P.; MARTÍ-VIDAL, I.; MEIKLE, W. P. S.; ROMERO-CAÑIZALES, C.; SMARTT, S. J.; TSYGANKOV, S.; VARENIUS, E.; ALONSO-HERRERO, A.; BONDI, M.; FRANSSON, C. HERRERO-ILLANA, R.; KANGAS, T.; KOTAK, R.; **RAMÍREZ-OLIVENCIA, N.**; VÄISÄNEN, P.; BESWICK, R. J.; CLEMENTS, D. L.; GREIMEL, R.; HARMANEN, J.; KOTILAINEN, J.; NANDRA, K.; REYNOLDS, T.; RYDER, S.; WALTON, N. A.; WIIK, K.; ÖSTLIN, G. (2018). A dust-enshrouded tidal disruption event with a resolved radio jet in a galaxy merger. Sci, 361, 482

2. **RAMÍREZ-OLIVENCIA, N.**; VARENIUS, E.; PÉREZ-TORRES, M.; ALBERDI, A.; PÉREZ, E.; ALONSO-HERRERO, A.; DELLER, A.; HERRERO-ILLANA, R.; MOLDÓN, J.; BARCOS-MUÑOZ, L.; MARTÍ-VIDAL, I. (2018). Sub-arcsecond imaging of Arp299-A at 150 MHz with LOFAR: Evidence for a starburst-driven outflow. A&A, 610L,18R

3. CICONE, C.; BOTHWELL, M.; WAGG, J.; MØLLER, P.; DE BREUCK, C.; ZHANG, Z.; MARTÍN, S.; MAIOLINO, R.; SEVERGNINI, P.; ARAVENA, M.; BELFIORE, F.; ESPADA, D.; FLÜTSCH, A.; IMPELLIZZERI, V.; PENG, Y.; RAJ, M. A.; **RAMÍREZ-OLIVENCIA, N.**; RIECHERS, D.; SCHAWINSKI, K. (2017). The final data release of ALLSMOG: a survey of CO in typical low-M_* star-forming galaxies. A&A, 604, 53.

4. VARENIUS, E.; CONWAY, J. E.; MARTÍ-VIDAL, I.; AALTO, S.; BARCOS-MUÑOZ, L.; KÖNIG, S.; PÉREZ-TORRES, M. A.; DELLER, A. T.; MOLDÓN, J.; GALLAGHER, J. S.; YOAST-HULL, T. M.; HORELLOU, C.; MORABITO, L. K.; ALBERDI, A.; JACKSON, N.; BESWICK, R.; CAROZZI, T. D.; WUCKNITZ, O.; **RAMÍREZ-OLIVENCIA, N.** (2016). Subarcsecond international LOFAR radio images of Arp220 at 150MHz. A kpc-scale star forming disk surronding nuclei with shocked outflows. A&A, 593, 86.

In preparation:

5. **RAMÍREZ-OLIVENCIA, N.**; PÉREZ-TORRES, M.A.; ALBERDI, A. A useful approximation to a small sample in SNR LFs. *In preparation.*

6. **RAMÍREZ-OLIVENCIA, N.**; VARENIUS, E.; PÉREZ-TORRES, M.A.; ALBERDI, A; CONWAY, J.E.; ALONSO-HERRERO, A.; PEREIRA-SANTAELLA, M.; HERRERO-ILLANA, R. Subarcsecond LOFAR imaging of Arp299 at 150MHz. Tracing the nuclear and diffuse extended emission of a bright LIRG *Working on referee's comments*

Acknowledgements

Querría empezar mis agradecimientos desde el principio. Gracias Juan Carlos (mi querido Petete, profesor de Física) por haber sabido trasmitirme la curiosidad por un mundo (un Universo) tan apasionante como la Física cuando estaba en Bachillerato. Durante el eclipse anular de 2005 me enteré de que eras astrofísico y desde entonces supe que quería ser como tú.

Mi total agradecimiento a mis profesores de la especialidad de Astrofísica en la Universidad Complutense de Madrid durante mi feliz andadura por la carrera de Física. Especialmente quiero agradecer a Pablo Pérez González, que aparte de mi profesor, fue mi director de trabajo fin de máster. Gracias por esas clases tan maravillosas, esas explicaciones tan claras, y esa exigencia tan alta. Precisamente tú, con todo lo que nos dabas, podías pedirnos el máximo esfuerzo. También gracias por tu paciencia durante mi trabajo fin de máster. Gracias también a mis amigos, especialmente a David, Nuria, Javi, Marcos, Alberto, Alicia, Manu, Bernardo, Irene, por haber sido los perfectos compañeros de batallas y de alegrías.

Thanks also to Alexander Knebe, professor at the Universidad Autónoma de Madrid, who supported me during my master's degree and did everything possible so that I could do my PhD with him in his beautiful dark matter simulations. In the end, as sometimes happens, money is an impediment to everything. Still, I am very glad to have met you and to have felt your support.

Ahora llego a una de mis partes favoritas, que es agradecer infinitamente a mis directores de tesis, Miguel y Antxon, todo lo que me han dado durante esta etapa de doctorado. Gracias primeramente por vuestra estupenda organización, por haberme dado la oportunidad de aprender tantísimo con los cursos, congresos, pedidas de tiempo, etc. Ha sido todo un regalo continuo. Gracias por haberme dado la confianza para liderar artículos y observaciones, y por animarme cuando las cosas no salían bien. Y profundamente gracias por este último tiempo tan difícil de doctorado, en el que habéis sabido tener paciencia y cariño infinitos conmigo. Cuando llegué al IAA y comenté que vosotros érais mis directores me dijeron que eráis los mejores. A día de hoy lo corroboro y doblo la apuesta.

Gracias a mis amigos y compañeros del IAA. Gracias a Pablo, Javi, Soomin, Víctor, Fran, Salva y Antonio. Habéis sido parte fundamental en mi buen hacer del doctorado porque tras hablar con vosotros de cualquier cosa, volvía con fuerzas renovadas al trabajo. Me encantaba vuestra compañia y poder charlar largo y tendido de todo, ¡incluído de ciencia!. Tengo tres menciones especiales. La primera es para Clara: mil gracias por ser como eras y servirme de modelo a seguir en tantas cosas. La segunda

para mi querida Estela, amiga desde la carrera. Me alegro mucho de que tu trabajo se esté viendo recompensado, te lo mereces. Y por último... para Estefanía, mi amiga, mi compañera de aventuras en el IAA. No hace falta que te diga que mi paso por el IAA no habría sido lo mismo sin ti. Eres muy especial para mí.

Gracias a J. Moldón por este último tiempo que se ha prestado en ayudarme con y asesorarme sobre todo lo relacionado con eMERLIN-LIRGI. Quiero agradecer también a mis compañeros de mi grupo Joel, Mónica y Francesco, por hacer el ambiente de trabajo tan respirable y ser todos unos ejemplos para seguir en mi trabajo. Y sobre todo gracias Rubén, mi hermano mayor de tesis, por todo el apoyo durante este tiempo. Dejaste el listón muy alto, bandido.

I would also like to say a word of thanks to my hosts on my most important journeys. Thank you Rob Beswick and Megan Argo for hosting me at the University of Manchester and teaching me everything you knew about eMERLIN. A very special thanks to Eskil, for his support in Onsala, for his professionalism, his great ability to teach others by making everything seem simple (when it is not), for his dedication and attention to me, and for his moral support in difficult times. Apart from a collaborator, I am taking a great Swedish friend with me. Tack så mycket!

También del IAA, agradecer al servicio de seguridad, por su amabilidad y cercanía. Cómo no agradecer a Ana su especial dedicación y amistad mientras trabajó allí. Al personal de limpieza, siempre tan profesionales, prudentes y amables. Gracias también a Paco, el antiguo conserje. Se jubiló una parte muy entrañable del IAA. También agradecer a toda la parte de administración por su trabajo, especialmente a Francisco Tapia y a Cristina, que de tantos apuros administrativos me han sacado.

Gracias a mis hermanos de comunidad de Granada, que tanto se han preocupado y rezado por mí para poder llegar al día de escribiendo estas líneas. Habéis seguido esta historia como si hubiera sido también vuestra y he sentido vuestro apoyo, incluso en la distancia. Gracias también a mi nueva comunidad de Lucena, que con el poco tiempo que llevamos, ya he visto cómo habéis entrado en la dinámica de sufrir también mis angustias y alegraros con mis alegrías de este tiempo de tesis. Sois la comunidad que necesitaba, está claro.

Y ahora, la que es sin lugar a dudas la parte más difícil por la dificultad de expresar en pocas líneas el agradecimiento que siento. Empiezo. Gracias Paco y Sierri, mis suegros, sobre todo por este último y tan intenso tiempo de tesis en el que os habéis volcado completamente en todo lo que he necesitado para tener tiempo y terminar. Gracias, gracias, e infinitas gracias papá y mamá. Por todo. Pero en cuanto a la tesis, por haberme apoyado siempre, desde que tengo uso de razón, por haber creído en mí

aun cuando yo no veía nada. Obviamente sabéis que sin vuestro apoyo no habría llegado hasta aquí. Gracias también por este último tiempo de sobreesfuerzo en el que me habéis ayudado tanto. Nunca os lo podré agradecer lo suficiente. Gracias, Samuel y Rodrigo, porque sin ser vosotros culpables de nada, habéis tenido que aguantar los nervios que le generaban a vuestra madre esta última etapa de tesis. Gracias porque, aunque sois pequeños, habéis entendido que vuestra mamá necesitaba trabajar mucho y no podía tener tanto tiempo para vosotros. Ahora vienen los buenos tiempos. Espero que esto os sirva como ejemplo en un futuro para no abandonar vuestras metas, por muy inalcanzables que parezcan. También agradecer al que viene que, sin ser consciente de nada, ya ha hecho en mí lo suficiente como para forzarme en acabar sin demasiados nervios para cuidarle, para desear todavía con más ganas terminar para poder disfrutarle mientras aún crece dentro de mí.

Y ...gracias Jesús, mi marido, mi amigo, mi compañero. Qué difícil me resulta escribirte esto y expresar mi agradecimiento. Se me hace pequeño. Gracias primero por haber sabido trasmitirme tu curiosidad científica, que tanto he admirado de siempre. Gracias por haberme apoyado desde que tenía que elegir carrera, sin dudar ni un momento en mis capacidades. Gracias por haberte venido sin pensarlo a Granada, aunque supusiera un parón en tu carrera profesional. Gracias por este último tiempo tan difícil en el que has sido mi principal bastón, por haberme aguantado los nervios y el desánimo por la tesis. Gracias por sentirte orgulloso de mí y disfrutar de mi felicidad ahora. No hace falta que te diga lo mucho que te quiero.

Y por último, lo más importante. Todas las gracias que he dado antes, todas las situaciones vividas que me han llevado hasta terminar esta tesis, se resumen en un solo agradecimiento: gracias Señor. Tú sabrás por qué me permitiste llegar hasta aquí. Sabes que has sido el último hilo al que me aferraba cuando quería dejar este precioso proyecto. Este trabajo, desde mi pequeñez, va dedicado a ti, Señor.

Contents

List of Figures

List of Tables

List of Abbreviations

U/LIRG	**U**ltra/BLuminous **I**nfra**r**ed **G**alaxy
JVLA	**J**ansky **Very** **L**ong **B**aseline
EVN	**E**uropean **V**LBI **Network**
eMERLIN	**e**nhanced **M**ulti **E**lement **R**emotely **L**inked **I**nterferometer **N**etwork
VLBI	**V**ery **L**ong **B**aseline **I**nterferometer
LOFAR	**LO**w **F**requency **AR**ray
RFI	**R**adio **F**requency **I**nterference
SFHU	**S**tar **F**ormation **H**istory of the **U**niverse
IR	**I**nfra**r**ed
FIR	**F**ar **I**nfra**R**ed
SNR	**S**uper**n**ova **R**emnant
AGN	**A**ctive **G**alactic **N**uclei
CR	**C**osmic **Ra**y
FWHM	**F**ull **W**idth **H**alf **M**aximum
FIR	**F**ar **I**nfra**r**ed
HBA	**H**igh **B**and **A**rray
LBA	**L**ow **B**and **A**rray
SMBH	**S**uper**m**assive **B**lack **H**ole
MHD	**M**agneto **H**ydro **D**ynamic
ISM	**I**nter**s**tellar **M**edium
SKA	**S**quare **K**ilometer **Array**
CCSe	**C**ore **C**ollapse **S**upernovae
TDE	**T**idal **D**isruption **E**vent
LIRGI	**L**uminous **I**nfra**r**ed **G**alaxy **I**nventory
CSM	**C**ircum**S**tellar **M**edium
LF	**L**uminosity **F**unction
GOALS	**G**reat **Observatories** **A**ll-sky **L**IRG **S**urvey

De Su Obra, a través de Su Gracia, para Su Gloria

1 Introduction

LOOKING at a clear and non-contaminated sky, our eyes discern an immeasurable number of objects, most of them belonging to the Milky Way, which is also traced as an elongated bright and dark cloud plenty of stars that crosses the sky. The detection of galaxies with the naked eye is, however, complicated at the very least, if not impossible in most cases. M31, commonly known as Andromeda, is one of the most easily observable galaxies in the Northern Hemisphere. If we were able to observe it in the whole frequency range, not just the optical, its apparent magnitude would increase by less than 20%. Now, consider that some galaxies emit such an enormous quantity of **I**nfra**r**ed (**IR**) light that overcomes the total energy at all other frequencies combined. If Andromeda would have this IR luminosity, but only in the optical, its apparent magnitude would increase by about 140%, reaching the apparent magnitude of the Sirius star. These extreme IR emitters are the so call **U**ltra/**L**uminous **I**nfra**r**ed **G**alaxies (**U/LIRGs**) and they are the main pillar of the present Thesis. The huge IR emission of U/LIRGs mainly originates from heated dust, which hides everything beyond it at optical wavelengths. Fortunately, radio wavelengths come to our aid, as they are not affected by dust absorption, and it is possible to observe radio from the Earth because our atmosphere is also transparent to these wavelengths (Fig. 1.1).

1.1 Ultra/Luminous Infrared Galaxies

Before the first IR observations were performed (Johnson, 1966), U/LIRGs were unknown to astronomers. During the 70's-80's, U/LIRGs were widely detected and catalogued as such, and started to be a very common source. U/LIRGs are so bright at

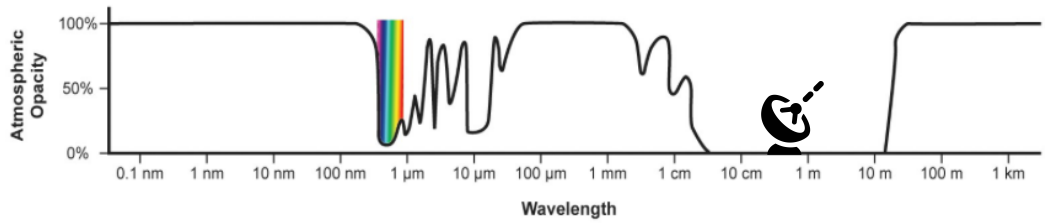

FIGURE 1.1: Scheme of the atmosphere opacity (y-axis) at any wavelength (x-axis). The optical range is represented by a vertical rainbow, and the radio window is observed between the centimetre (cm) and the millimetre (m) regime, which is pinpointed with an antenna symbol.

IR wavelengths that overcome the rest of the energy in the other bands (Sanders and Mirabel, 1996). The process behind this extremely high IR emission is dust heating. This heating might be caused by different scenarios: the presence of an **A**ctive **G**alactic **N**ucleus (**AGN**), the presence of star formation bursts (Farrah et al., 2003), or a combination of both. When an AGN becomes active, the disk emits abundant UV emission. The UV photons heat the nuclear dust in the torus, and this light is re-emitted in the IR. However, a starburst can mimic this behaviour. Indeed, in a starburst, very young, massive stars (and supernovae) emit large amounts of UV photons, heating the surrounding dust, which re-emits this energy at IR wavelengths. These massive stars have very short lifetime, up to a few tens of million years, so any indirect measure of their presence is a very recent tracer of star formation. Therefore, high IR emission in a galaxy is indicative of a very recent and intense burst of star formation (in the absence of an AGN).

I note than in this thesis, L_{IR} refers to the (total) infrared emission between 8 - 1000μm, which we have obtained by using the following expression:

$$L_{IR}(8 - 1000\mu m) = 4\pi D_L^2 F_{IR}(L_\odot), \tag{1.1}$$

where

$$F_{IR} = 1.8 \times 10^{-14}(13.48 f_{12} + 5.16 f_{25} + 2.58 f_{60} + f_{100}) W\, m^{-2} \tag{1.2}$$

is the infra-red flux density from IRAS data. D_L is the luminosity distance, and f_{12}, f_{25}, f_{60} and f_{100} are the flux densities at 12, 25, 60 and 100 μm in Jy, respectively, from IRAS data (Sanders and Mirabel, 1996). When L_{IR} is between $10^{11} L_\odot$ and $10^{12} L_\odot$, we refer to that galaxy as a LIRG, while if L_{IR} is above $10^{12} L_\odot$, the galaxy is a ULIRG.

High-luminosity LIRGs and essentially all ULIRGs are mostly disrupted galaxies, or interacting galaxies in a merger or post-merger state. The merger scenario produces

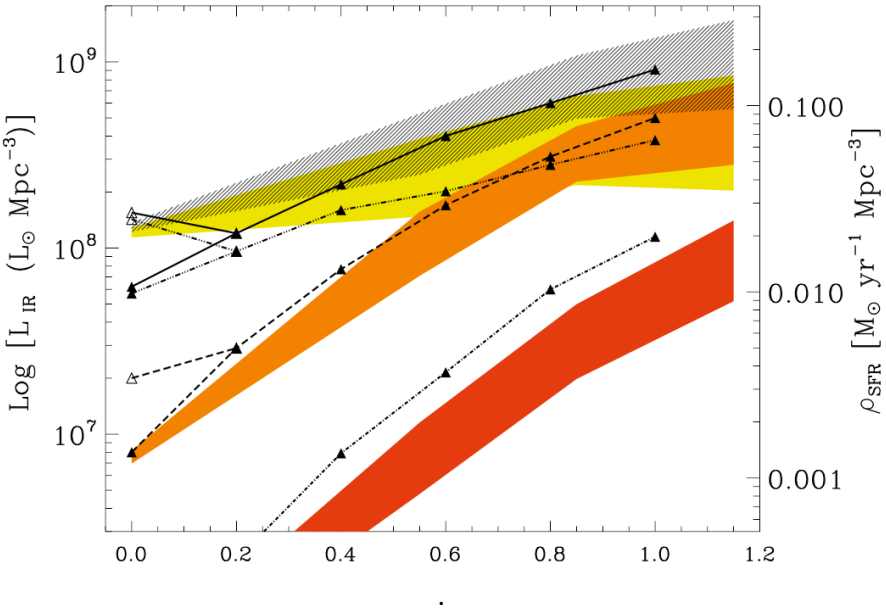

FIGURE 1.2: Figure from Magnelli et al. (2009). Stripped band correspond to the total comoving IR density contribution in the Universe along the redshift. Yellow, orange and red are the contribution of normal galaxies, LIRGs and ULIRGs, respectively. For deeper explanation, consult the reference (Magnelli et al., 2009)

in general angular momentum losses in the nuclei of the galaxies, and favour nuclear star formation, especially when the masses of both galaxies are similar (Cox et al., 2008). Although U/LIRGs are very rare locally (see e.g. Lagache, Puget, and Dole 2005), they start to increase their IR contribution and star formation density, and start to dominate beyond z$\sim$1.2 (Fig. 1.2, Magnelli et al. 2009). Thus, the study of local U/LIRGs is expected to contribute to understand the evolution of galaxies at high z, where sources with that behaviour were predominant and crucial in the star formation.

1.2 Radio Spectral Energy Distribution

The main processes that drive the Universe are star formation and accretion. Accretion is one of the most powerful energy sources in Universe, whereas star formation is responsible for the formation and evolution of galaxies. Radio observations are able to extract important information of both processes. Basically, radio emission may be split into two main mechanisms: thermal and non-thermal radiation. Thermal emission is produced by the interaction of electrons in a medium without being captured by ions or colliding with other electrons. It is called thermal because the electrons embedded on this medium are in thermal equilibrium, and the temperature of the emission and of the

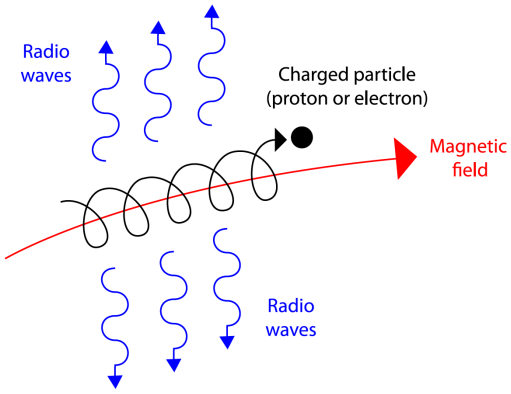

FIGURE 1.3: Schematic motion of a charged particle (black line) in the presence of a magnetic field (red line). The particle is forced to follow the magnetic field lines in a helical trajectory, and this continuous acceleration makes the particle emit synchrotron radiation (blue line).

body are the same, T. The emitting source is therefore a blackbody and, since particles are free and not energy quantified, the emission will produce a continuum spectrum in energy, according to Planck's law. For a blackbody at a given temperature, the intensity of the energy distribution of the emission peaks at a certain ν (Wien's law). In the radio, where the photon energy, $h\,\nu$, is much less than $k\,T$, and the intensity of the emission decreases with the square of the frequency, $B_\nu \propto \nu^{-2}$ (Rayleigh-Jeans law).

Besides thermal radio emission, there are also other mechanisms of non-thermal nature. In particular, synchrotron emission is the principal non-thermal emitting mechanism at GHz and sub-GHz frequencies. Synchrotron emission is produced by relativistic particles (also referred in the present work as **C**osmic **R**ays, **CRs**) in a magnetic field (see Fig. 1.3). Synchrotron also emits in a wide, continuum range of frequencies, and is usually characterized by a (brightness) temperature, T, even though the emission is no longer related to the temperature of the body. Charged particles will gyrate, in the presence of a magnetic field, around the magnefic field lines due to the Lorentz force, and hence will emit as they are being continuously accelerated. In the case of relativistic particles, this non-thermal emission is known as synchrotron emission.

The synchrotron luminosity can be written as follows

$$L = \frac{4Z^4e^4B^2\gamma^2v^2}{9c^5m^2} == \frac{4Z^4e^4B^2E^2}{9m^4c^7} \tag{1.3}$$

Since m_p/m_e=1836, for the same particle velocity, the luminosity ratio between protons and electrons is 3×10^{-7}. On the other hand, if we assume the same energy for both particle, i.e. slower motion for protons, the ratio increase to 9×10^{-14}. Therefore, (relativistic) electrons are the only relevant particles that produce significant synchrotron

emission. In this Thesis, I will consider just electrons, since they are the main contributors to the total synchrotron emission.

In Fig. 1.4, it is shown the spectral energy distribution, from the radio to the far-infrared, of the prototypical starburst galaxy M 82 (U/LIRGs can be considered starburst galaxies due to their characteristics). The observed spectrum is the sum of the contribution of non-thermal synchrotron emission (dot-dashed line) coming from Radio Supernovae and Supernova Remnants, thermal free-free emission (dashed line) coming from the HII regions, and dust emission at **F**ar **I**nfra**R**ed (**FIR**) wavelengths (dotted line).

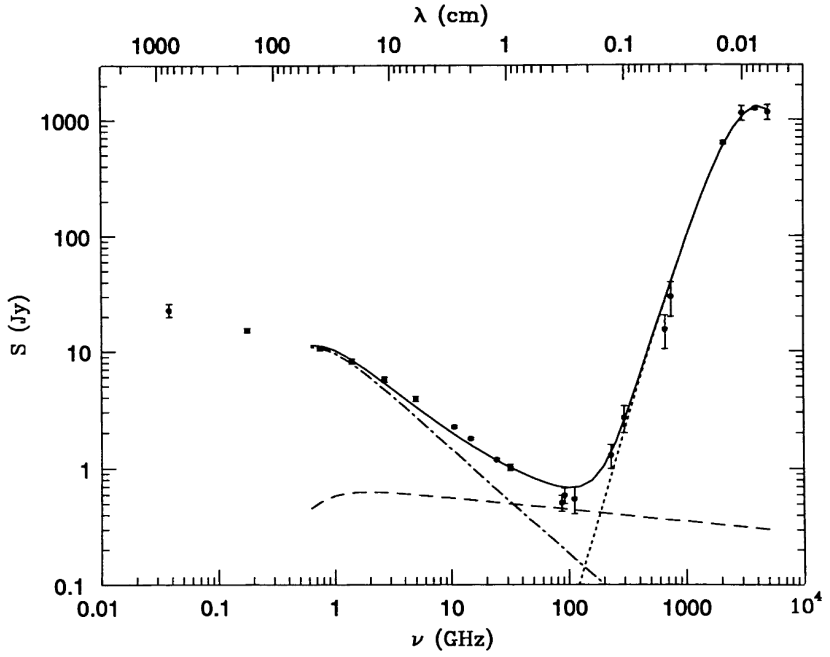

FIGURE 1.4: Spectral energy distribution of M 82 from radio to FIR wavelengths. Dot-dashed line represents synchrotron emission, dashed line the thermal free-free emission and dotted line emission at FIR wavelengths. Figure from Condon (1992)

There is an empirically relation between the **F**ar **I**nfra**R**ed (**FIR**) and the radio emission. The relation applies over at least four orders of magnitudes in FIR luminosity. It is closely related with the star formation, although it is still not completely understood how. The general scenario is the following one: young massive stars ($\geq$)8 $M_{\odot}$ produce huge quantities of UV continuum emission that is absorbed by the dust surrounding those stars. The dust is thus heated, and re-radiates the UV emission at FIR wavelengths. Once these stars die, they explode generally as SN II accelerating the CRs and making them gyrate in the magnetic field generated, giving rise to the synchrotron emission. In this way, a correlation of the radio and FIR emission is expected.

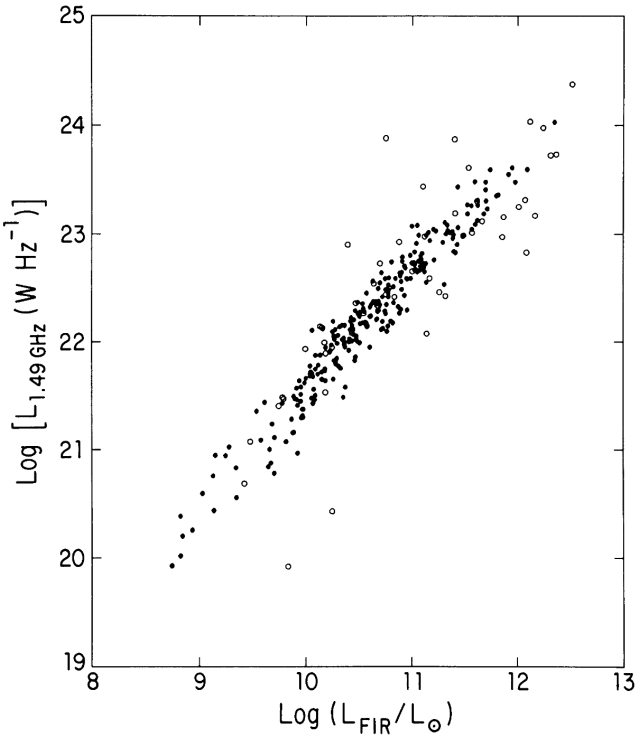

FIGURE 1.5: It shows the correlation of Radio vs. FIR luminosities for a sample of 313 spiral galaxies, which is limited in FIR luminosity to $S \leq 5.24\ Jy(\lambda$=60 μm). Figure from Condon, Anderson, and Helou (1991).

1.3 Supernova and AGN feedback in the evolution of U/LIRGs

Radio observations are a useful tool to help determining the **S**tar **F**ormation **H**istory of the **U**niverse (**SFHU**) through two different methods. First, the detection of synchrotron (non-thermal) emission from relativistic particles of supernovae. This emission depends on the cosmic ray energy density and the strength of the magnetic field in the **I**nter**S**tellar **M**edium (**ISM**). Second, the detection of free-free emission from HII regions. This emission is directly and uniquely dependent on the number of ionizing photons. Galaxies in the local Universe (which are the galaxies studied in the present thesis) observed between 150 MHz and 8.4 GHz (range used in this work) make possible to discern between synchrotron and thermal emission.

On the other hand, detection of radio loud and radio quiet AGNs is crucial in the determination of the evolution of galaxies, as those could be responsible for the quenching of star formation through the heating of gas or the expelling of it (see the recent studies of Su et al. 2020; Su et al. 2021 and references therein). Galaxies with flux densities $\geq$ 100 μJy are dominated by radio loud AGNs, whereas galaxies with flux densities below this value are dominated by star-forming galaxies and radio quiet AGN.

Therefore, both AGNs and starbursts determine galaxy evolution due to the expel of molecular gas from the reservoirs of the galactic nucleus (Rupke, Veilleux, and Sanders, 2005a; Veilleux, Cecil, and Bland-Hawthorn, 2005) in the form of outflows. Since AGNs and/or starbursts are the main actors responsible for heating the gas and dust in the those galaxies, and its subsequent re-radiation at IR wavelengths leads to the U/LIRG phenomenon, I will briefly explain the main characteristics of both AGN and starbursts, and some of the processes associated with them that regulate the evolution of the galaxies, e.g., the outflows.

SNe are usually divided into two different groups, according to the presence, or not, of H lines in their early-time spectra: Type I SNe do not show H lines, while Type II SNe do. However, a more physical division is that of core-collapse, and thermonuclear runaway supernovae. Type II SNe (which include a number of subtypes), and Type Ib/c SNe are the result of a collapse of the core of a massive star ($\geq 8 M_{\odot}$, Chandrasekhar (1931)), which is unable to support the gravitational force once an iron core is formed at the center of the star. The external layers fall in a fraction of a second and rebound on the iron core, which generates an expanding shockwave that propagates outwards at velocities of tens of thousands of kilometers per second. Type Ia supernovae are thermonuclear runaway supernovae. This kind of SN is the result of the explosion of a white dwarf in a binary system. If the other star is a normal star, the system is called single-degenerate. If, on the other hand, the companion star is also a white dwarf, the system is called double-degenerate. This explosion is, then, not from a collapse of any

nucleus, but of thermal nature, starting in the surface of the white dwarf. The objects of study in this thesis (U/LIRGs) are star-forming galaxies. In the regions of ongoing star formation, it is much more likely that the **S**uper**N**ova **R**emnants (**SNRs**) observed are of collapse nature, since their progenitors are massive stars (and recent, in consequence), than being a SNIa, whose progenitor hosted a long-lived black dwarf.

The explosion of a SN is able to radiate in the whole spectrum, but does not last long in the optical, or at higher energies. Fortunately, the radio emission from core-collapse supernovae is long-lasting. The different phases a SN goes through are essentially three: an initial, free expansion phase, an adiabatic (Sedov-Taylor) phase, and a radiative phase. The first one encompass from the SN explosion as such, where the shockwave goes through the own star, freely, before it reaches the CSM and the ISM. This shock wave moves forward, but also produces a shock in the opposite direction, the reverse shock. The second phase is the adiabatic Sedov-Taylor phase, in which the density of the ISM equals the density of the swept up mass. As radiative losses in this phase are still negligible, the energy is conserved. During the expansion of a SNR, the magnetic field decreases in strength (Shklovskii, 1960), and decreases significantly the synchrotron emission. Therefore, there should be a mechanism that accelerates the particles to relativistic speeds and make possible the continuity of the radio emission. One option for a continuous bump of energy is the residual object (neutron star); but the most probable scenario is that the reacceleration takes place into the shock wave. Shock waves would produce irregularities of the magnetic field and the so-called diffusive shock acceleration (Bell, 1978a; Bell, 1978b). Another point to explain is the origin of the magnetic field that is triggering the emission of the electrons. This magnetic field is thought to be the previous ISM magnetic field compressed by the explosion. Apart from that, CRs themselves can amplify the magnetic field, inducing flow instabilities (Schure et al., 2012; Reynolds, Gaensler, and Bocchino, 2012). The third and last phase is the radiative phase, where radiative losses start to dominate and the SNR phase comes to an end, dispersing into the ISM.

There is a particular type of galaxies that are called active galaxies. They are characterized by a central nucleus (the so-called active galaxy nucleus, AGN for short) that shines so brightly that it can become more luminous than the rest of the galaxy. The existence of a **S**uper**m**assive **B**lack **H**ole (**SMBH**) in the interior of these AGNs would naturally explain their properties: they emit a large amount of energy, which would be associated with gravitational processes linked to matter that would be attracted and squeezed towards the black hole. and the emission would cover all ranges of the electromagnetic spectrum. Nowadays, very long baseline radio interferometry at a few GHz yield milliarcsecond angular resolution, which translates in sub-parsec linear resolutions up to 200 Mpc.

The role of SMBHs in the evolution of the galaxies is determinant, because it is believed that they trigger or stop the star formation, via feedback processes. The AGN is able to expel gas, leaving its neighbourhood empty of fuel for new stars; in other cases, the expelled gas collides with pre-existing gas, starting the process of star formation. This feedback could be modified if we deal with a merger with other galaxy. Now, the collision produces that gas from the other galaxy flow away to the nuclei and feed the SMBH while enshrouding it. The result is known as obscured AGN (for example Arp299-A, which will be a target object), which is confused as a low luminosity AGN in many cases (Hopkins et al., 2009; Lambrides et al., 2020).

Outflows, also known as superwinds, are believed to cause the regulation of star formation in a galaxy, through negative feedback, sweeping away the material that should have fed up the starburst. Outflows are typically generated either by star formation, due to high-mass stellar winds, radiation, explosion events and cosmic rays (see e.g. Rupke (2018)), or AGNs via radiative energy or related to its mechanical effects. In that way, galaxies evolve from star-forming disk-like objects to ellipticals. The missing link between a starburst galaxy and an elliptical/lenticular galaxy seem to be the Ultra/Luminous Infrared Galaxies (Sanders et al. 1988; Rothberg et al. 2013). It is also important to incorporate new insights to outflows in order to improve the models of major gas-rich mergers, and how they grow with time. On the other hand, AGNs may also be responsible of the formation of an outflow. The launching of the plasma is a **m**agneto**h**ydro**d**ynamic process (**MHD**). The initial acceleration is activated by magnetocentrifugal forces that converts the magnetic energy into kinetic energy of the material coming from the accretion disk. It is collimated through a self-generated toroidal field created by the plasma inertial forces.

1.4 Radio Interferometry

More and more celestial objects have been detected over the centuries as the instruments developed improving their sensitivity. Thus, Messier, between 1770 and 1780, prepared a list of 110 objects (among them many galaxies) that were observed in the Parisian night sky. As time went by, and optical telescopes increased their sensitivities, the catalogues of detected objects were extended. In the 1880s, the so called ***N**ew **G**eneral **C**atalogue* (NGC), including almost 8000 objects was created. Over the years, telescopes were built up bigger and bigger, which enormously increased their sensitivity, which is proportional to the area of the detector, $\sim D^2$. where D is the diameter of the telescope. By making telescopes bigger, we also get a sharper view in case they work in the diffraction limit. Indeed, the angular resolution (i.e., the capacity to differentiate two

points in the sky when they are close together) is proportional to the observing wavelength, and inversely proportional to the diameter of the telescope, $\theta \sim \lambda/D$. Thus, optical wavelengths, for example, could potentially obtain resolutions of milliarcseconds with large telescopes. However, the atmosphere precludes us from reaching such high angular resolutions in the optical. In fact, the angular resolution is normally limited by the seeing, which is hardly any better than about 0.5 arcsec, unless one uses adaptive optics, which can yield angular resolutions of about 0.1 arcsec.

To pinpoint the sources that produce the heating of the dust in U/LIRGs, sharp and deep observations are essential. Optical observations are of no use, as the dust blocks all optical photons, but radio emission goes unimpeded by dust. Deep radio images can then be obtained by increasing the observing time as long as necessary. But sharpness is a tricky problem when we have to observe in radio. For an optical telescope observing above the Earth atmosphere, e.g. the HST, its angular resolution is diffraction limited, and is about 0.15 arcsec. To obtain a similar angular resolution at cm-wavelengths, the diameter of a radio telescope would have to be of the order of a few hundred kilometers. This, as one might imagine, is technically impossible. However, a weakness can become a strength: radio wavelengths can be combined in a coherent way better than at the rest of wavelengths thanks to the interferometry technique, where the combination of several antennas are able to make the role of a virtual antenna of even more than hundreds of kilometers. Moreover, this technique allows to probe different angular resolutions, thus is capable of detecting compact objects, as well as diffuse emission. However, thanks to the interferometry, the diameter of the antenna can be replaced by the distance between telescopes. As in the case of a single telescope, the angular resolution is $\theta = 1.23\frac{\lambda}{d}$, where λ is the wavelength of the emitted light and d is the separation between antennas.

I will now explain the basics of radio interferometry, which involves two main steps in order to obtain the final image of our source of interest:

$$\text{Sky Brightness} \xrightarrow{\text{Fourier Transform}} \text{Dirty Image} \xrightarrow{\text{Deconvolution}} \text{Clean Image}$$

1.4.1 From the sky to the dirty image: The Fourier Transform

The signal of the source is collected by each antenna and detected as a voltage. Next, each signal is correlated between antennas, pair by pair, which consists in multiplying and averaging the voltages. Then, we obtain the complex visibility. Visibilities are just the terms of the Fourier series that define the brightness distribution of the real source in the sky. Thus, the visibility is composed of an amplitude for a given term of the Fourier series, and a phase, that depends on the frequency, the baseline between the antennas we are considering, and the location of the source, if it is not in the center

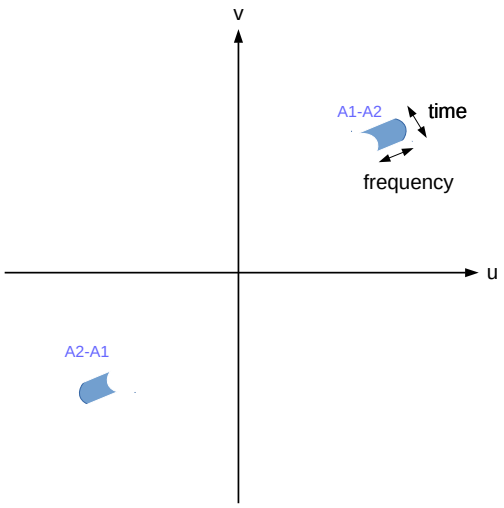

FIGURE 1.6: Representation of the interferometric uv-plane (u x-axis, v y-axis). The "instantaneous" observation by a baseline (between antennas A_1 and A_2) at a given frequency and time is represented as a blue shape. Note that there are two ranges in opposite quadrants, since given a baseline there are two possible directions (from A_1 to A_2 and from A_2 to A_1).

of phases (this center is not absolute, but once is chosen all has to be referred at this center). It is mathematically described as:

$$T(l,m) = \int\int V(u,v)e^{-2\pi i(ul+vm)}dudv \tag{1.4}$$

Here, $T(l,m)$ is the real signal of the source in a given l and m real position; and $V(u,v)$ the visibilities at an u and v position in the uv-plane.

For a given observation, once the frequency and the position of the source is given, the relative position of the antennas are the parameters that form the different terms of the Fourier series. These relative positions are located in the so-called uv-plane, and for a given point in the plane (the separation between A_1 and A_2, where A_i is the location of an antenna i) we will also have the point in the opposite direction (from A_2 to A_1). To obtain the true image, it would be necessary to obtain all the components of its Fourier series; but it is not possible to cover all the uv-plane with a limited number of antennas, so a first approach to the real case is to make use of the Earth's rotation to fill it up. Thus, the uv-plane is filled in portions of interval times, with a width given by the bandwidth and with different baselines (see Figure 1.6).

Once the data is correlated it is necessary a step of calibration, since our case is not ideal, and each instrument requires particular calibration depending on its architecture

and electronics. Some examples would be the effect of the changing atmosphere, wrong phase center, differences between clocks in the antennas, etc.

1.4.2 From the Dirty Image to the Final (Clean) Image: Deconvolution

In the course of the observation (the Earth rotating on itself) just some ranges of the uv-plane are filled ($S(u,v)$). These ranges represent the "active" terms of the Fourier series that are available for the reconstruction of the real image, so the integral of Eq. 1.4 becomes a sum:

$$S(u,v) = \sum_{k=1}^{M} \delta(u-u_k, v-v_k)$$

Where M is the discrete number of (u,v) points in the observation. Applying the Fourier transform to this discrete sum of certain terms (in the Fourier space) we obtain the point spread function, or in radio words, the dirty beam (in real space), s(u,v). This beam is responsible for spreading out the flux of a point source. So the Fourier transform reads thus:

$$V(u,v)S(u,v) \xrightarrow{F} T^D(l,m)$$

Where $T^D(l,m)$ is the dirty brightness distribution. In the real space, the dirty image is just the convolution of the real image ,$T(l,m)$, with the dirty beam:

$$T(l,m) * s(l,m) = T^D(l,m)$$

The goal now is to recover the real image, as reliable as possible. The generalized process to obtain the deconvolved image is called cleaning. First of all, a clean image with no point sources is initialized. Then, the peak is identified in the residual image, $T^D(l,m)$ and subtracted. Then, the scaled dirty beam $s(l,m)$ is applied to that subtracted point and the result added to a clean image. These steps are repeated until the residual image show essentially noise.

1.5 Facilities used in this thesis

The results presented in this PhD has been obtained from three main radio facilities. e-MERLIN, LOFAR and the JVLA.

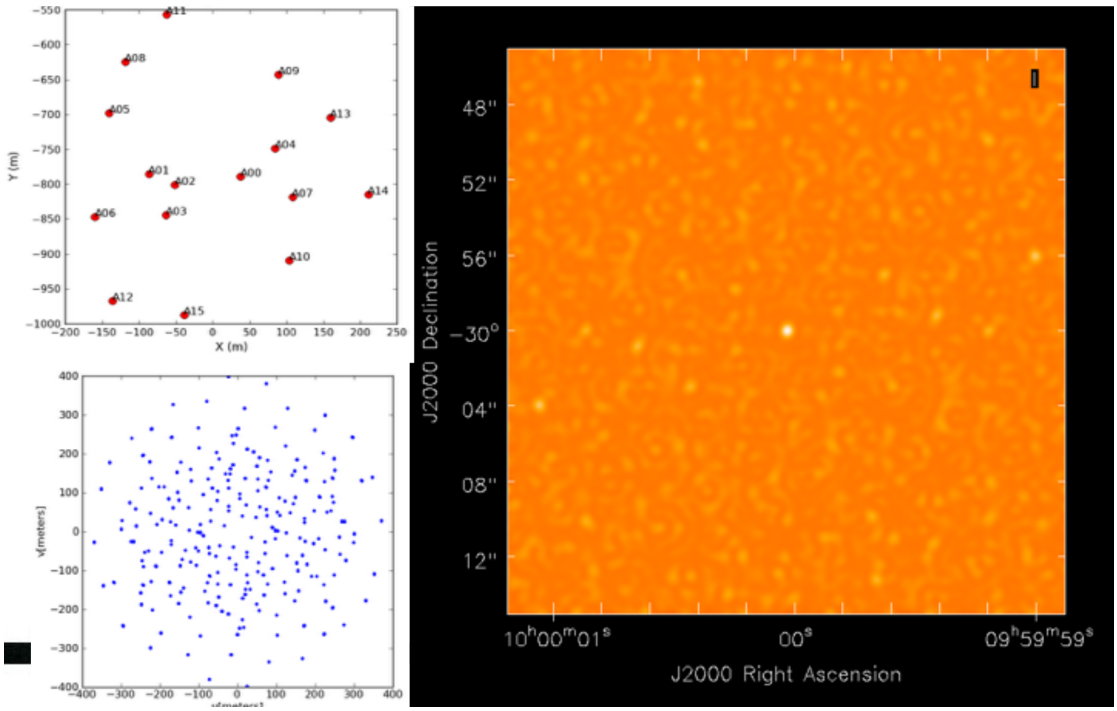

FIGURE 1.7: Upper left image shows the position of the antennas 16 in an extended configuration (VLA). Bottom left image represent the corresponding uv-plane of the upper antenna positions in a certain frequency and instantaneously. Right image is the resulting beam for this (*Image taken from a presentation for the NRAO workshop of Lucca Ricci "Introduction to the Interferometry")*.

e-MERLIN

The **e**nhanced **M**ulti **E**lement **R**emotely **L**inked **I**nterferometer **N**etwork (**e-MERLIN**) is a heterogeneous array of 7 radio telescopes connected by an optical fibre network to Jodrell Bank Observatory, its headquarters. e-MERLIN works at the .5, 5 and 22 GHz bands, with a bandwidth of 4 GHz, reaching resolutions between 10-150 mas. The sensitivity reached is around 10-20 of μJy in 12 hours of integration.

The seven antennas are: the Lovell and Mark II antennas, located in the Manchester area, with a diameter of 76 and 25×38 m, respectively; Cambridge, with 32 m; and Pickmere, Darnhall, Knockin and Defford, each of 25 m. See the distribution of the antennas in Fig. 1.8 and in the map of 1.11 (blue symbols).

Due to the characteristics of the instrument, eMERLIN is used to study different astrophysical scenarios, such us the local/global star formation in local/high-z galaxies, the extreme physics of a neutron star, the formation of the AGN jets, or the gravitational lensing. Here I focus my attention in the capability of this instrument in tracing regions of star formation and galactic nuclei.

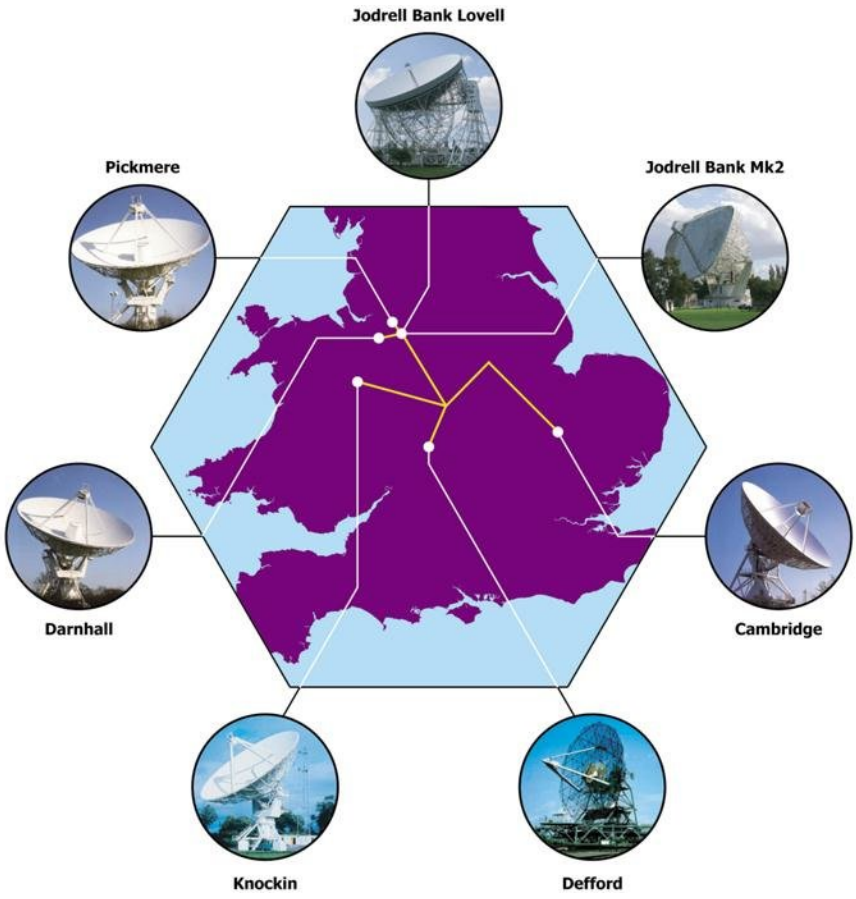

FIGURE 1.8: Distribution of the seven antennas through the United Kingdom.

In the context of the new era of the upcoming **S**quare **K**ilometer **A**rray (**SKA**), eMERLIN is a precursor where information can be obtained via the high resolution observations, long-distance data transport and testing of the optical fibre links in the phase transfer.

LOFAR

The **LO**w **F**requency **AR**ray was conceived in 2012 by ASTRON in the context of the SKA era. LOFAR brought a possible solution for the goal of building a huge collecting area: the Phased Aperture Array. It consists of a distribution of small fixed dipoles in a random or regular pattern that is able to observe more than one part of the sky simultaneously. Using different time delays, it is possible to obtain different beams of different positions in the sky. The only limits are signal processing, data communications and computing capacity. The antennas are distributed in the following way: 9 antennas form 1 tile (1.9, left image, blue crosses); depending on the station, one station can host 24 tiles (LOFAR core), 48 tiles (Remote stations in the Netherlands) or 96 tiles (International Stations). The antennas are grouped in stations (Figure 1.9), 48 in Netherlands and 8 in remote stations throughout Europe. The core distributes the antennas to cover up an instantaneous uv-coverage good to the study of the reionization epoch and radio transients searches. Aside from the core, located close to the village Exloo (the Netherlands, see 1.11) the 16 remote LOFAR stations are distributed over the Netherlands in a logarithmic spiral distribution.

LOFAR is splitted into two main bands: the **H**igh **B**and **A**rray (**HBA**) and the **L**ow **B**and **A**rray (**LBA**). The HBA works in the 110-240 MHz range (150 MHz corresponds to a wavelength of almost 2 meters), while LBA operates in the 30-80 MHz domain. In the present thesis I will resort to that last band, which, together with up to 1000 km baseline added with the International Stations,provide sub-arcsecond angular resolution in the LOFAR images presented in this Thesis.

LOFAR is the largest pathfinder for the SKA-LOW telescope. The contribution of LOFAR to the SKA development is of technical nature, such as high band width data links, or massive correlation, among others.

JVLA

The Karl G. **J**ansky **V**ery **L**arge Array (**JVLA**) is a radio interferometer located in Socorro, New Mexico (see Figure 1.11, yellow antenna symbol). It is an array consisting of 27 antennas of 25 meters of diameter, disposed in a Y-shape. They can be moved from its most extended configuration, A, down to its most compact one, D (see Fig. 1.10).

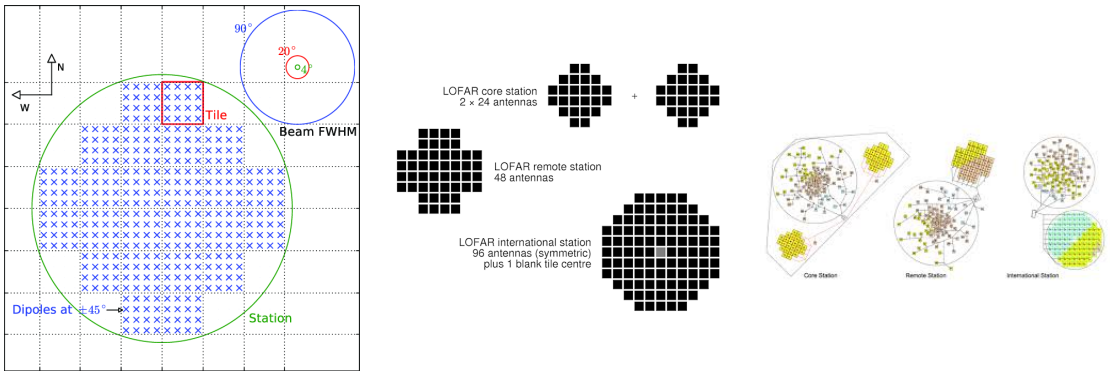

FIGURE 1.9: *left:* Scheme of a station (large green circle), a tile unit example (red square), and distribution of dipole antennas (blue crosses). The circles up right are the comparison of the corresponding beams for each unit (using the same color code as the scheme). *Center:* Different configuration of the stations. Squares represent the tiles therein. *Right:* Disposition of the different stations, as core, remote or international.

In total, it covers from 21 km of the A-configuration to 1 km in its most compact D-configuration. The array configuration changes periodically. It covers a wide, almost continuous range of frequencies from 58 MHz up to 50 GHz. The VLA data analysed in this thesis have been obtained in bands L (1.4 GHz), C (5 GHz), and X (8.4 GHz). The resolution reached by this instrument is up to 0.2" at 8.4 GHz in A-configuration.

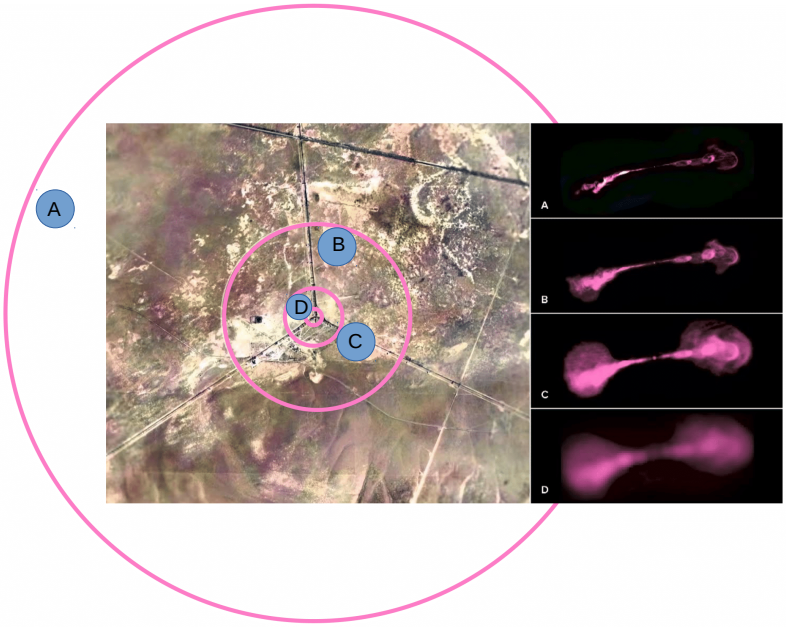

FIGURE 1.10: **Left**: Aerial view of the location of the Jansky VLA antennas. The pink circles correspond to the different configurations available (from A, the most compact, to D, the most spread). **Right**: VLA images of Hercules A, taken with the different configurations at left. Note how the sharpness evolves from the A configuration image to the D one.

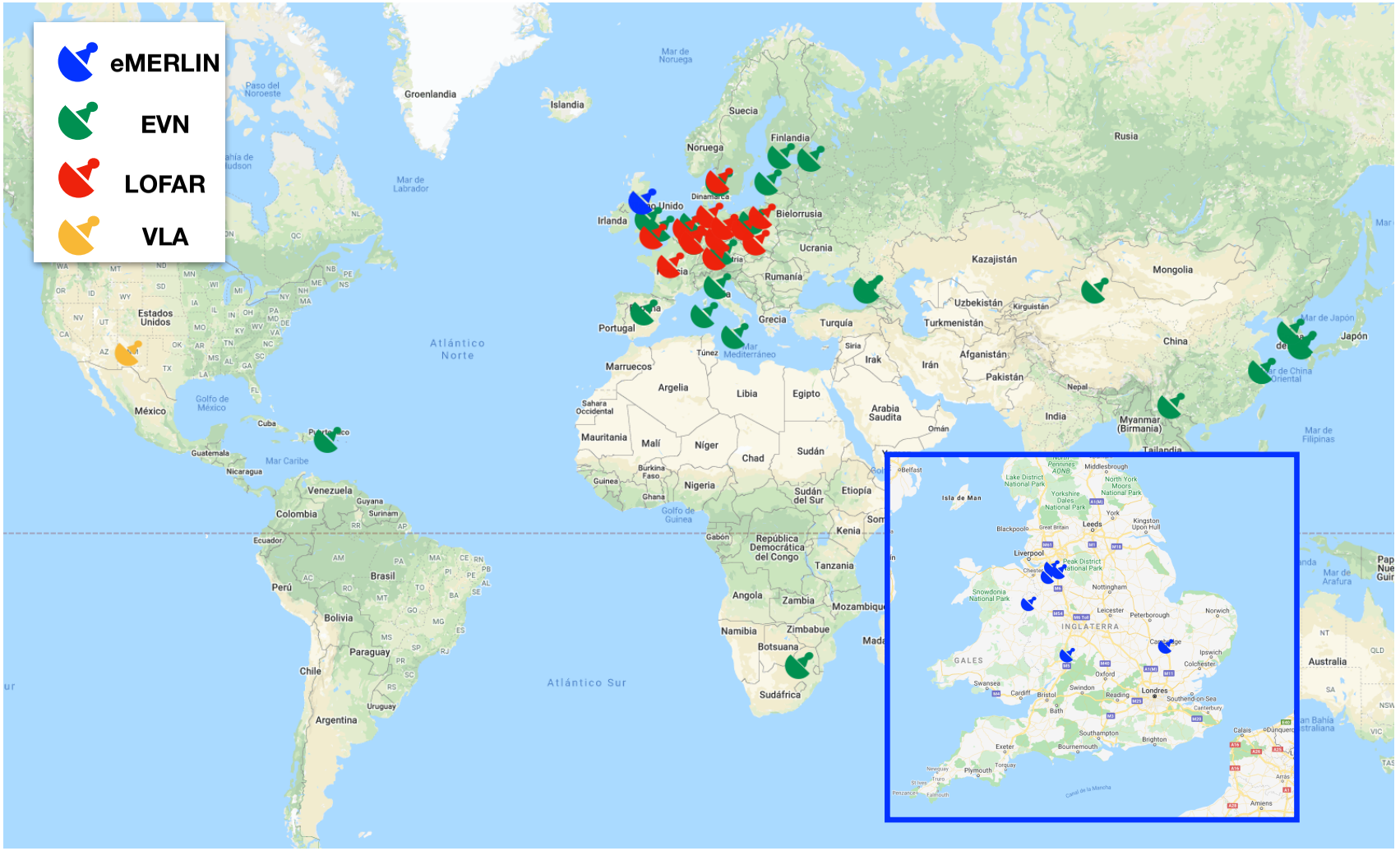

FIGURE 1.11: Map with the different arrays of antennas used in this thesis distributed around the World. Colors of the antennas are indicated in the legend up in the figure. In the right-down corner, a zoom-in for the eMERLIN array in the UK. VLA is indicated as unique antenna in the map, but it consists in 25 antennas (see Figure 1.10). LOFAR has been draw as a unique antenna in the Netherlands as well, but in this place are located 40 stations. **E**uropean **V**LBI **N**etwork (**EVN**) is also indicated in the map since it has been mentioned in Chapter 4.

1.6 Outline of this thesis

This thesis has the goal of showing the importance of radio observations at high resolution in the determination of fundamental characteristics of the above explained U/LIRGs. This thesis has been divided as follows:

- Chapter 2: This chapter presents an overall, comprehensive radio study of the local LIRG Arp299 at low and mid-frequencies (i.e, 150 MHz with LOFAR and 1.4, 5.0 and 8,4 GHz with the JVLA, respectively) to characterize both the compact and extended radio emission of Arp 299.
- Chapter 3: This chapter presents the detection of an outflow in Arp 299A, the first outflow ever detected from LOFAR observations.
- Chapter 4: In this chapter I present preliminary results from the e-MERLIN legacy project LIRGI, mainly from 5 GHz observations.
- Chapter 5: I study the supernova remnant luminosity function from a relatively large sample of SNRs in nearby normal galaxies, using a novel statistical approach, and adding the SNRs of Arp299 and the new catalogue of SNRs of Arp220.
- Chapter 6: I summarize the main results of this thesis and discuss future prospects.

2 Low-frequency radio emission in the merging galaxy Arp 299

2.1 Introduction

ULtra/Luminous Infrared galaxies (U/LIRGS) are the most luminous galaxies in the infrared domain ($\log(L_{IR}/L_{\odot}) \geq 11.0$ for LIRGs, $\log(L_{IR}/L_{\odot}) \geq 12$ for ULIRGs (Sanders and Mirabel, 1996)), with L_{IR} making up the bulk of their total bolometric luminosity of those galaxies. The number of U/LIRGs increases with redshift (Magnelli et al., 2009), suggesting that they were dominant in the infrared sky at z=1-2. The multifrequency study of their characteristics and behavior in the local Universe can serve as a template to understand the characteristics of U/LIRGs in the high-z universe.

Arp 299 (also known as NGC 3690-A + NGC 3690-B, Mrk 171, IRAS 11257+5850, VV 118) at $D = 44.8$ Mpc is the brightest LIRG within 50 Mpc, and with a luminosity of $L_{IR} \approx 8 \times 10^{11}$ $L_{\odot}$ it approaches the ULIRG class. The Arp 299 system consists of a pair of galaxies in an early major merging process (Keel and Wu, 1995), with three well separated regions (Gehrz, Sramek, and Weedman 1983; Neff, Ulvestad, and Teng 2004). Region A is the nucleus of the eastern galaxy, B is the nucleus of the western galaxy, and C and C′ are off-nuclear star-forming regions in the overlap of the two disk components of the system (Telesco, Decher, and Gatley, 1985). Both nuclei A and B are known to host AGNs: Arp 299-A hosts a Low Luminosity AGN (LLAGN;Pérez-Torres et al. 2010), while Arp 299-B is hosting an obscured Seyfert-like AGN (Della Ceca et al., 2002; García-Marín et al., 2006; Alonso-Herrero et al., 2013).

The inner kpc region of Arp 299 harbours a large amount of molecular gas in its circumnuclear regions ($M(H_2) = 7.5 \times 10^9$ $M_{\odot}$; Aalto et al. 1997), and an intense star

Telescope	Frequency	Project	Observing Date DD-MM-YYY	rms [μJy/beam]	Peak [mJy/beam]	Integrated Flux [Jy]
LOFAR	150 MHz	LC5-020	22-02-2016	98.2	23.2	0.90±0.13
JVLA-L	1.4 GHz	GP053	12-06-2015	59.8	113.1	0.59±0.08
JVLA-C	5.0 GHz	GP053	20-10-2014	18.9	70.6	0.35±0.05
JVLA-X	8.4 GHz	GP053	03-11-2014	11.9	44.6	0.43±0.06

TABLE 2.1: Summary of the observations of LOFAR and JVLA and their different configurations.

formation burst in their nuclear regions, within the central 100 pc (Pérez-Torres et al., 2009b; Bondi et al., 2012; Romero-Cañizales et al., 2011; Alonso-Herrero et al., 2000), has been unveiled through high angular resolution radio observations. The energy released by the compact starburst in the central region of Arp 299A is so large as to power a large scale superwind, or outflow, as recently unveiled by Ramírez-Olivencia et al. (2018) using the sub-mJy sensitivity and sub-arcsecond angular resolution capabilities of LOFAR at 150 MHz (LOFAR; van Haarlem et al. 2013).

The high sensitivity and angular resolution of LOFAR allow detailed studies of the very low frequency emission and absorption properties of nearby galaxies (e.g. M82 Varenius et al., 2015; Arp 220 Varenius et al., 2016). Together with matched angular resolution images at higher frequencies, the spatially resolved SED allows us to disentangle regions with different (thermal/non-thermal) spectral properties. For example, synchrotron emission in the sub-GHz regime can suffer significant free-free absorption by H II regions, (e.g. Condon, 1992). Since H II regions are commonly found within star-forming regions, at MHz frequencies the radio emission arising from supernovae and young massive stars is expected to be partially suppressed due to the free electrons pervading the H II regions. This absorption can be traced well with LOFAR observations.

In this chapter, I present for the first time sub-arcsecond angular resolution images of the whole Arp 299 system at 150 MHz. We also present a physical characterization of the system based on the LOFAR observations at 150 MHz and JVLA observations at 1.4, 5.0, and 8.4 GHz (L-band, C-band and X-band, respectively).

2.2 Observations and data reduction

2.2.1 150 MHz LOw Frequency Array (LOFAR) observations

We observed Arp 299 with LOFAR between 22 and 23 February 2016 (project code LC5_20; P.I. Pérez-Torres, see Table 2.1), for a total of 12 h, including the LOFAR international stations. We centered our observations at a frequency of 150 MHz with 32 MHz bandwidth. We used the nearby compact source J1127+5841 for phase calibration, J1128+5925 for delay/rate/amplitude/bandpass calibration, and 3C 295 for absolute flux density calibration. Each observing scan lasted for ∼24 min, which included observations of the target and of the two nearby calibrators, J1127+5841 and J1128+5925. Every 30 minutes we observed the flux calibrator 3C 295 for 3 min, since it is bright and point-like, even for the **C**ore **S**tations (**CS**). This allowed us to remove the differences in phase generated by the electronics of the stations (the electronic delay varies slowly, hence a scan of 3 min each 30 minutes was enough). We also applied primary beam correction. This is particularly important for an array as LOFAR, which does not move and has different features for each azimuth. We also applied the (automatic) flagging via AOFlagger.

2.2.2 1.4 GHz, 5 GHz and 8.4 GHz Jansky Very Large Array (JVLA) observations

I show in Table 2.1 the summary for the observations taken at 1.4 GHz, 5.0 GHz and 8.4 GHz with the JVLA taken in October 2014 (5.0 GHz, C-configuration), November 2014 (8.4 GHz, C-configuration), and June 2015 (1.4 GHz, BnA to A configuration) under the global **VLBI** (**V**ery **L**arge **B**aseline **I**nterferometry) experiment GP053 (PI: Pérez-Torres).

The JVLA data were averaged to 10 sec in time and 2 MHz per channel before calibration to reduce the processing time. We then used AOFlagger v2.8 to remove **R**adio **F**requency **I**nterference (**RFI**), and converted the CASA data measurement set into UVFITS using the CASA task `exportuvfits`. We did all calibration and imaging steps in a standard manner using AIPS release 31DEC16 and ParselTongue 2.3. We referenced the Arp 299 visibility phases to the nearby calibrator J1128+5925, and derived the flux density scale and bandpass corrections from observations of the primary absolute flux density calibrator, 3C 286. We then imaged Arp 299 using the CLEAN deconvolution algorithm as implemented in the AIPS task `IMAGR`. Finally, we applied primary beam correction using the AIPS task `PBCOR`.

2.3 Results

2.3.1 General description of the LOFAR and JVLA images

Figs. 2.1 and 2.2 show our 150 MHz (LOFAR), 1.4, 5.0 and 8.4 GHz (JVLA) images of Arp299. The overall morphological similarity of the JVLA images with the LOFAR image is striking, considering the factor of ∼60 difference in frequency between our 150 MHz LOFAR image and the 8.4 GHz VLA image. The main components of Arp 299 are clearly detected in the LOFAR image: the two nuclei of the interacting galaxies, NGC 3690-A (where the peak of the whole LOFAR image is located) and NGC 3690-B, as well as the two prominent compact radio and infra-red emitting regions C and C'. The A nucleus shows evidence of an outflow-like structure. The B nucleus is resolved into its two main components: B1 (the true nucleus) and the emitting region B2 to the North-East. I will discuss in detail the nature of those regions in Chapter 3. I note that component D (see e.g. Neff, Ulvestad, and Teng 2004), which was initially thought to be part of the Arp 299 system but does not belong to it, is not detected in our LOFAR observations above a 3σ of about 1 mJy.

The diffuse emission is traced in detail also by the LOFAR observations, which show a clear bridge of emission that connects NGC 3690-A and NGC 3690-B. The morphological similarity of all images for the Arp 299 system, both in the compact and diffuse emission, already suggests that the main emission and absorption processes operating at all the frequencies are likely the same.

In Table 2.1 I show the summary of our LOFAR and JVLA observations. I determined the total integrated flux densities as follows. I first set up a 3σ level in all images, to be able to compare the emission from the nuclei and other compact features in Arp 299 at different frequencies. I then blanked all pixels below a 3σ threshold in the final images (not shown). The total uncertainty in the quoted flux density is the result of adding in quadrature the off-source rms σ_{rms}, and the calibration uncertainty, $\sigma_{syst,i}$ at each pixel position. I then measured σ_{rms} in the outer regions of the system and assumed a calibration uncertainty of the flux density per pixel of 15%, 10%,5% and 3% for 150 MHz, 1.4, 5 and 8.4 GHz, respectively.

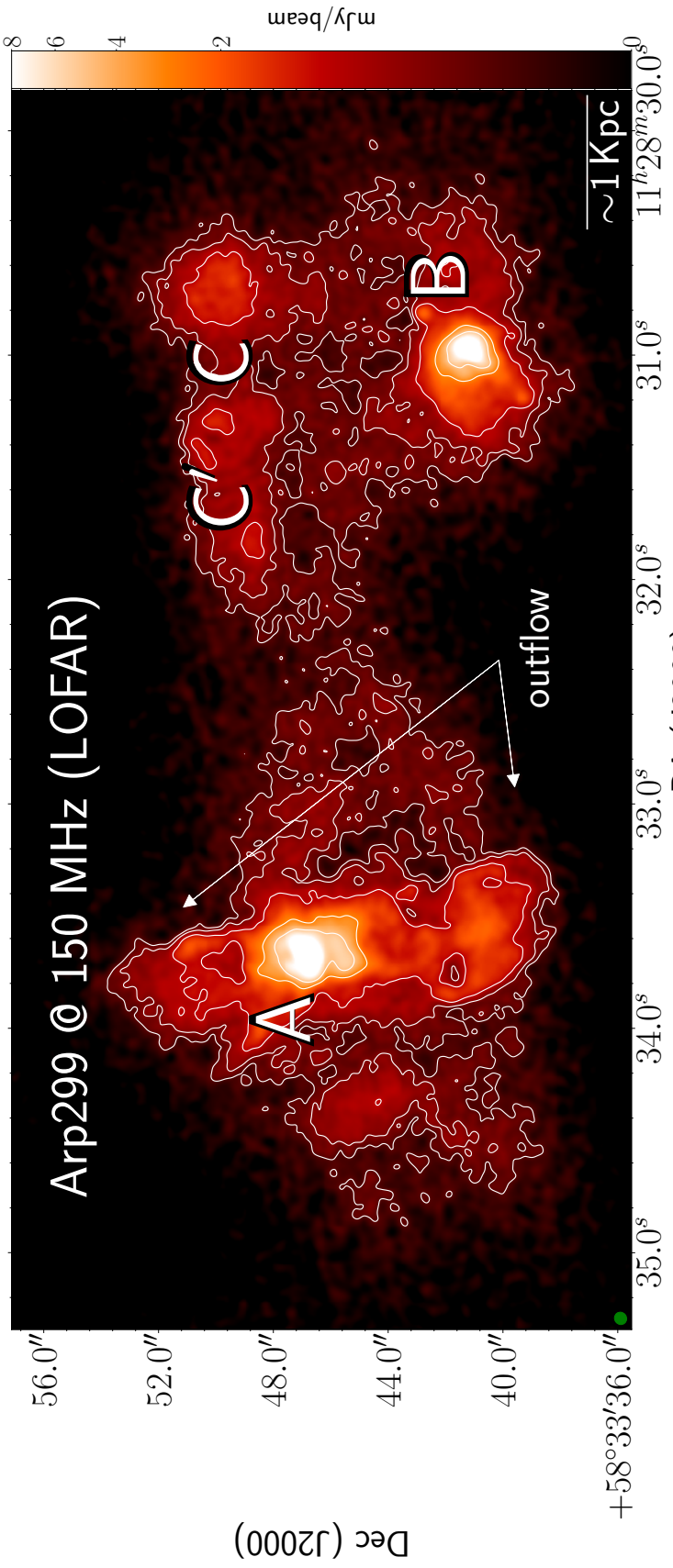

FIGURE 2.1: 150 MHz LOFAR image of the LIRG Arp 299 system. Contours represent [3,5,10,20,35,50,100,200,230]× rms (~98μJ/beam). Classical components are marked (A, B, C and C'), and the new outflow from A nucleus (Ramírez-Olivencia et al., 2018) is also indicated.

TABLE 2.2: Summary of compact component position, peak brightness and flux density from our LOFAR (150 MHz) and JVLA (1.4, 5.0 and 8.4 GHz) observations.

Components	Frequency	R.A[1]. (J2000)	Dec.[1] (J2000)	Peak mJy/beam	S_ν^2 mJy
A nucleus	150 MHz	11:28:33.661	+58:33.46.840	23	104.5±13
	1.4 GHz	11:28.33.634	+58.33.46.663	113	87.6±11.3
	5 GHz	11:28:33.628	+58.33.46.650	71	80.3±4.1
	8.4 GHz	11:28:33.628	+58.33.46.643	44	60.9±1.9
B nucleus	150 MHz	11:28:30.967	+58:33.41.240	16	36.0±9.8
	1.4 GHz	11:28.30.986	+58.33.40.816	32	63.4±4.3
	5 GHz	11:28:30.989	+58.33.40.803	13	18.5±1.3
	8.4 GHz	11:28:30.987	+58.33.40.800	9	13.4±0.5
C component	150 MHz	11:28:30.665	+58:33.49.399	17	25.8±4.6
	1.4 GHz	11:28.30.645	+58.33.49.305	9	17.9±2.3
	5 GHz	11:28:30.651	+58.33.49.305	3	10.5±0.6
	8.4 GHz	11:28:30.652	+58.33.49.318	1	8.0±0.3
C′ component	150 MHz	11:28:31.084	+58:33.51.720	14	17.1±3.3
	1.4 GHz	11:28.31.336	+58.33.49.989	7	11.4±2.1
	5 GHz	11:28:31.335	+58.33.50.008	3	7.4±0.6
	8.4 GHz	11:28:31.333	+58.33.50.017	1	6.0±0.3

[1] Position of the peak for each band and compact source.

[2] Integrated flux in the area described in Sect. 2.3.2

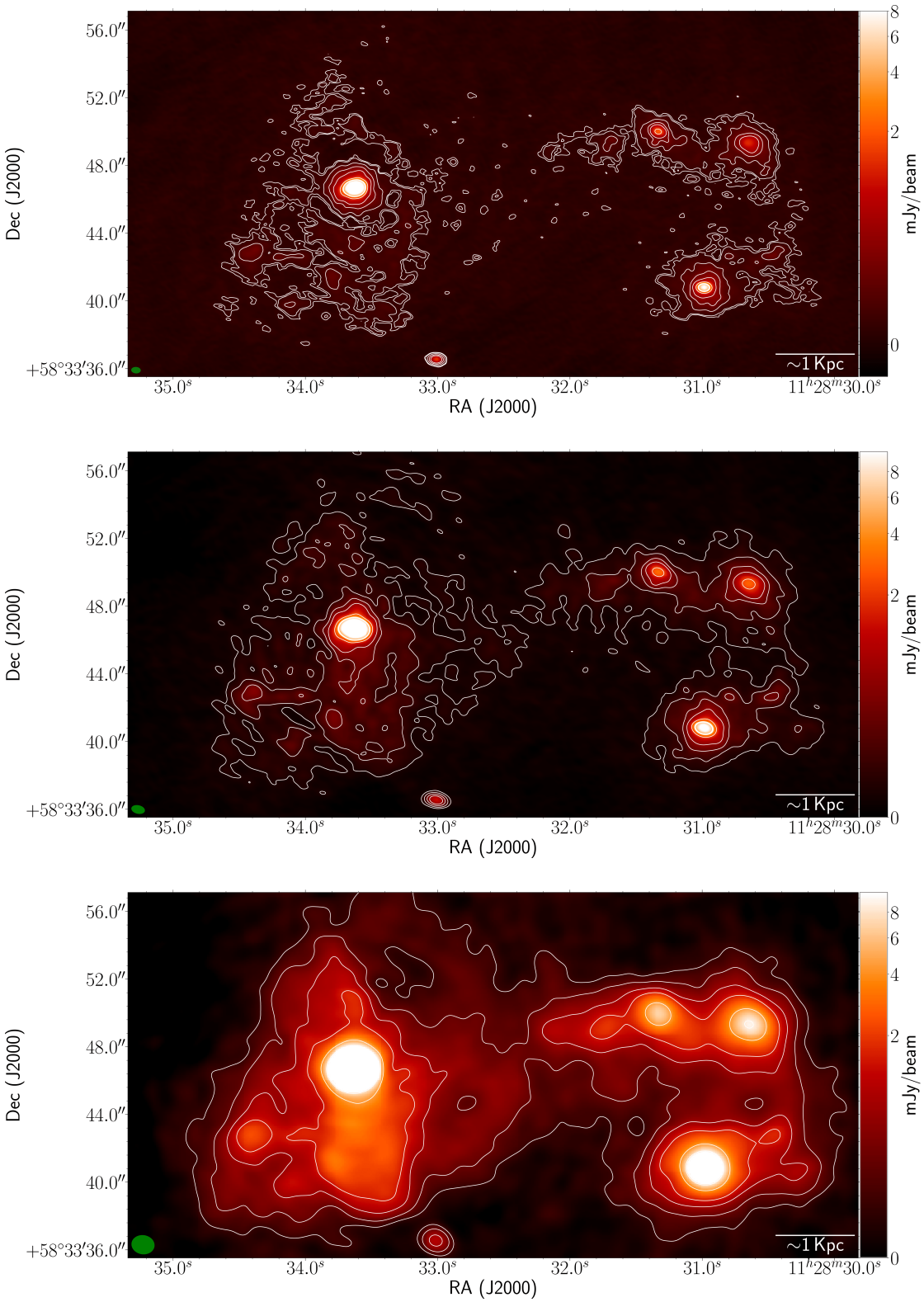

FIGURE 2.2: Images of Arp 299 observed with the JVLA at 1.4 GHz (top), 5 GHz (middle), and 8.4 GHz (bottom). Contour levels are drawn at (3,5,10,20,35,50,100,200,230,250)×rms at each band (see Table 2.1)

2.3.2 Spectral properties at radio wavelengths

In this section, I first determine the integrated flux densities of the nuclei at different bands, and then the spectral-index maps for the whole Arp 299 system.

Integrated flux density of the nuclear components

All the nuclear components A, B, C and C′ are detected at all frequencies. I show in Table 2.2 the peak and total flux density for the nuclei of Arp 299. I used the same physical size at each frequency, for a direct comparison of our results. I first convolved the images of the nuclear components A, B, C and C′ at each frequency to the largest beam, which corresponds to that of the 1.4 GHz observations ($\theta_{\mathbf{FWHM}}$ ∼1.4 arcsec, **F**ull **W**idth **H**alf **M**aximum), using a circular beam for simplicity. I also regridded the JVLA images to the coordinate system of LOFAR using the CASA task `imregrid`. I then used the region delimited by the 50% of the peak of the convolved 1.4 GHz image, as a common angular size for all images. For the uncertainties, I proceeded in the same way as described in Sect. 2.3.1, except that I used the uncertainty map for each band of the JVLA observations. The results are summarized in Table 2.2.

I note that the maximum of the radio emitting peaks occurs at 150 MHz for C and C′, while in the case of A and B the maximum is located at 1.4 GHz. The A nucleus is the brightest component at all frequencies. Most of the emission from the Arp 299 system comes from the extended emission, with only ∼20%, ∼30%, ∼33% and ∼20% at 150 MHz, 1.4, 5 and 8.4 GHz, arising from the compact nuclear regions, respectively.

Spectral index maps

I obtained two-point spectral index (α, according to the power law S_ν=ν^α) images by combining our LOFAR and JVLA observations. I first used the convolved and regridded images at each frequency, as described in the previous subsection, and then applied the CASA task `immath` to the following pairs of images: 150 MHz - 1.4 GHz; 1.4 GHz - 5.0 GHz; 5.0 GHz - 8.4 GHz (left panels in Fig. 2.3).

I computed the pixel-wise spectral index uncertainty as in Kim and Trippe (2014) and Varenius et al. (2016):

$$E(\alpha_{\nu 1,2}) = \frac{1}{\log(\nu_2/\nu_1)} \times \left[\frac{\sigma^2_{\nu_1}}{S^2_{\nu_1}} + \frac{\sigma^2_{\nu_2}}{S^2_{\nu_2}}\right]^{1/2} \tag{2.1}$$

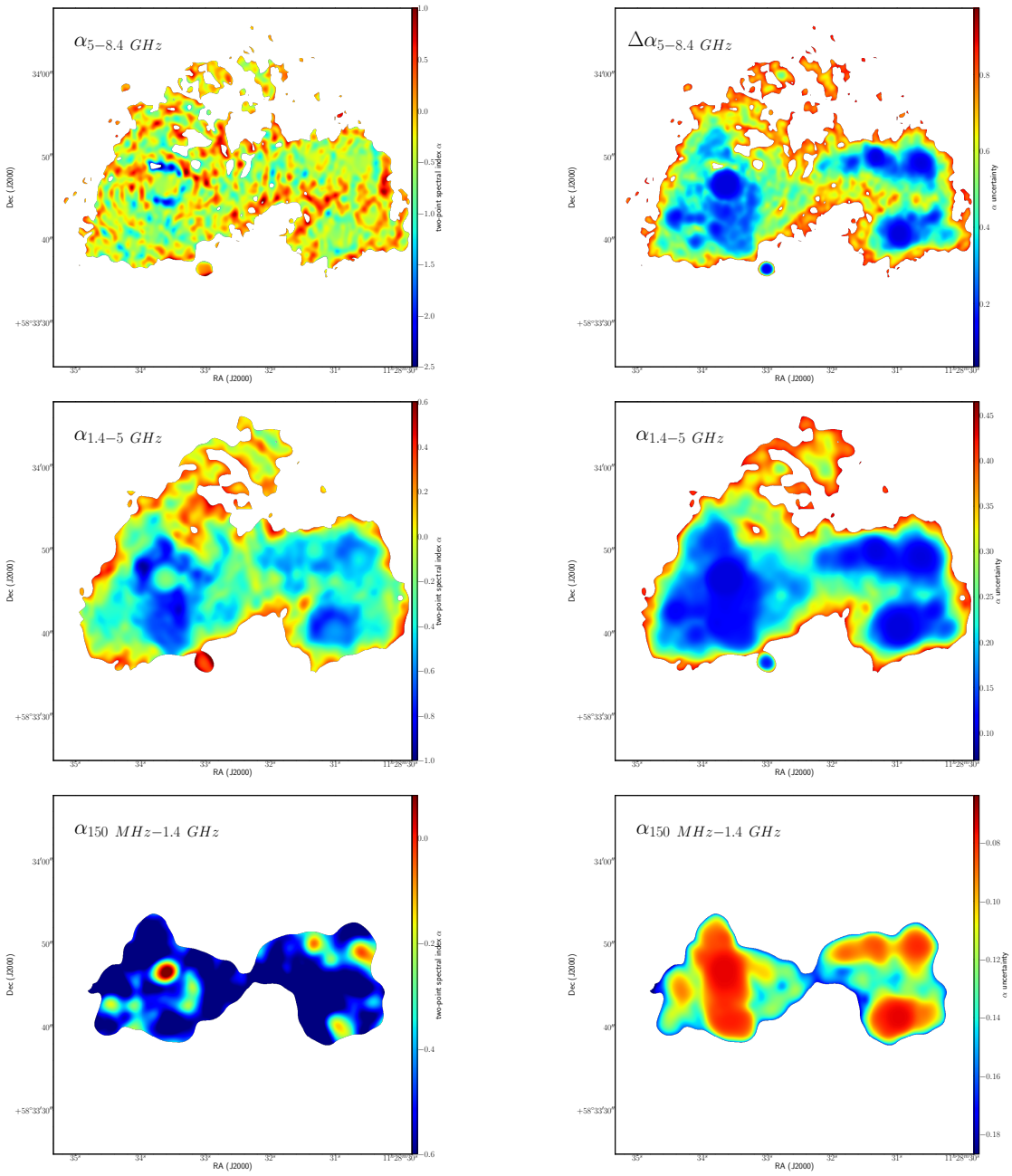

FIGURE 2.3: *Left:* Plots for the spectral index maps; (a) corresponds to $\alpha_{(8.4GHz-5GHz)}$ at a resolution of 0.8" $\times$ 0.8", (c) to $\alpha_{(5.0GHz-1.4GHz)}$ at a resolution of 1.4" $\times$ 1.4" and (e) to $\alpha_{(1.4GHz-150MHz)}$ at a resolution of 1.4" $\times$ 1.4" *Right:* Total spectral index error (taken into account the Eq. 2.1) at the frequencies given by the left image of each one. For more details, see Sec. 2.3.2.

where σ_{ν_i} is the total intensity error. For the sake of clarity, I blanked all pixels in the spectral index maps that had an uncertainty larger than 0.4 in absolute value (right panels in Fig. 2.3).

The spectral index maps in Fig. 2.3 help us to understand the nature of the emission of the different regions. In the spectral index map between 5 and 8.4 GHz (Fig. 2.3, top-left), the general trend is within the range $\alpha_{8.4GHz-5GHz} \in (-0.3, -2.)$, suggesting that the whole galaxy is dominated by non-thermal synchrotron emission. The spectral index of the radio emission in the nuclear regions in Arp 299 starts to depart from the spectral index of the diffuse emission at some frequency between 1.4 and 5 GHz (Fig. 2.3, middle-left). This trend becomes more evident in Fig. 2.3 bottom-left, where the spectral index, $\alpha_{1.4GHz-150MHz}$, clearly distinguishes the diffuse emitting regions, where $\alpha_{1.4GHz-150MHz} \leq$ -0.5, from the nuclear emission, where $\alpha_{1.4GHz-150MHz} \sim$ 0.0. This different low-frequency behaviour of the synchrotron emitting regions, where the nuclei display flat spectra, while the diffuse emission outside of the nuclei shows a rather steep spectrum, can be easily explained if, e.g., free-free absorption becomes increasingly relevant at frequencies around and below 1.4 GHz within the nuclear regions. In this case, the radio spectra will flatten in those regions, diverging from the pure synchrotron behaviour observed in those regions outside the nuclei. For the case of A and B nuclei, the observed flat spectral index could be in principle explained by the presence of an AGN that would flatten the spectrum. However, this is at odds with milliarsecond angular resolution radio observations with VLBI obtained for the A and B nuclei by, e.g., Pérez-Torres et al. (2009b), which find the putative AGN contribute very little to the total radio emission observed at cm-wavelengths.

The bright knots C and C′ do not host any AGN, and are off-source star forming regions in an interaction region between the two galaxies within the Arp 299 system. The flat spectral index on these physical scales (tens to hundreds of pc) at lower frequencies (150 MHz to 1.4 GHz) can be explained by the absorption of the synchrotron emission by H II regions (Sec. 2.4.1), excluding the presence of an AGN. The emission of these two off-nuclear regions is extended and partially resolved at all four frequency bands, in contrast with the compact sources present in the A and B nuclei. Making use of the spectral index maps (see Fig. 2.3), it is evident that the central areas of the nuclei C and C′ have a flatter spectral index than the extended emission surrounding them, which is of synchrotron origin. This synchrotron emission would come from the star-forming regions C and C′ (HII regions) resulting from the interaction between NGC 3690-A and NGC 3690-B. The flat spectral index on these physical scales (tens to hundreds of pc) at lower frequencies (150 MHz to 1.4 GHz) can be completely explained by the absorption from H II regions, excluding the presence of an AGN (spatial scales of a few pc). This is this case of C and C′, which have a relatively flat spectral index between 1.4 GHz and 150 MHz although they do not harbour any AGN.

Spectral Energy Distributions of compact components

I show in Table 2.3 the flux density per solid angle, S_ν/Ω, for each compact component and frequency of Arp 299, where I used the sizes obtained as described in Sec. 2.3.2. I plot those values against frequency in Fig. 2.4, to build up broadband spectral energy distributions between 150 and 8400 MHz. The spectra of all four components are inconsistent with a pure, unabsorbed synchrotron power-law, but show instead signs of flattening. In the next section 3, I fit these spectra using models with mixed synchrotron and free-free emission and absorption.

2.3.3 Magnetic Field

I show in Table 2.3 the minimum equipartition magnetic field for the nuclei of Arp 299. This magnetic field is obtained by assuming equipartition between the cosmic ray energy and the magnetic field energy (Pacholczyk, 1970):

$$B_{eq} = (4.5c_{12}/\phi)^{2/7}\,(1+\psi)^{2/7}\,R^{-6/7}L_R^{2/7} \tag{2.2}$$

where c_{12} is a slowly varying function of the spectral index, α; ϕ is the filling factor of fields and particles; R is the linear radius of the emitting region; L_R is the radio luminosity of the source; and ψ is the ratio of the total heavy particle energy to the electron energy. Depending on the mechanism that generates the relativistic electrons, this ratio will range between ψ ≈1 to $\psi \approx m_p/m_e$ ≈2000 (where m_p and m_e are the proton and electron mass, respectively). For simplicity, I used here ϕ = 0.5 and ψ = 100. (See Appendix B for details).

2.4 Discussion

2.4.1 Emission models for compact components

Radio emission in LIRGs comes from a combination of synchrotron and free-free emission. Synchrotron emission arises from relativistic electrons accelerated in supernovae (with possible contributions from buried AGN and associated radio jets), interacting with magnetic fields. The free-free emission component is Bremsstrahlung emission from ISM gas ionized by massive stars. While the free-free thermal gas makes only a small emission contribution at gigahertz frequencies and below, it can have a large effect on the overall spectrum at low radio frequencies because it can effectively absorb background synchrotron emission. Such low frequency absorption effects of thermal

	R_{ang} arcsec (1)	S_ν/Ω mJy/arcsec^2 (2)				N_{cl} (3)	α (4)	f_{th} (5)	ν_t GHz (6)	EM/10^5 pc cm^{-6} (7)	B_{eq} μG (8)	t_{sync} 10^3yr (9)			
		150 MHz	1.4 GHz	5.0 GHz	8.4 GHz							150 MHz	1.4 GHz	5.0 GHz	8.4 GHz
A	1.52	32.4	37.5	29.6	22.3	-	-0.33 (0.11)	0.007 (0.004)	0.23 (0.08)	1.4	246	154	17	16	12
						5.2 (0.8)	*-0.6 (fixed)*	*0.18 (0.04)*	*1.16 (0.08)*	*42*	*286*	*114*	*12*	*13*	*10*
B	1.58	20.9	11.3	5.9	4.3	-	-0.56 (0.02)	0.014 (0.002)	0.18 (0.01)	0.8	186	260	28	24	18
						1.8 (0.2)	*-0.6 (fixed)*	*0.05 (0.01)*	*0.33 (0.03)*	*2.4*	*192*	*253*	*27*	*24*	*18*
C	2.09	2.8	1.95	1.16	0.88	-	-0.59 (0.02)	0.089 (0.008)	0.23 (0.04)	1.4	106	790	87	55	43
						5.6 (7.6)	*-0.6 (fixed)*	*0.18 (0.06)*	*0.24 (0.03)*	*1.5*	*102*	*903*	*97*	*61*	*47*
C′	1.96	3.18	2.1	1.4	1.2	-	-0.39 (0.02)	0.050 (0.008)	0.15 (0.04)	0.6	102	883	95	60	46
						5.0 (fixed)	*-0.32 (0.07*	*0.038 (0.003)*	*0.122 (0.001)*	*0.4*	*97*	*903*	*97*	*61*	*47*

[1] Angular radius of each component; measured as described in 2.3.2.
[2] Flux density per solid angle measured for each component. Calculated as described in 2.3.2.
[3] Mean number of clumps intercepted per LOS assuming clump model. Note that this is only given for the clumpy model rows (see table caption).
[4] Spectral index of synchrotron emission, as described in 2.4.1.
[5] Thermal emission as a fraction of synchrotron emission at 1 GHz, as described in 2.4.1.
[6] Frequency at which free-free opacity through source equals unity (see 2.4.1 and Appendix A).
[7] Emission Measure along LOS, estimates as described in 2.4.1.
[8] Equipartition magnetic field, estimated as described in 2.3.3.
[9] Synchrotron lifetime of electrons assuming an equipartition magnetic field estimated as explained in 2.4.2.

TABLE 2.3: Fitted spectral model parameters for each compact component and derived physical quantities. Columns 2 to 6 give size and estimated surface brightness versus frequency of each component. Columns 7 to 10 give the spectral model fit parameters split into separate rows for the continuous free-free model fits (normal typeface) and clumpy free-free model fits (italics). Values in parenthesis correspond to the estimated uncertainties of the values above. For the clumpy model some of theses values are held fixed (see 2.4.1). Finally columns 11 to 15 give derived physical parameters for the continuous model. Each column is described in the table notes with the respective index number.

ionised gas can readily explain the peaked spectra observed in the radio spectra of the compact components in Arp 299 (Fig. 2.4).

The standard model of radio emission in LIRGs (Condon et al., 1991; Condon, 1992) assumes that both the synchrotron and free-free media are smooth and co-extensive. In Section 2.4.1 I apply this model to fit the observed spectra of the Arp 299 compact components and discuss the results. However, going a step further, it is probable that the free-free emission/absorption in LIRGs is not smooth but is instead concentrated within discrete HII regions (Lacki, 2014). Both Lacki (2014) and Conway, Elitzur, and Parra (2018) have presented spectral models which take into account this fundamentally clumpy nature of the free-free absorbing medium. In Sec. 2.4.1 I fit models based on the clumpy medium formalism of Conway, Elitzur, and Parra (2018) and compare these results to those obtained by fitting the continuous model.

Continuous free-free medium model fitting

The continuous free-free medium model (Condon et al., 1991), following the formulation of Varenius et al. (2016), predicts a radio brightness versus frequency given by

$$S_{\nu,\Omega} = 7.22\,\nu^2\,(T_e/10^4\mathrm{K})\,(1-e^{-\tau_\nu})\,\left[1+{f^{cont}_{th,1\ GHz}}^{-1}\nu^{\alpha^{cont}_{nth}+0.1}\right] \tag{2.3}$$

where $S_{\nu,\Omega}$ is the surface brightness in units of mJy arcsec^{-2}, the frequency ν has units of GHz and T_e is the free electron temperature in Kelvin; $f^{cont}_{th,1\ GHz}$ is the ratio of thermal to synchrotron emission at 1 GHz (assuming both emission mechanisms are optically thin, i.e. ignoring absorption effects); and α^{cont}_{nth} is the non-thermal synchrotron spectral index. Note that some parameters are also marked with a *cont* superscript to differentiate the present continuous case to the clumpy model explained in the next subsection. The free-free opacity versus frequency in this model follows $\tau_\nu = \left(\nu/\nu^{cont}_t\right)^{-2.1}$, where ν_t is the turnover frequency at which free-free opacity through the continuous source medium is unity. If I fix $T_e = 10^4$ K the model has three free parameters (i.e. α^{cont}_{nth}, $f_{th,1\ GHz}$, ν^{cont}_t); with the turnover frequency (Mezger and Henderson, 1967) given by

$$\nu^{cont}_t(\mathrm{GHz}) = \left[\frac{EM^{cont}(\mathrm{pc\,cm^{-6}})}{3.05\times10^6}\right]^{1/2.1} \tag{2.4}$$

where the **E**mission **M**easure (**EM**, EM^{cont} for this continuous scenario) through the source medium equals the integral of n_e^2 through the source where n_e is the thermal electron density.

I used the model given in Eq. 2.3 to fit the spectrum of each compact component, setting the electron temperature $T_e = 10^4$ K and solving for the three remaining free

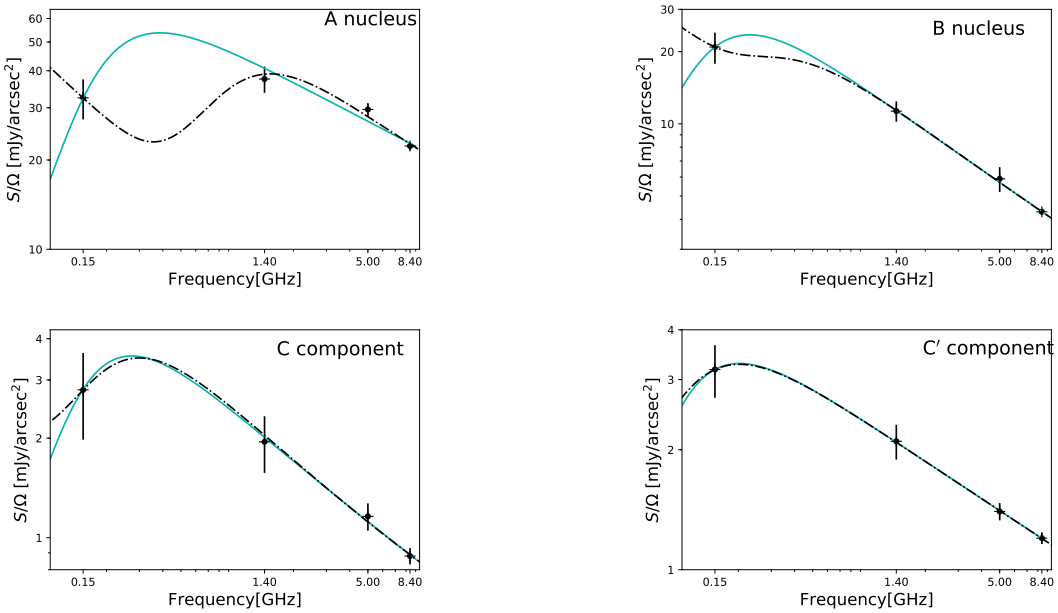

FIGURE 2.4: SEDs of the nuclei in Arp 299. Their sizes are defined by the 50% of the peak in the convolved (1.4 arcsec^2 beam) of 1.4 GHz JVLA image (see Sec. 2.3.2). Solid blue lines and dashed-dotted lines correspond to the best fit to the smooth continuum and clumpy models, respectively.

parameters. I used the Python fitting `lmfit` package to minimize the square of the difference between the data and the different model fits. The results of this fitting are shown in Fig. 2.4 and Table 2.3. Generally the continuous model provides excellent fits to the data with the possible exception of component A. For this component I find that in order to accommodate both the 150 MHz and the higher frequency spectral points a free-free turnover is required at the relatively low frequency of 230 MHz; with the consequence that at 1.4 GHz and above the model spectrum is very close to power-law. The resulting straight high frequency spectrum cannot therefore provide a good fit to the apparent spectral curvature implied by the 1.4, 5 and 8 GHz spectral points.

I also find that our model fitting requires synchrotron spectral indices of -0.33 ± 0.11 and -0.39 ± 0.02 for components A and C′ respectively; i.e. significantly flatter spectral indices than are normally observed in star-forming galaxies ($\alpha_{nth}^{cont} \approx -0.8$; e.g. Herrero-Illana et al. 2017; Pérez-Torres et al. 2021). The flatter spectral indices required for components A and C′ in Arp 299 could be explained (see Sec. 2.3.3) by the effects of Bremsstrahlung and/or ionization loss effects on the energy spectrum of the synchrotron emitting relativistic electrons in dense regions. Such loss mechanisms can flatten the energy spectrum of relativistic electrons at lower energies, in turn giving flattened synchrotron spectra below a critical frequency. Given the relatively high densities

implied by the EM values obtained towards the four compact regions, a flattened spectral index around 1.4 GHz and below is plausible (see Sec. 2.3.3). More exact modelling, which is beyond the scope of this thesis, would take into account the combined effects of bremsstrahlung, ionization and synchrotron losses, which in general are expected to generate a curved synchrotron spectrum rather than one that is a single power-law at all frequencies as assumed by Eq. 2.3. Another potential reason for the relatively flat radio spectral index of the A nucleus could be the existence of an AGN (Pérez-Torres et al. 2010). This AGN is however very faint, about 1 mJy at cm-wavelengths, and it therefore makes a negligible contribution to the overall radio spectral index of the A component.

Fitting of Eq. 2.3 to the four compact components shows that all require similar free-free absorption frequencies close to 0.2 GHz. This implies for each component an EM of $\sim 10^5$ pc cm^{-6} (see Eq. 2.4). This value is more than seven orders of magnitude larger than the EM of the Milky Way (10^{-2} pc cm^{-6}; Nakashima et al. 2018); consistent with the expectation of a much denser ISM in Arp 299. Somewhat surprising however is the similarity of the fitted turnover frequencies between the four components given that they span an order of magnitude in radio surface brightness. The empirically established correlation between radio synchrotron brightness and star-formation rate per unit area, combined with the expectation that the free-free EM also scales with area star-formation rate (Murphy et al., 2011), means that one would expect brighter radio components to also have larger EM values, and hence larger turnover frequencies. Another way to view the same issue is that the fitted 1 GHz thermal fractions $f^{cont}_{th,1\,GHz}$ for the bright sources A and B are only 0.7% and 2% respectively[1] significantly smaller than for C and C′ or for normal star-forming galaxies (∼10%; Condon 1992, Niklas, Klein, and Wielebinski 1997). Such low thermal fractions for A and B compared to C and C′ are forced by the model-fitting because these bright components have large synchrotron brightness at 1 GHz and yet their thermal gas content must be the same as for the weaker components C and C′ because all components have similar turnover frequencies.

The required anomalously low $f^{cont}_{th,1\,GHz}$ in the bright components A and B could theoretically arise because these components have for some reason an overabundance of synchrotron emission relative to their star-formation rates. This explanation is however in conflict with A and B being much brighter in the IR (see Pérez-Torres et al. 2021)

[1]The thermal fraction of component A is comparable to that estimated by Varenius et al. (2016) for the high radio surface brightness east and west nuclei of Arp 220 (thermal fractions 0.8% and 0.4%respectively).

implying that these components have significantly larger star-formation. A more plausible explanation for the low $f_{th,1\ GHz}$ fractions in A and B is that the synchrotron emission closely follows star-formation rates, but that the free-free Emission Measure (EM) is partially suppressed in these bright components. A possible reason could be dust absorption, as suggested by Barcos-Muñoz et al. (2015) to explain a similar suppression of free-free emission in Arp 220. Dust absorption in dense regions could reduce the number of high energy photons available to ionize gas, which in turn reduces the EM and the turnover frequency.

In summary, I find that the continuous free-free absorption model provides excellent fits to the spectral data for the four compact components. These fits require however that for the bright components A and B a mechanism (possibly dust absorption of ionising photons) must operate to suppress the amount of free-free emitting/absorbing gas. Additionally in two components (the brightest component A and in component C') relatively flat synchrotron spectral indices (i.e. -0.33 and -0.39 respectively) are required. Such spectral indices could however be explained by the effects of Bremsstrahlung and ionization losses in these dense regions.

Clumpy HII region free-free medium model fits

Lacki (2013) has argued that in (U)LIRGs free-free gas is confined within discrete compact HII regions surrounding high mass stars or Super Star Clusters. Such a physical origin for thermal gas contrasts with the assumption of the continuous free-free absorption model fitted in Sec. 2.4.1. Nevertheless it can be shown (see Conway, Elitzur, and Parra 2018 and Appendix A) that the continuous model provides a good approximation to the emerging spectrum as long as individual clumps remain optically thin down to the lowest frequency observed.

In this section, I present fits to the observed compact component spectral data using a model that explicitly takes into account the effects of clumping and which therefore applies even when individual clumps are optically thick. Appendix A uses the formalism of Conway, Elitzur, and Parra (2018) to derive an expression Eq.A.4 for the clumpy spectrum. For fixed electron temperature this expression has four free parameters, three of which are shared with the continuous case, namely the thermal/synchrotron ratio at 1 GHz, $f^{clum}_{th,1\ GHz}$, the synchrotron spectral index α^{clump}_{nth}, and the frequency ν^{clump}_{t} at which total free-free opacity through the clump population is unity (roughly the turnover frequency). The fourth free parameter is N_{cl} the mean number of clumps intercepted per LOS. As described in Appendix A above the frequency at which individual clumps becomes optically thick i.e. ($\nu_{turn-up} = \nu^{clum}_{t} N^{(-1/2.1)}_{cl}$) the clumpy medium spectrum closely tracks that of a continuous medium spectrum which shares

the same values of $f_{th,1\,GHz}^{clum}$, α_{nth}^{clum} and ν_t. However at the frequency $\nu_{turn-up}$ the emission reaches a local minimum, below which it increases again, eventually becoming power law with spectral index α_{nth}^{clum} (see as an example the spectrum for component A in Fig. 2.4).

I fitted the observed spectra of the compact components in Arp 299, using the clump spectral model of Eq. A.4. The four free parameters of the clump model equal the number of spectral points to fit so that if all parameters are adjusted the fitting has no degrees of freedom. In order to stabilize the fitting and not to be too sensitive to noise I therefore chose to fix the one of the parameters and fit for the other three parameters. For components A, B and C I fixed the spectral index at $\alpha_{nth}^{clum} = -0.6$ (acceptable fits were found for all $\alpha_{nth}^{clum} > -0.5$) which is in the range of synchrotron spectral index typically observed in star-forming galaxies). For component C' it was not possible to get a good fit assuming this spectral index so instead the number of clumps per LOS was fixed at $N_{cl} = 5$ forcing a solution similar to the continuous model.

The best fitting clump models are shown by the dashed-dotted lines in Fig. 2.4, which use the model parameters shown in italics in Table 2.3. The clump fits shown for components A and B are quite different from the continuous models for these components, showing a significantly larger initial turnover frequency, followed at lower frequencies by a spectral 'turn-up' which occurs above the frequency of the LOFAR data point. The clump fits for C and C' are in contrast very similar to the continuous model over the range of the observations. This is because for these components, which have relatively low turn-over frequencies, the clump induced spectral turn-ups occur well below the lowest observed data point. It is interesting to note in Fig. 2.4 how the turnover frequency for the clump models shown decreases as one progress from brighter to weaker components. This is as expected assuming an approximately constant free-free to synchrotron ratio which implies that brighter components have more free-free gas and hence have larger turnover frequencies.

For components A and B it should be noted that there are alternative clump models that provide equally good fits to the data to those plotted in Fig.2.4. These alternative fits like those for C and C' tracking the continuous model closely over the range of frequencies observed and having turn-up frequencies significantly below the lowest observed data point. Since these alternative clump models do not show the expected progression of turnover frequency with peak component brightness, and in any case these have essentially share same physical properties (EM etc) as the continuous models I do not discuss these alternative clump models further.

If one compares in detail the clump fit shown in Fig.2.4 for component A (blue curve) with the continuous model fit from subsection 2.4.1 (dashed black curves) I find

(1) The clump fits gives a better fit to the apparent spectral curvature defined by the three highest frequency points. (2) For the clump case a good solution exists having a synchrotron spectral index ($\alpha_{nth}^{clum} = -0.6$) closer to typically observed values in intense star-forming galaxies (i.e., Basu et al., 2015) than the flat value of -0.33 required for the continuous model. (3) The required thermal fraction for the clump model is 18% compared to the 0.7% for the continuous model. This higher thermal fraction is much closer to the typical value of about 10% found in normal star-forming galaxies. Turning to component B I find that; (1) The clump and continuous fits are equally good. (2) The synchrotron spectral indices are very similar for both models with both being close to values commonly observed in star-forming galaxies. (3) The required thermal fraction is 5% for the clump model rather than the 1.8 % required for the continuous model which again is closer for the clump case to the value commonly observed in star-forming galaxies. Overall the above results show that the clump model fits the spectral data either somewhat better (component A) or equally as well (component B, C and C′) as the continuous model. The thermal fractions derived from the clump model are more similar between components and closer to values typical of star-forming galaxies. Finally, good clump fits can be made assuming (for components A, B and C) a synchrotron spectral index of -0.6 which is more consistent with the normal range observed in star-forming galaxies (C′ however still requires a flat spectral index even in the clump case). While the above arguments broadly support the clump model one notes that alternative explanations exist (see Sect. 2.4.1) within the frame of the continuous model for their somewhat non-standard spectral indices and thermal fractions.

Continuous versus clumpy free-free models

It is interesting to consider possible future observations which could clearly distinguish between the continuous and clump models for A and B. One systematic difference between the two models is in their thermal fractions (for component A these are 0.7% versus 18% for continuous and clump models respectively). This in turn predicts different amounts of flat spectrum high frequency free-free emission in the two cases which could be distinguished via high-frequency VLA observations. Another clear difference in spectral shape for the two models occurs between 150 MHz and 1.4 GHz and this could potentially be distinguished using uGMRT observations at 200, 600 and 800 MHz. Additionally the clump and continuous models predict respectively negative and positive spectral indices at 150 MHz. A spectral index measured internally over the LOFAR HBA observing band should in principle be able to distinguish between these different predictions but the internal data calibration of the present LOFAR data is not of high enough accuracy to do this. Finally there is the possibility of using future LOFAR Low Band Array international baselines observations to observe around

60 MHz. There is a clear prediction from the clump model that at this frequency emission from components A and B should be significantly brighter than at 150 MHz with the continuous model predicting the opposite (Fig. 2.4).

2.4.2 Energy losses and the spectral index of the Arp 299 nuclei

If relativistic electrons are injected with a power law $p = 2.1$ ($N(E) \propto E^{-p}$) and the cooling of electrons is due to synchrotron (and/or **I**nverse **C**ompton, IC) losses, then the index p would steepen by unity, i.e., $\mathcal{P} = p+1$. In the absence of other energy losses, the observed radio spectrum $S_\nu \propto \nu^\alpha$ steepens, and becomes equal to $\alpha = (1-\mathcal{P})/2 = -p/2$. If $p = 2.1$, then $\alpha = -1.05$. However, this is not observed, as indicated in Table 2.3, which shows that all nuclei have radio spectra significantly flatter than $\alpha = -1.0$. Hence, the observed spectral flattening suggests that electrons losses other than radiative losses (synchrotron and IC) are likely affecting the observed spectrum.

To determine the importance of synchrotron cooling relative to other losses, I compare the lifetimes of electrons. The synchrotron cooling timescale for CR electrons emitting at frequency ν

$$t_{\rm synch} \approx 1.4 \times 10^5 \, B_{100}^{-3/2} \nu^{-1/2} \ {\rm yr}, \tag{2.5}$$

where $B_{100} = B/100$ μG is the minimum equipartition magnetic field, B_{eq}, for each of the nuclei in Arp 299, and ν is the critical frequency at which I am calculating the synchrotron lifetime of the electrons, in GHz.

The synchrotron lifetimes of the electrons in the Arp 299 nuclei are in accordance with other studies of LIRGs at similar frequencies (see, e.g. Romero-Cañizales et al. 2011), with the most long-lived ones in the B nucleus at the lower frequencies of LOFAR.

The synchrotron lifetime of the electrons must be compared against escape, ionization, and Bremsstrahlung losses. For Arp 299-A, we know there is a starburst-driven outflow with a speed $v_w \sim (370 - 890)$ km s^{-1} (Ramírez-Olivencia et al., 2018) (see Chapter 3). Winds, whether AGN or starburst-driven, can advect cosmic rays out of their host regions on relatively short timescales. The corresponding lifetime is

$$t_{\rm wind} = h/v_w \approx 2.4 \times 10^5 \, h_{100} \, v_{w,400}^{-1} \, {\rm yr}, \tag{2.6}$$

where $h = 100 \, h_{100}$ pc is the scale height of the nuclear disk, which is about 100 pc for compact LIRGs (e.g. Lacki, Thompson, and Quataert, 2010; Herrero-Illana, Pérez-Torres, and Alberdi, 2012), and $v_w = 400 \, v_{w,400}$ km s^{-1} km s^{-1}. For the magnetic field

values expected to exist dense starbursts like Arp 299-A ($\gtrsim$100 μG and larger), $t_{\rm synch}$ is shorter than even the advection timescale (Eq. 2.6), and therefore escape losses can be neglected, compared to synchrotron losses.

The electron lifetime due to inverse Compton losses can be written as (e.g., Lacki, Thompson, and Quataert, 2010)

$$t_{\rm IC} \approx 5.7 \times 10^8 \, B_{100}^{1/2} \nu_{\rm GHz}^{-1/2} U_{\rm ph,\,-12}^{-1} \, {\rm yr} \tag{2.7}$$

where $U_{\rm ph} = 10^{-12} \, U_{\rm ph,\,-12}$ ergs cm^{-3} is the photon energy density.

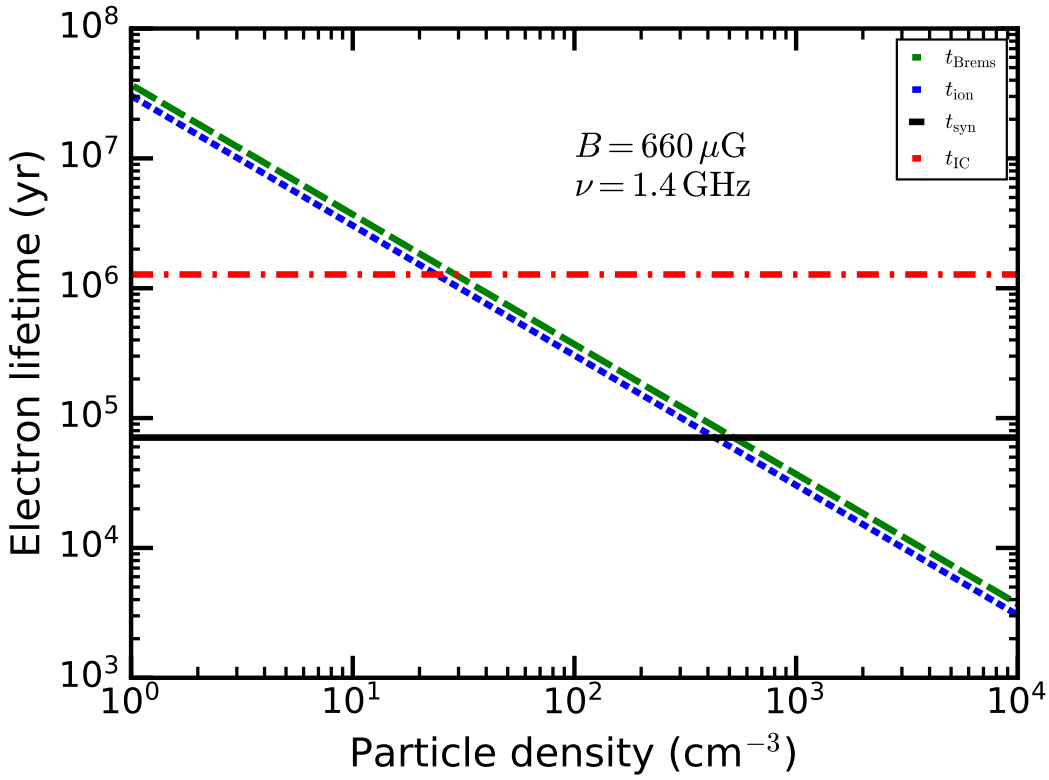

FIGURE 2.5: Lifetime of electrons (in yr) emitting at 1.4 GHz, as a function of the particle number density (in cm^{-3}), and subjected to Bremsstrahlung (long dashes), ionization (short dashes), Synchrotron (solid line), and Inverse Compton (dash-dotted line) losses.Synchrotron an Inverse Compton losses are appropriate for the A nucleus. Note that at low particle densities, which are appropriate for most extra-nuclear regions in galaxies, radiative losses (i.e., synchrotron and IC) dominate, while at high particle densities as those encountered in the nuclear regions of LIRGs, Bremsstrahlung and ionization losses dominate. (See main text for details.)

In LIRGs, synchrotron cooling is expected to dominate over IC cooling. However,

we cannot neglect bremsstrahlung and ionization losses of CR electrons, whose efficiency increases with the density of the ISM. Namely, the bremsstrahlung and ionization energy loss timescales are

$$t_{\rm brems} \approx 3.7 \times 10^7 \, n_e^{-1} \, {\rm yr}, \tag{2.8}$$

and

$$t_{\rm ion} \approx 6.6 \times 10^7 \, B_{100}^{-1/2} \nu_{\rm GHz}^{1/2} n_e^{-1} \, {\rm yr}, \tag{2.9}$$

Bremstrahlung and ionization processes can flatten significantly the equilibrium electron spectra. If Bremsstrahlung losses dominate over all other losses, the injected spectrum is not modified, i.e., $\mathcal{P} = p$, and $\alpha = (1-p)/2$ (Pacholczyk, 1970). For $p = 2.1$, the spectral index would then become $\alpha = -0.55$. Similarly, if ionization losses are the only relevant ones, $\mathcal{P} = p - 1$, and $\alpha = 1 - p/2$ (Pacholczyk, 1970), i.e., $\alpha = -0.05$ for $p = 2.1$. When $t_{\rm synch} = t_{\rm brems}$ at some energy, and all other losses are negligible, then $\mathcal{P} = p + 1/2$ and $\alpha = 1/4 - p/2$ (Lacki, Thompson, and Quataert, 2010). Similarly, when $t_{\rm synch} = t_{\rm ion}$ and there are no other losses $\mathcal{P} = p$ and $\alpha = (1-p)/2$ (Lacki, Thompson, and Quataert, 2010). For $p = 2.1$, I have $\alpha = -0.8$ and $\alpha = -0.55$ when Bremsstrahlung and ionization losses, respectively, are as important as Synchrotron losses.

As an illustrative example, it is shown in Fig. 2.5 the different timescale losses for the A nucleus. For particle densities below $\sim$500 cm^{-3}, synchrotron losses dominate the emission at 1.4 GHz, and therefore the observed radio spectrum becomes steep. However, for particle densities above $\sim$ 500 cm^{-3}, as seems to be the case in Arp 299-A and, most likely, for all other nuclei, Bremsstrahlung and ionization losses can be as important, or even dominate over synchrotron losses, so that the radio spectrum flattens significantly.

Bremsstrahlung and ionization processes can flatten significantly the equilibrium electron spectra. If Bremsstrahlung losses dominate over all other losses, the injected spectrum is not modified, i.e., $\mathcal{P} = p$, and $\alpha = (1-p)/2$ (Pacholczyk, 1970). For $p = 2.1$, the spectral index would then become $\alpha = -0.55$. Similarly, if ionization losses are the only relevant ones, $\mathcal{P} = p - 1$, and $\alpha = 1 - p/2$ (Pacholczyk, 1970), i.e., $\alpha = -0.05$ for $p = 2.1$. When $t_{\rm synch} = t_{\rm brems}$ at some energy, and all other losses are negligible, then $\mathcal{P} = p + 1/2$ and $\alpha = 1/4 - p/2$ (Lacki, Thompson, and Quataert, 2010). Similarly, when $t_{\rm synch} = t_{\rm ion}$ and there are no other losses $\mathcal{P} = p$ and $\alpha = (1-p)/2$ (Lacki, Thompson, and Quataert, 2010). For $p = 2.1$, I have $\alpha = -0.8$ and $\alpha = -0.55$ when Bremsstrahlung and ionization losses, respectively, are as important as Synchrotron losses.

As an illustrative example, I show in Fig. 2.5 the different timescale losses for the A nucleus. For particle densities below $\sim$500 cm^{-3}, synchrotron losses dominate the

emission at 1.4 GHz, and therefore the observed radio spectrum becomes steep. However, for particle densities above ~ 500 cm^{-3}, as seems to be the case in Arp 299-A and, most likely, for all other nuclei, Bremsstrahlung and ionization losses can be as important, or even dominate over synchrotron losses, so that the radio spectrum flattens significantly.

In Table 2.3, the (assumed) spectral index value of $\alpha = -0.6$ in the clumpy scenario would correspond to an injected population of relativistic electrons with $p = 2.2$, which is essentially unaffected by energy losses at our observed frequencies, or only by Bremsstrahlung losses. Alternatively, the smooth, continuous model leads to spectral indices for the nuclei in the range from $\alpha \simeq -0.33$ up to $\alpha - 0.59$. If one neglects all energy losses, as assumed in the clumpy scenario, so that the injected spectrum is not modified, the different spectral indices would imply injected indices for the relativistic electrons of 1.6, 2.12, 2.18 and 1.78 for the A, B, C, and C′ nuclei. While this is a possibility, it seems more realistic to assume the same injected spectrum for all nuclei. If one assumes a standard injected electron index of $p = 2.1$, subject to synchrotron, Bremsstrahlung and ionization losses, the observed spectral indices of the nuclei can be explained within the continuous model by the increasing relevance of Bremsstrahlung and ionization losses due the large gas densities encountered in those regions.

2.4.3 An intrinsic shift in the emission peaks between LOFAR and JVLA frequencies

I determined the positions of the flux density peaks for the compact components at different frequencies in Sec. 2.3.2. As shown in Table 2.2, the position of the peaks of the 150 MHz LOFAR image systematically differ from the position of the same peaks at all other frequencies. Indeed, the position of each peak differs by less than 0.1 arcsec among all JVLA images (see Table 2.4), while it is about 10 times higher between the LOFAR and JVLA bands, and significantly larger than the beam size at any of these frequencies. A plausible explanation for this shift could come from the contribution to the phase solution from the LOFAR phase calibrator, as the point-like quasars used at higher frequencies as phase calibrators might have an extended structure at 150MHz. This would produce an additional contribution to the phase solutions that propagates to the target source image. The magnitude of this error is also in the range of the shifts observed in Table 2.4. However, this shift should be observed with the same orientation for all components, which is not the case (see the different directions of the black arrows of Figs. 2.6, which correspond to the different shift directions). This strongly suggests a physical origin for the observed shift.

As I have discussed in Sec. 2.4.1, I associate the high EM regions with the presence

	Shift [arcsec]			
A nucleus	LOFAR	JVLA-L	JVLA-C	JVLA-X
LOFAR	-	0.25	0.31	0.32
JVLA-L	0.25	-	0.06	0.07
JVLA-C	0.31	0.06	-	0.02
JVLA-X	0.32	0.07	0.02	-
B nucleus				
LOFAR	-	0.45	0.46	0.47
JVLA-L	0.45	-	0.02	0.03
JVLA-C	0.46	0.02	-	0.01
JVLA-X	0.47	0.03	0.01	-

TABLE 2.4: Shift in the flux density peaks between pairs of frequencies for each component of Arp 299.

of dense ionised clouds formed at the heart of the star forming regions. Given the compact nature of the synchrotron sources (SNRs), the intrinsic synchrotron emission at any frequency, from LOFAR to the VLA frequencies, should come from the same location. However the observed low-frequency peak is located at a different position than the peak at the higher frequencies due to the absorption by the ionized medium. The peak observed at 1.4, 5 and 8,4 GHz is located at the maximum of the intrinsic emission, whereas the low-frequency peak is located where the effect of the absorption is minimized, shifted with respect to the higher frequencies.

2.5 Summary

In this chapter, I presented the first subarcsecond (0.4"$\sim$100 pc) image of the whole Arp 299 system at 150 MHz ever. The high-surface brightness sensitivity of our LOFAR observations ($\sim$100 μJy/beam) allows us to detect all of the nuclear components detected at higher frequencies, as well as the extended, steep-spectrum emission surrounding the nuclei. Our deep, sub-arcsecond angular resolution LOFAR observations allowed us to trace in detail the radio emission from the nuclear regions up to largest, several kpc scales, at a spatial resolution better than 100 pc. The brightest components correspond to the well-known nuclei A and B (which have identified AGNs), as well as to the compact components C and C'. W note, however, that most of the 150 MHz emission comes from diffuse, extended structures.

I presented also some of the deepest, high-angular resolution JVLA observations of Arp 299 at 1.4, 5.0 and 8.4 GHz. By combining the LOFAR and the JVLA data sets, I obtained spatially resolved, two-point spectral index maps for the whole galaxy. The

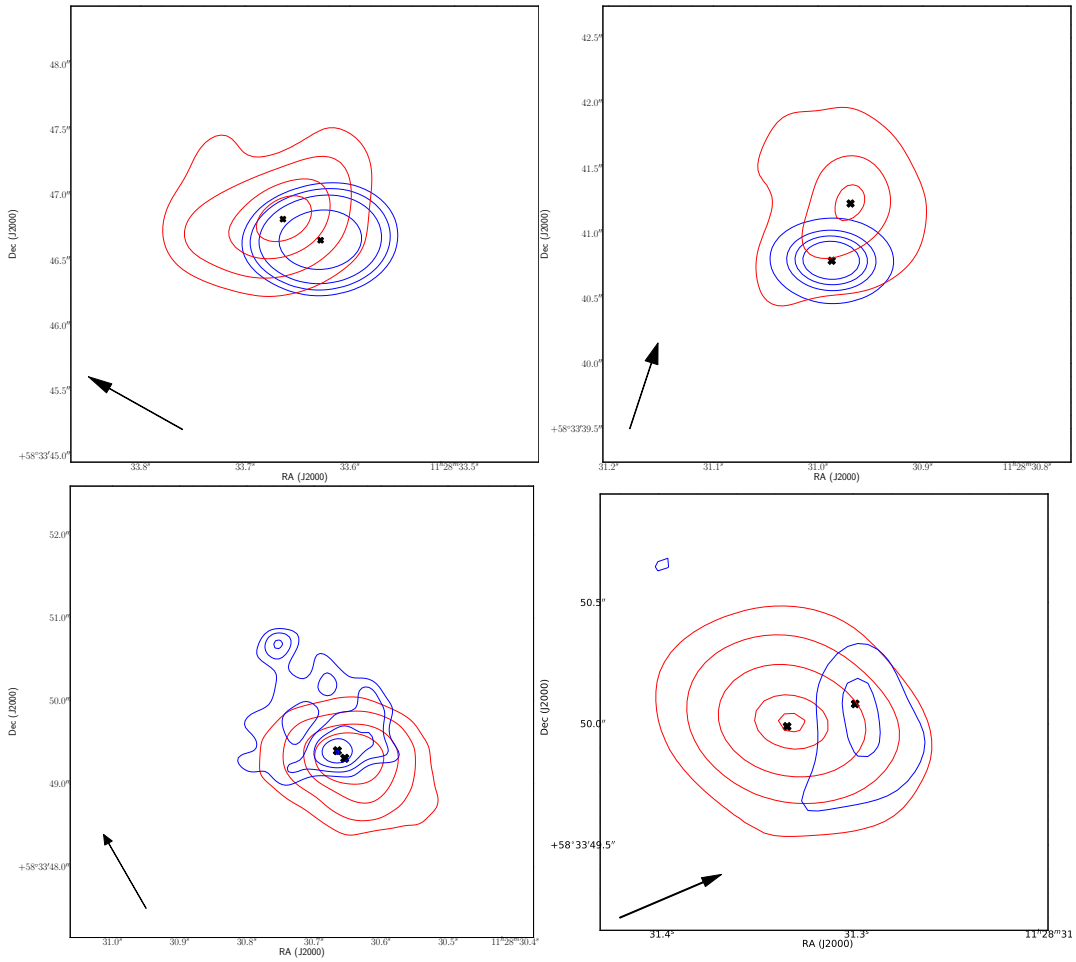

FIGURE 2.6: Contour plots of Arp 299-A, (top left), and Arp 299-B (top right) nuclei, and (bottom left) C and (bottom right) C′ compact component. Red and blue contours represent the local brightest values at 150 MHz and 8.4 GHz, respectively. Black crosses pinpoint the location of the maximum for each frequency. Black arrows represent the directions of the shifts.

main result is that the compact nuclei show relatively flat spectra nuclei, while the extended, diffuse component shows a steep spectrum. The diffuse emission shows a two-point synchrotron spectral index between 150 MHz and 1.4 GHz, $\alpha \approx$ -0.7, typical of star-forming regions.

I also used our LOFAR and JVLA observations to fit the radio SED of the nuclear regions, using two different models of the free-free absorbing/emitting thermal gas: distributed in respectively a smooth continuous medium and a clumpy medium. Both models fit well the existent data. The smooth, continuous model can explain the SED of the nuclei by a standard injected population of relativistic electrons subjected to synchrotron, Bremsstrahlung and ionization losses. The clumpy model can explain the

data by a population of relativistic electrons with negligible energy losses, and yields thermal fractions that are more typical of star-forming galaxies, compared to the continuous model. To unambiguously discern between these two models, we suggest to carry out LOFAR observations at frequencies shorter than 100 MHz, or uGMRT observations at frequencies below 1 GHz.

I also found an intrinsic shift between the emission peaks of LOFAR and those at JVLA frequencies in the A nucleus. The direction of the shift aligns well with the average direction of the outflow in the A nucleus, which may suggest that the dense ionized star-forming nuclear regions of the NGC 3690-A disk are collimating the outflow. We also find that the direction of the shift in the B nucleus is nearly coincident with that of the (suggested) outflow.

All of the above results confirm the usefulness of combining spatially resolved radio imaging at both MHz and GHz frequencies to characterize in detail the radio emission properties of LIRGs from the central 100 pc out to the kiloparsec, galaxy-wide scales.

3 Outflows in Arp 299

3.1 Introduction

Feedback in the form of nuclear outflows driven by star formation or active galactic nuclei is a key component of galaxy evolution, and therefore the study of outflows is relevant to understand their role in galaxies across cosmic time. While discovering outflows is currently easier than in the past, thanks to the availability of new techniques and the increase in sensitivity of essentially all instrumentation, unveiling the nature of those outflows is not trivial. For example, discerning the source responsible for the outflow structure in a U/LIRG is very difficult, as it is usually hidden behind large amounts of dust in their nuclei.

In this chapter, I present evidence of a nuclear outflow in Arp 299A (host to a very prolific supernova factory) discovered from LOFAR observations, and driven by star-formation. This is the first outflow ever detected at such low frequencies, which opens a new window to the study of this phenomenon in galaxies. I also show the possible existence of an AGN-driven outflow in the nucleus of Arp299B, which is known to host a Low-Luminosity AGN (LLAGN).

3.2 Observations

The 150 MHz images showed in this chapter correspond to an extract of the LOFAR image showed in Chapter 2, and we refer the reader to that chapter for a detailed description of these data.

We also used archival Na I line absorption data of Arp 299-A taken with INTEGRAL, a fiber-based integral field system (Arribas and Colina, 2003), on 3 May 2014. INTEGRAL is connected to the Wide Field Fibre Optic Spectrograph (WYFFOS; Bingham et al. 1994) attached to the 4.2m WHT in La Palma. The setup was the R120, the four exposures from the ING (Isaac Newton Group) archive at the Cambridge Astronomy Survey Unit (CASU) of the Astronomical Data Centre (ADC). The exposures were median combined and different spectra were extracted from the nucleus and from an adjacent region.

3.3 Results and Discussion

We show in Figure 3.1 the Arp 299-A image ($0.44 \times 0.41\,\mathrm{arcsec}^2$) obtained from our LOFAR $150\,\mathrm{MHz}$ observations. The rms achieved is $\approx 90\,\mu\mathrm{Jy\,beam}^{-1}$. The peak of brightness of the image is located at R.A. = $11^{\mathrm{h}}28^{\mathrm{m}}33.487^{\mathrm{s}}$ Dec. = $+58\circ33'47.044''$ (J2000.0), with a value of $21.5\,\mathrm{mJy\,beam}^{-1}$, and corresponds to the brightest point in the entire Arp 299 system.

The low-surface-brightness component (which we define as regions with signal-to-noise $3\sigma < \mathrm{S}_{150\,\mathrm{MHz}} < 50\sigma$) of the image accounts for 40% of the extended emission of the entire galaxy, and is about four times more luminous than the A nucleus (which we define as the region with signal-to-noise $> 50\sigma$.) The distribution of this emission forms a biconical structure with an extension $\approx 14\,\mathrm{arcsec}$ in length and a maximum width $\approx 8\,\mathrm{arcsec}$. The Northern region shows edge-brightening. On the contrary, the Southern region this behavior has no edge-brightening, but shows a more uniform emission distribution.

3.3.1 An outflowing wind in Arp 299A unveiled with LOFAR

The most remarkable finding of our 150 MHz LOFAR observations is an intriguing two-sided, wide filamentary structure emanating from the A-nucleus that extends up to at least 14 arcseconds ($\simeq 3$ kpc) from the A-nucleus in the N-S direction. The peculiar shape of this extended emission is very suggestive of an outflow (e.g., Su, Slatyer, and Finkbeiner 2010; Barcos-Muñoz et al. 2017; McKinley et al. 2018). The northern part of the structure appears less obscured.

This structure is consistent with a bipolar structure emanating from the center of an inclined absorbing galactic disk. Since the disk most likely hosts star-forming regions with ionized gas (HII regions), these would produce free-free absorption (Condon, 1992), which would extend down to $150\,\mathrm{MHz}$. This behavior also indicates that,

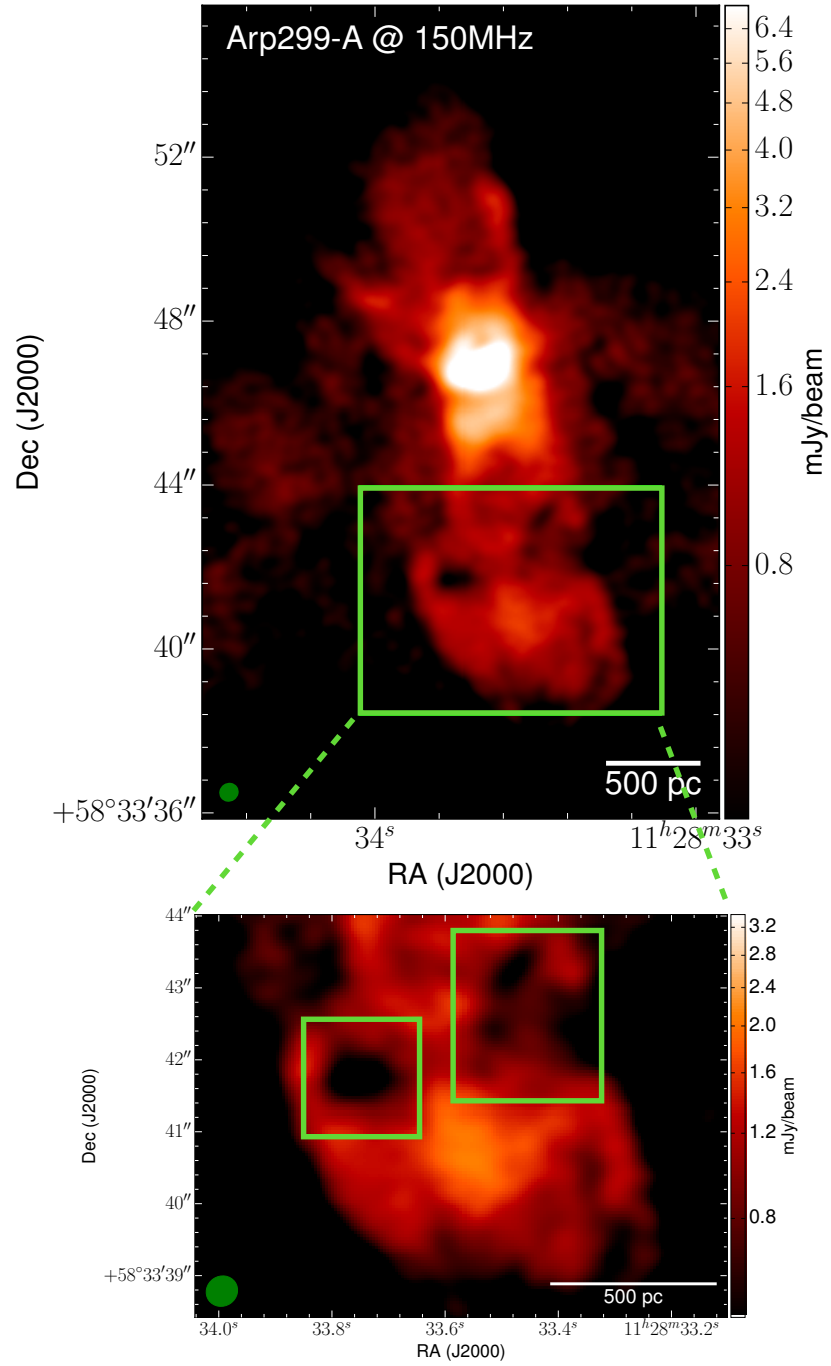

FIGURE 3.1: *Upper panel:* LOFAR Image of Arp 299A at 150MHz with a beam of 0.44 × 0.41 arcsec^2 (Position Angle = $-51.88°$) and a sensitivity of $\mathrm{rms} = 90\,\mu\mathrm{Jy\,beam}^{-1}$. *Lower panel:* Zoomed image of the region of $\approx 1.2 \times 1.6$ kpc marked with a green box in the upper panel. The absorbed regions of the southern part of the outflow are indicated with green boxes. The sizes are approximately $330\,\mathrm{pc} \times 380\,\mathrm{pc}$ (left) and $420\,\mathrm{pc} \times 500\,\mathrm{pc}$ (right).

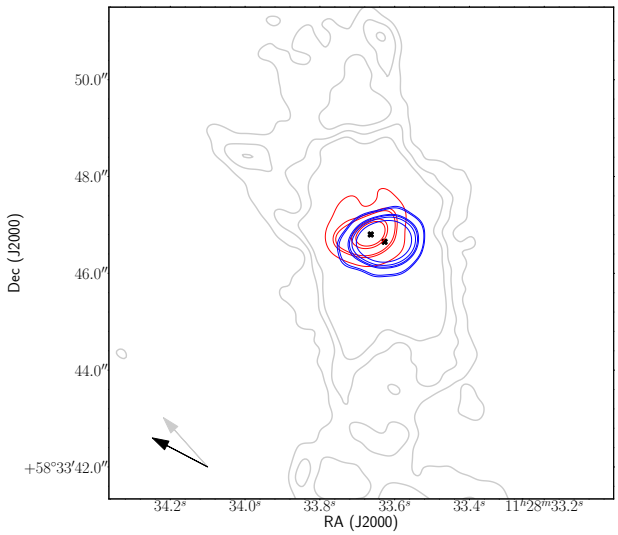

FIGURE 3.2: Contour plots of Arp 299-A. As in Chapter 2, red and blue contours represent the local brightest values at 150 MHz and 8.4 GHz, respectively, and black crosses pinpoint the location of the maximum for each frequency. It is also traced the values that shape the starburst driven outflow for A-nucleus detected at 150 MHz by LOFAR (see Ramírez-Olivencia et al., 2018). Arrows represent the directions of the shift (black) and the outflow (grey).

although the predominant star formation activity is located at the nuclei of the interacting galaxies, ongoing star formation is also present in the spiral disk. This was also previously suggested for Arp299 by Alonso-Herrero et al. (2000) in particular, and in other interacting galaxies in general (M81 of the M81 group, Kaufman et al. 1989; Casasola et al. 2007; NGC 3627 of the Leo Triplet Smith et al. 1994; Paladino, Murgia, and Orrù 2009). Therefore, considering all the above, everything suggests that this structure is an outflow. Moreover, the direction of the intrinsic shift between the peak of brightness at different frequencies is coincident with the average direction of the starburst-driven outflow in Arp 299-A (black and grey arrows, respectively, in Fig. 3.2, left. This may suggest that the dense ionized star-forming nuclear regions belonging to the Arp299-A disk are collimating the outflow.

In Figure 3.3, we present NICMOS/HST H_2 (2.12μm) and FeII ($1.644\mu m$) emission-line images from Alonso-Herrero et al. (2000). The images represent the same region of Arp 299-A, using a logarithmic color scale to enhance the faint, extended emission. The structures present in both images also trace a bi-conical behavior of the extended emission similar to that seen in our 150 MHz LOFAR image, reinforcing the idea that the structure seen at such different frequencies is real, and the emission processes must be related.

The main causes of the ro-vibrational transitions of H_2 are the fluorescent excitation

("UV pumping") and the processes associated with thermal causes (collisions). Moorwood and Oliva (1990) concluded that in a starburst galaxy, as is the case of Arp 299, the most plausible scenario is the one that favors the collisions, for example, the shock of an outflow with the interstellar medium (ISM). On the other hand, the existence of [FeII] emission could be associated with both compact objects or extended emission. SNe are responsible for the compact emission, coming from the ionized medium after the shocks produced in the explosions propagate through the ISM, while in the form of extended emission is directly related with nuclear outflows (Greenhouse et al., 1997; Alonso-Herrero et al., 2003).

We focus here on the Northern part to avoid any potential FeII emission from SN shocks inherent to the clumpy disk. The bulk of the emission originates in the nucleus, but there is a very faint structure to the North that follows the same shape as the putative outflow and that is brighter at the edges, thus resembling filaments.This enhanced emission may be the result of FeII emitter stacking, the trigger of a process that favors the FeII or both scenarios combined. As Arp 299-A is an ongoing factory of SNe (Pérez-Torres et al., 2009a), one might ask if the FeII extended emission is the sum of all the generated compact FeII emission plus the winds associated in the region. The presence of this emission up to $2.5\,\mathrm{kpc}$ away from the nucleus, where the bulk of SNe live, cannot be explained by an emission generated by shocked material in the nucleus and transported northwards, emitting Fe II on its way towards the regions of enhanced emission. Even though the outflow is most likely generated by the SN factory present in the nucleus, the Fe II emission observed in the Northern component is most likely coming from shocks produced by the outflow itself.

The filament in the FeII image observed in the NW region matches the edge of the emission in both H_2 and at $150\,\mathrm{MHz}$. The co-existence of H_2 and FeII in the same region indicates that the process behind these lines is an outflow that produces shocks with the ISM in its wake (Moorwood and Oliva, 1990).

Na I absorption in the nucleus: Because of its low ionization potential, the resonant NaI D lines are a good tracer of the neutral ISM. NaI absorption was used in the pioneering work of Phillips (1993) as a probe of a superwind in NGC 1808, and in a systematic study of 32 FIR bright starburst galaxies by Heckman et al. (2000). Moreover, these double sodium absorption lines have been used in the study of outflows in ULIRGS (Rupke, Veilleux, and Sanders, 2005a; Rupke, Veilleux, and Sanders, 2005b). Figure 3.4 shows the spectra around the NaI D lines $\lambda\lambda$5889.95, 5895.92 extracted from the nucleus (blue line) and from an adjacent region (in red). The absorption is redshifted in the outer regions, indicating a large amount of outflowing dense neutral medium.

The spectra are flux normalized in the continuum window 5805-5930 Å.

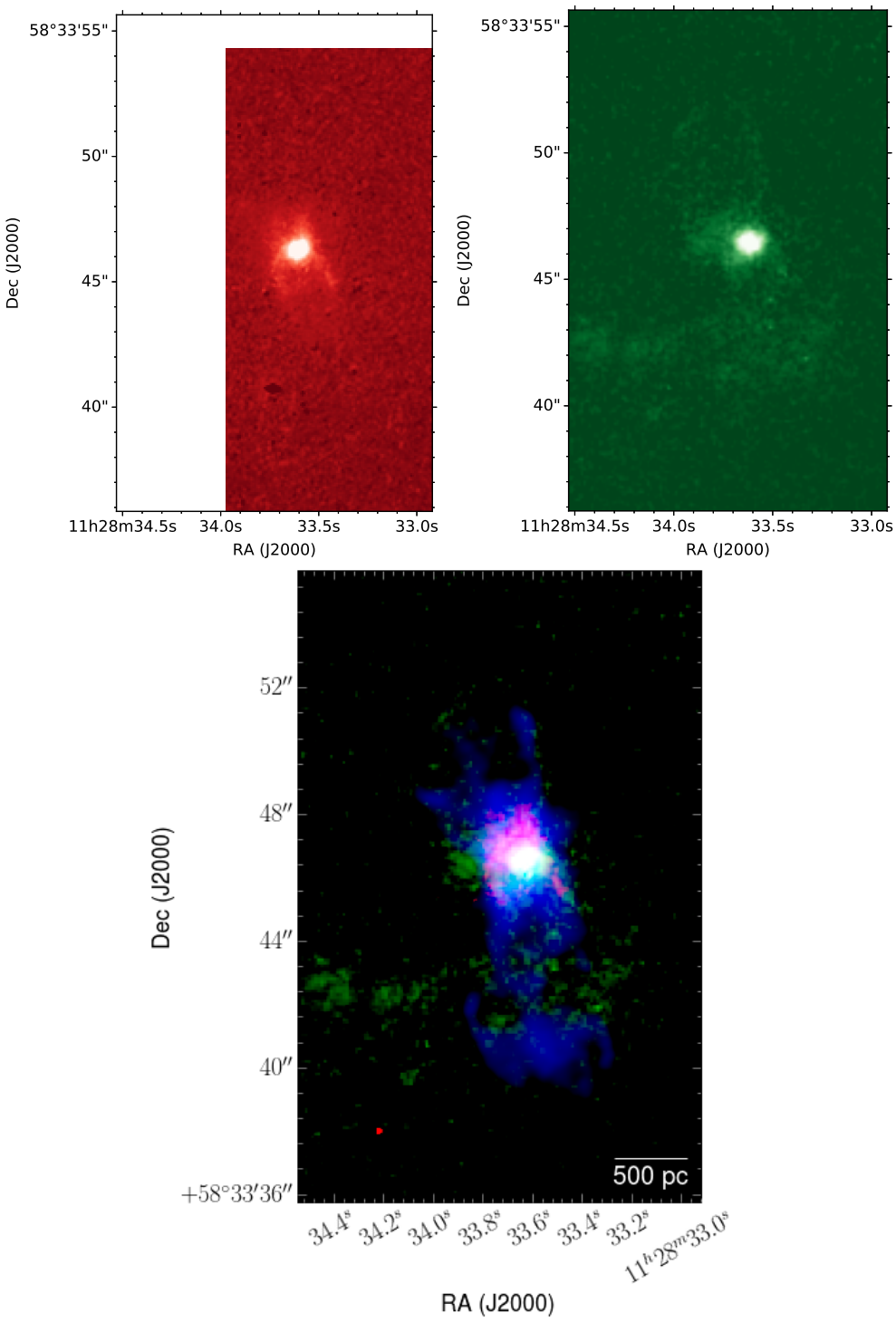

FIGURE 3.3: Images of (a) H_2 and (b) FeII from Alonso-Herrero et al. (2000). H2 is represented in linear scale, while FeII is in logarithmic scale. The H2 image is blanked in the left and upper regions since those regions were not covered by NICMOS observations. The composite RGB image (c) of the same region of Arp 299-A H_2 and FeII , and the LOFAR image at 150 MHz, in red, green and blue, respectively.

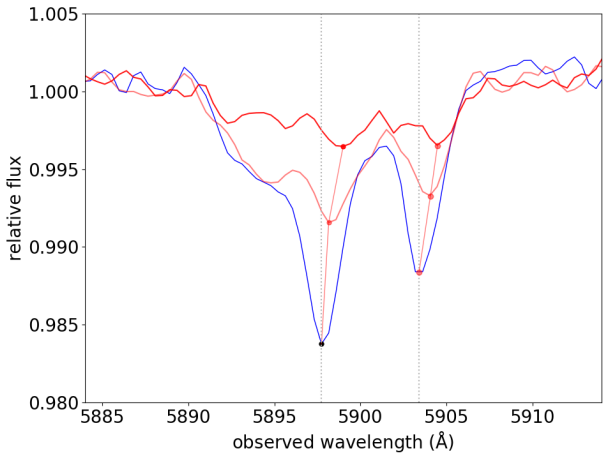

FIGURE 3.4: NaI D lines in the nucleus (blue) and in two adjacent fibers corresponding to outer regions (red). The outer profiles are blueshifted indicating an outflow. Dots indicate the local minimum of the line. Dashed vertical lines indicate the reference wavelength positions of the absorption lines in the nucleus. The spectra is flux normalized in the continuum window 5805 - 5930 Å.

3.3.2 The nature of the outflow in Arp 299-A

There is little doubt that the LOFAR 150 MHz morphology of the extended emission in the central regions of Arp 299-A, in addition to the morphology of the Fe II and H_2 near-IR observations and the Na I D spectra, signals the existence of an outflow in the nucleus of Arp 299-A. Arp 299-A is known to host a low-luminosity active galactic nuclei (LLAGN, Pérez-Torres et al. 2010; Alonso-Herrero et al. 2013) defined as an AGN with $\mathrm{L}(\mathrm{H}\alpha) \leq 10^{40}\mathrm{erg\,s^{-1}}$ (Ho, Filippenko, and Sargent, 1997), although its precise nature (Seyfert or LINER) is still unknown. Further, it also presents a powerful starburst (Pérez-Torres et al., 2009a; Ulvestad, 2009; Bondi et al., 2012) in its nuclear region. Thus, a natural question arises regarding the mechanism that is powering the outflow. Is it the LLAGN in Arp299-A, or is it a compact starburst?

AGNs can drive outflows in the central regions of galaxies, as their accretion power can be very high (e.g., Veilleux, Cecil, and Bland-Hawthorn 2005):

$$\dot{E}_{\mathrm{acc}} \simeq 10^{11}\,\epsilon_{-2}\,\dot{M}_{\mathrm{acc}}\,L_{\odot}, \tag{3.1}$$

where $\dot{\mathrm{M}}_{\mathrm{acc}}$ is the mass accretion rate in $\mathrm{M_{\odot}yr^{-1}}$ and $\epsilon_{-2} = \epsilon/0.01$ is the energy conversion efficiency in rest mass units. The mass accretion rate ranges from ≤ 0.001 $\mathrm{M_{\odot}\ yr^{-1}}$ for low-luminosity AGN, $\sim 1\,\mathrm{M_{\odot}\ yr^{-1}}$ for Seyfert galaxies, and $\sim 100\,\mathrm{M_{\odot}\ yr^{-1}}$ for quasars and powerful radio galaxies (Veilleux, Cecil, and Bland-Hawthorn, 2005).

EVN observations of Arp 299-A showed that Arp 299-A hosts an LLAGN at its center (Pérez-Torres et al., 2010), with $\mathrm{L_{bol}} \approx 6.4 \pm 0.6 \times 10^{43} \mathrm{ergs}^{-1}$ (Alonso-Herrero et al., 2013), surrounded by a large core-collapse supernova factory (Pérez-Torres et al., 2009a). The accretion power of the LLAGN in Arp299-A is unlikely to be larger than $\dot{\mathrm{E}}_{\mathrm{acc}} \simeq 3.8 \times 10^{41} \epsilon_{-2}$ erg s^{-1}, but still might produce outflow phenomena as is the case in, for example, NGC 1433 (Combes et al., 2013), or NGC 1068 (García-Burillo et al., 2014).

We should note that one major problem with the scenario of a LLAGN-driven outflow for Arp299-A is the orientation of the jet. We know from our previous EVN observations (Pérez-Torres et al., 2010) that the radio jet emanating from the AGN in Arp 299-A is oriented along the East-West direction, while the outflow unveiled by LOFAR is in the North-South direction, almost perpendicular (in the projected plane) to the AGN jet.

The main alternative scenario is that of a starburst driving the outflow, given the existence of intense supernova activity in the central ~ 150 pc (Pérez-Torres et al., 2009a; Bondi et al., 2012). In the early stages of a starburst, that is, before **C**ore **C**ollapse **S**upernovae (**CCSNe**) start exploding, the main input of mechanical energy into the ISM is through stellar winds, in particular those of Wolf-Rayet stars (Leitherer et al., 1999). However, soon after CCSNe come into play, their mechanical input dominates for starburst ages ≥ 6 Myr (see, e.g., Figs. 108 and 114 of Leitherer et al. (1999). Given that we have direct observational evidence of ongoing CCSNe explosions in the central $\sim$150 pc of Arp 299-A from our own VLBI observations (Pérez-Torres et al., 2009a; Bondi et al., 2012) and an estimation of 10 - 15 Myr for the starburst age (Alonso-Herrero et al., 2003), we consider here only the mechanical input from CCSNe, for the sake of simplicity. Bondi et al. (2012) found a lower limit to the CCSNe rate in Arp 299-A of $\mathrm{r_{SN}} \geqslant 0.8 \mathrm{SNyr}^{-1}$. Assuming standard values for the energy of CCSN explosions, $\mathrm{E_{SN}} = 10^{51}\,\mathrm{E_{51}}$ erg (where $\mathrm{E_{51}}$ is the energy in units of 10^{51} erg), and for the conversion efficiency of the energy of the explosion into mechanical energy, $\eta = 0.1\,\eta_{-1}$ (Thornton et al., 1998a), we obtain $\dot{\mathrm{E}}_{\mathrm{sb}} \simeq 3.2 \times 10^{42} \mathrm{r_{SN,1}}\,\eta_{-1}$ erg s^{-1}, where $\mathrm{r_{SN,1}} = \mathrm{r_{SN}/yr}^{-1}$. The available mechanical energy due to SN activity is almost ten times larger than that due to AGN activity in Arp 299A, and hence a starburst can account for the observed outflow much more easily than the LLAGN. The maximum outflowing mass-loss rate of a starburst-driven outflow is:

$$\dot{M}_{\mathrm{sb}} \simeq 1000\,\eta_{-1}\,E_{51}\,r_{\mathrm{SN,1}}\,v_2^{-2}\,M_{\odot}\mathrm{yr}^{-1}, \tag{3.2}$$

where $\mathrm{v_2} = \mathrm{v}/100\,\mathrm{kms^{-1}}$ is the outflow speed, in units of $100\,\mathrm{kms^{-1}}$. Starburst-driven outflows show wind speeds of about $400\mathrm{kms^{-1}}$ (Veilleux, Cecil, and Bland-Hawthorn, 2005), so the maximum outflowing mass rate supported by the starburst is $\dot{\mathrm{M}}_{\mathrm{sb}} \simeq 63\mathrm{M_\odot yr^{-1}}$. We can independently obtain another estimate for the starburst mass outflow rate, using the approximation in Veilleux, Cecil, and Bland-Hawthorn (2005):

$$\dot{M}_{\mathrm{sb}} = 0.26\ (\mathrm{SFR/M_\odot\ yr^{-1}})\ \ \mathrm{M_\odot\ yr^{-1}}, \tag{3.3}$$

where SFR is the star formation rate ($\mathrm{M_\odot yr^{-1}}$), solar-metallicity is assumed, and the starburst age is beyond $\sim$ 40 Myr, implying that the mass-loss rate and mechanical luminosity are constant. Assuming, for simplicity, a constant SFR, the CCSN rate for a Salpeter IMF is approximately $\mathrm{r_{sn}} \approx 0.019\,\mathrm{SFR\,yr^{-1}}$ (e.g., Eq. 9 in Pérez-Torres et al. 2009a), and the above expression becomes $\dot{\mathrm{M}}_{\mathrm{sb}} \simeq 13.6\,\mathrm{r_{SN,1}\,M_\odot yr^{-1}}$, or about 11 $\mathrm{M_\odot\,yr^{-1}}$ for the case of Arp 299A. We can now rewrite Eq. 3.2 to obtain the outflow speed:

$$\mathrm{v} \simeq 3200\,\eta_{-1}\,\mathrm{E_{51}\,r_{SN,1}, \dot{M}_{sb}^{-1} km\,s^{-1}}, \tag{3.4}$$

We thus obtain the range of mass outflow rates $\simeq 11 - 63\mathrm{M_\odot yr^{-1}}$. Substituting those values into the previous equation, and using $\mathrm{r_{SN}} \geqslant 0.8\mathrm{yr^{-1}}$ from our VLBI observations, we obtain outflow speeds in the range $\mathrm{v} \simeq 370 - 890\mathrm{kms^{-1}}$, which are in broad agreement with observed wind speeds in starburst-driven outflows (e.g., Veilleux, Cecil, and Bland-Hawthorn 2005).

The range of velocities estimated above, in addition to the physical size of the outflow and the position of the nuclear starburst can help to get an idea of the age of the outflow. However, this length is affected by the projection on the sky of the real outflow, so, primarily, we must deproject it (HyperLeda [1] angle value is $i \approx 52°$). Therefore, the total size of the outflow would be $\approx 5\,\mathrm{kpc}$. Since the compact starburst in Arp299-A surrounds the A nucleus (Pérez-Torres et al., 2009a), the outflow radius is then $2.5\,\mathrm{kpc}$. For the range of velocities obtained above ($370 - 890\,\mathrm{km\,s^{-1}}$), the kinematic age of the outflow is $(3 - 7)$ Myr.

3.3.3 An absorbed disk in the A nucleus

I detected emission in the Southern part of Arp299-A in all our JVLA images arising from three regions of $\sim$300 pc in size (a_1, a_2 and a_3, highlighted with yellow rectangles

[1] HyperLeda: http://leda.univ-lyon1.fr

in Fig. 3.5). Interestingly, the LOFAR image does not show any radio emission above the noise in those regions. If those are star-forming regions, their non-detection at the LOFAR frequencies can be explained by free-free absorption associated with the presence of the interstellar medium ionized by young, massive stars. Since the emission of the Southern part of the outflow is absorbed at 150 MHz by those three regions, this suggests that they belong to the disk of Arp299-A.

This result may have implications regarding the rotation mode of the galactic disk in Arp299-A, which in turn may impact the way bar formation proceeded in this galaxy in particular, and in galaxies in general (Kim and Ostriker, 2007; Seo et al., 2019). Indeed, Pereira-Santaella et al. (2010) suggested, based on spectroscopic observations, that the Western part of the disk of Arp299-A moves away from us, while the Eastern part moves toward us. However, an inclined disk and its Doppler rotation information is not sufficient to determine the rotation mode of a galactic disk, as the orientation with which one is observing the disk would still remain unclear I represent those two possibilities for the rotation of the disk in Arp299-A in Fig. 3.6: leading mode (left image) and trailing mode (right image).

As mentioned earlier, there are three free-free absorbing regions in the A nucleus (a1, a2 and a3, Fig. 3.5). For a1 and a2, the absorption at 150 MHz is observed as a lack of emission, due to the free-free absorption occurring in the knot itself. For a3, the background synchrotron emission of the outflow is absorbed, as well as its own knot emission (the hole of emission in the Southern part of the outflow). This indicates that one is observing the disk from the Northern part (Fig. 3.6, right), and therefore the disk rotation follows the trailing mode.

3.3.4 An AGN-powered outflow in the B nucleus?

One of the most outstanding characteristics of the nuclear region of Arp299-B observed at 150 MHz is its bowshock-like structure (which has not being reported at any other wavelength) surrounding B1 to the north, east and west (Fig. 3.7, grey contours). This bowshock could be also produced by an outflow, emanating from the AGN within the B1 nucleus since it has a well defined synchrotron behavior (see the white contours of Fig. 3.8 lower panel, with values of $\alpha_{1.4GHZ-5.0GHZ}$ of -0.6, -0.65 and -0.7). Supporting this scenario, I refer to observations at other wavelengths that trace AGN shocks. Since the extended emission of the [FeII] infrared line is related with the shocked material due to global nuclear outflows (Greenhouse et al., 1997), I have compared the [FeII] B1 map showed in the background in Fig. 3.8, with the LOFAR counterpart, in white contours. There appears to be weak FeII emission in the structure of the bow-shock seen in LOFAR. This [FeII] emission reinforces the scenario of an outflow or jet interacting with

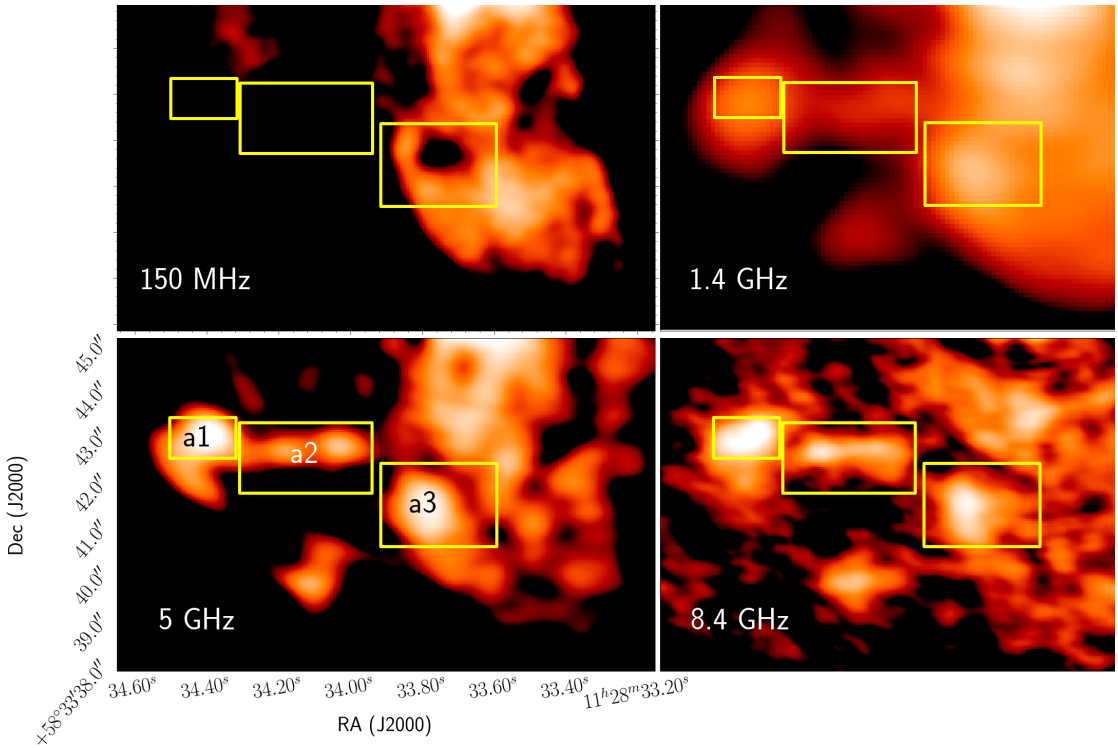

FIGURE 3.5: From left to right, from top to bottom: 150 MHz, 1.4, 5 and 8.4 GHz. They show the southern region of the Arp299-A nucleus. The different regions have been named a_1, a_2 and a_3 and are highlighted with yellow rectangles.

the surrounding medium. Another hint of this bowshock was previously presented by García-Marín et al. (2006), in which the map of the ratio [OI]λ6300/Hα, very sensitive to shocked medium in the optical regime, presents an ionization cone emerging from B1 in the same direction than the observed bowshock. Very recently, a **T**idal **D**isruption **E**vent (**TDE**) has been discovered (Mattila et al., 2018) hidden in the B nucleus. However, one can rule out the scenario in which this bowshock is being produced by the TDE since the TDE-event is very recent (the event started in 2005) and the bowshock is $\sim$500 pc away from the central region (it would require a propagation velocity for the plasma of millions of km/s, which is not plausible). We have previously observed in the Arp299-A outflow that the direction of the shift is ,in average, in the same direction that the direction of the outflow. Looking at the shift observed in the B nucleus, and comparing it with the direction of the plausible outflow (see Fig. 3.7), it is remarkable that it also tends to match. As follows the same behaviour of the confirmed outflow in A-nucleus, it would reinforce the idea of the presence of the B-nucleus outflow as well.

Assuming the existence of an outflow in Arp 299-B1, in order to study its nature, I follow a similar procedure to the case of the A outflow in last chapter (Chap. 2). First, let us discuss the scenario where the outflow is AGN-powered. From the luminosity

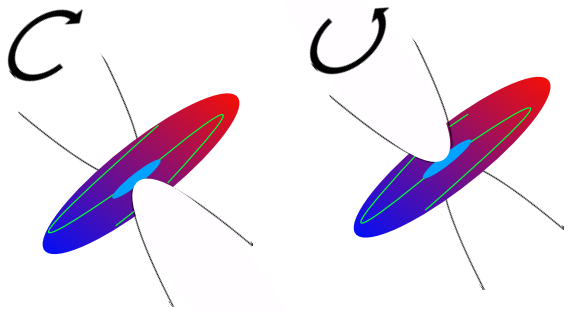

FIGURE 3.6: Sketch of the two scenarios of the disk and the outflow of Arp299-A. The disk is coloured in a gradient from red to blue, to represent the motion away or towards the observer, respectively. In the leading scenario (left), the observer sees the Southern part of the disk, while in the trailing scenario (right), the observer sees the Northern part of the disk. The schematic shape of the spiral arms observed in the optical and near-IR (see Randriamanakoto et al., 2019) has been represented in light green.

of the B nucleus ($L_{bol} = 3.2 \times 10^{44} \mathrm{erg\,s^{-1}}$; Alonso-Herrero et al. 2013), one would obtain an accretion rate of $\dot{M} \approx 0.06 M_{\odot}\, yr^{-1}$. In that case, the energy rate due to the mass accretion would be $\dot{E}_{acc_{B}1} \simeq 10^{11} \epsilon_{-2} \dot{M}_{acc} L_{\odot} \simeq 2.34 \times 10^{43} \mathrm{erg\ s^{-1}}$, able to explain the observed outflow. Alternatively, if the outflow is driven by star formation, the energy rate can be estimated by assuming the core collapse supernova (CCSN) rate of $r_{SN,B1} \simeq 0.3 yr^{-1}$ from Romero-Cañizales et al. (2011). Using a typical SN total energy of $E_{SN} \simeq 10^{51} erg$, and assuming an efficiency of 10% for the conversion of energy of the explosion into mechanical energy (Thornton et al., 1998b), one roughly obtains an energy rate from a starburst of $\dot{E}_{sb} = 9.5 \cdot 10^{41} erg\, s^{-1}$, about 20 times lower than for the AGN-driven scenario. Thus, an AGN-driven starburst seems to be preferred for the B1 nucleus, in contrast with the case of the A nucleus.

Rings of star formation in Arp 299B?

The distance between the nucleus B1 and the observed bowshock at 150 MHz is about 200 pc. In the case that the ISM between the bowshock and B1 has been shocked by the jet in a few Myrs (assuming a typical velocity of 10^2 -10^4 km/s, see e.g. Gupta et al. (2013)), one could search for hints of very recent star formation, with an age of about 1-10 Myr (Calzetti 2013). UV photons can trace the most recent star formation events, but these are rapidly absorbed by dust associated with enshrouded sources, as is the

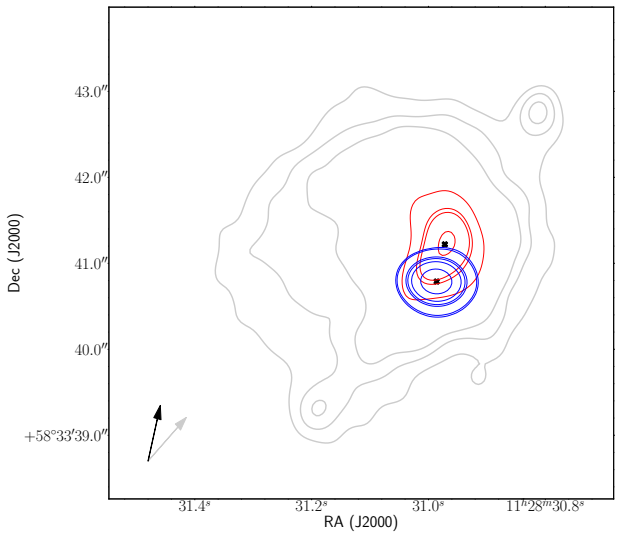

FIGURE 3.7: As in 3.2, blue an red contours correspond to the 150 MHz and 8.4 GHz image of the Arp299-B nucleus. Grey contours show the structure related with the bowshock. Black arrow represents the direction of the intrinsic shit and grey one showed the average direction of the possible outflow related with the observed bowshock.

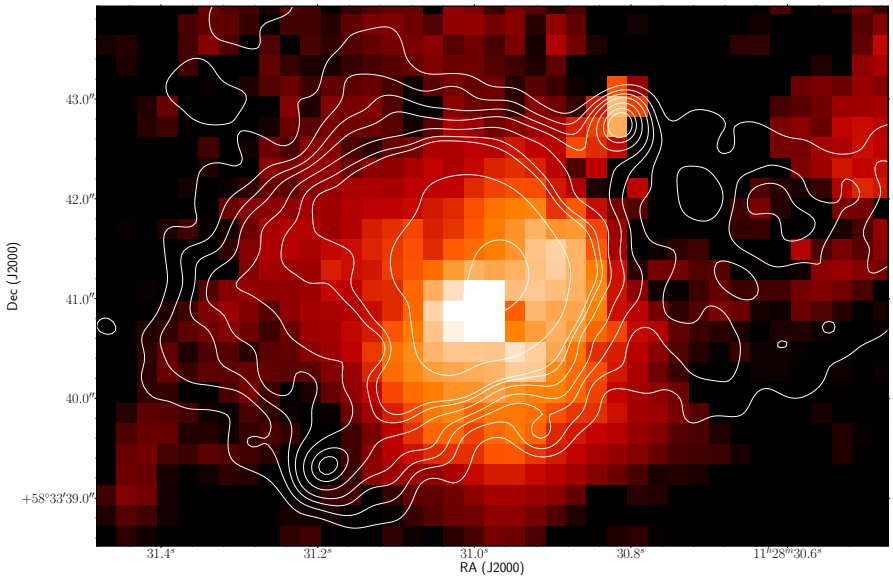

FIGURE 3.8: B1 region. (At the background, continuum-subtracted NIC3 F166N, from Alonso-Herrero et al. (2000)) corresponding to [FeII] emission, and LOFAR at 150 MHz, in white contours.

case of these starburst regions. However, UV photons excite hydrogen atoms and in its decay emits, among others, Paschen lines, which the brightest is Paα, and trace star formation as young as 10 Myrs. This line is a good SF tracer in dense regions since it

is less absorbed than Hα and it is just 8 times less bright. Then, taking the Paα observations from Alonso-Herrero et al. (2000), I confirm that several blobs lie within the region mentioned above. This situation allows us to propose an scenario of a positive feedback of the outflow over the star formation processes (see e.g. Gaibler et al. (2012)). Several studies have already proposed a possible observational evidence of a current jet triggering star formation (Jackson et al. 1998), but these results are still under discussion. However, our results favour the scenario of an observed bowshock generated by an AGN powered outflow (at 150 MHz) while triggering star formation (as shown by the Paα line observations). Other studies have shown evidence of star formation but associated with previous episodes of activity in the jet, including even a star formation in a disk perpendicular to the jet. In our case, the distribution of the star forming blobs detected at Paα line around B1 (B11,B13,B16, according to the nomenclature of Alonso-Herrero et al. (2000), is consistent with a ring-like structure (see the suggested distribution in Fig. 3.9, with the blue rings showing the different location of the star formation episodes). Moreover, this scenario is consistent with the one proposed by Juneau (2011) for the growth of the galaxies and their super massive black holes, where a phase of concurrent SF and AGN activity would be required, as the result of a major merger, as it could be the case of the early stage of merge of Arp 299.

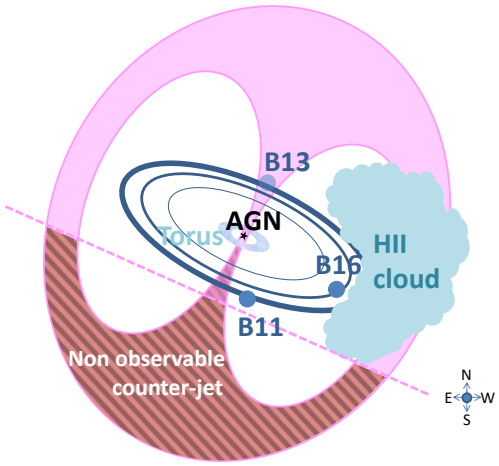

FIGURE 3.9: Sketch of the jet in B nucleus. The thickness of the concentric rings around the AGN and concentric with the torus, indicate the age of the star forming regions (the thicker, the younger). Some of the known brightest blobs in Paα are located in their respective rings, i.e. B11, B13 and B16.

3.4 Summary

In this chapter, I focused on the LOFAR data for nuclei A and B of the merger galaxy Arp 299, paying especial attention at the possible existence of outflows in them. The main findings are the following:

- Arp 299-A shows a two-sided, wide filamentary structure emanating from its nucleus, which is consistent with an outflow that extends up to at least $\simeq 3$ kpc from the A-nucleus along the N-S direction. I discuss two main scenarios to power the outflow, namely that of a starburst, or that of an AGN. The mechanical energy available from the starburst in the central regions of Arp 299-A is very large, $\dot{\mathrm{E}}_{\mathrm{sb}} \simeq 3.2 \times 10^{42} \mathrm{r}_{\mathrm{SN},1}\, \eta_{-1}$ erg s^{-1} due to the large core-collapse supernova rate (Bondi et al., 2012). On the other hand, the mechanical energy due to the accretion power of the LLAGN sitting at the center of Arp 299-A is almost ten times smaller. We thus conclude that the outflow in Arp 299-A is driven by the powerful starburst in its central regions. The starburst wind can support a mass-outflow rate in the range (11 - 63) $\mathrm{M}_{\odot}\mathrm{yr}^{-1}$ at speeds of up to (370 - 890) km^{-1}, and that it is relatively young, with an estimated kinematic age of $(3 - 7)$ Myr.
- There is tentative evidence of the presence of an outflow in the B nucleus from our 150 MHz LOFAR observations. From energy considerations, this outflow is more likely to be AGN-driven, unlike the case of the starburst-driven outflow in Arp 299-A.

These results indicate that sub-arcsecond imaging with LOFAR may be an excellent new tool for unveiling outflows in the central regions of local LIRGs.

4 The LIRGI Sample

ONE of the outstanding milestones in Astrophysics is the determination of galaxy assembly and evolution in the life of the Universe (see Fig. 4.1). To achieve this milestone, a major goal of current and future radio/mm/sub-mm/IR facilities is to use high-redshift galaxies to trace the star-formation history of the universe and its galaxy assembly. One of the most important tools for that purpose is the relation between the radio continuum and IR emission ubiquitously found in galaxies (see, e.g., Pérez-Torres et al. 2021). This relation has to be widely studied in terms of galaxy kinds, AGN hosts and IMF among others.

The e-MERLIN legacy survey **LIRGI**[1] (**L**uminous **I**nfra**r**ed **G**alaxy **I**nventory; P.Is: J.E. Conway and M.A. Pérez-Torres). LIRGI is the high resolution counterpart of the **G**reat **O**bservatories **A**ll-sky **L**IRG **S**urvey (**GOALS**,[2]) program, which encompasses observations from the **HST** (**H**ubble **S**pace **T**eslescope), the Spitzer, and Chandra + **GALEX** (**G**alaxy **E**volution **E**xplorer). The overall goal of LIRGI is to understand better, and comprehensively, the starburst phenomenon in nearby LIRGs as well as the presence of an AGN in its innermost structure, where e-MERLIN can resolve the radio emission of the nuclear region, aiming at extrapolating this understanding to the high-redshift star-forming galaxies, those that were formed in the early life of the Universe.

LIRGI comprises 42 galaxies with infrared luminosities, $\mathrm{Log}(L_{IR}/L_{\odot}) \geq 11.4$) (see Fig. 4.2) in the local universe ($D < 250$ Mpc), and almost all of them are merging or post-merging systems. Half of them are catalogued as H II galaxies (Table 4.1), related with starbursting systems triggered by the presence of tidal forces (Telles and Terlevich,

[1] http://lirgi.iaa.es/content/home
[2] http://goals.ipac.caltech.edu

Galaxy	Type	RA	DEC	D	log(L_{IR})
MCG+12-02-001	?	00 54 04.07	+73 05 05.1	64.28	11.44
CGC 436-030	LINER,HII	01 20 02.63	+14 21 42 .5	122.02	11.63
III ZW 035	Sy2	01 44 30.54	+17 06 08.6	106.96	11.56
NGC0695	HII	01 51 14.36	+22 34 53.6	126.7	11.63
MCG+05-06-036	LINER,HII,Sy1	02 23 21.97	+32 11 48.9	131.71	11.59
UGC02369	HII	02 54 01.81	+14 58 14.9	121.94	11.60
IRAS03359+1523	HII	03 38 47.10	+15 32 53.4	137.11	11.47
VII Zw 031	HII	05 16 46.43	+79 40 13.0	214.83	11.94
IRAS05223+1908	?	05 25 16.26	+19 10 45.7	116.77	11.59
MCG+08-11-002	?	05 40 43.53	+49 41 42.6	77.22	11.41
NGC 2623	LINER,Sy2	08 38 24.08	+25 45 16.6	77.43	11.54
IRASF08572+3915	LINER,Sy2	09 00 25.37	+39 03 54.1	232.19	12.10
UGC04881	LINER,HII	09 15 55.52	+44 19 58.0	161.16	11.69
UGC05101	LINER,Sy1.5	09 35 51.60	+61 21 11.8	158.61	11.95
IRASF10173+0828	Megamaser	10 20 00.21	+08 13 33.9	198.65	11.80
IRAS10565+2448	HII,LINER	10 59 18.14	+24 32 34.4	176.26	12.02
MCG+07-23-019	?	11 03 53.97	+40 51 00	143.21	11.61
IC2810	HII,LINER	11 25 45.09	+14 40 35.9	142.89	11.59
NGC3690/IC694	Sbrst,AGN	11 28 32.50	+58 33 45.00	47.74	11.88
UGC08058	Sy1	12 56 14.24	+56 52 25.1	171.84	12.51
VV250a	HII	13 15 34.96	+62 07 28.8	127.99	11.74
UGC08387	HII,LINER	13 20 35.32	+34 08 22.3	99.99	11.67
NGC5256	Sbrst,Sy2	13 38 17.58	+48 16 36.0	115.83	11.49
UGC08696	LINER,Sy2	13 44 42.13	+55 53 13.5	154.71	12.14
VV340a	HII,LINER	14 57 00.63	+24 37 04.2	139.36	11.67
VV705	HII	15 18 06.12	+42 44 45.1	168.72	11.89
IRASF15250+3608	LINER	15 26 59.42	+35 58 37.4	223.49	12.02
Arp220	LINER,HII,Sy2	15 34 57.22	+23 30 11.5	79.9	12.21
NGC6090	HII	16 11 40.88	+52 27 27.0	122.55	11.51
IRASF17132+5313	HII	17 14 19.79	+53 10 28.6	204.26	11.89
NGC6670	Triple system	18 33 37.35	+59 53 22.9	118.38	11.60
NGC6786	HII,Sy2	19 10 54.29	+73 24 36.4	102.69	11.43
IRAS19542+1110	?	19 56 35.80	+11 19 05.1	256.71	12.04
IRAS20351+2521	?	20 37 17.67	+25 31 40.2	134.85	11.54
CGCG448-020	HII	20 57 24.37	+17 07 39.2	144.1	11.87
IRAS21101+5810	?	21 11 29.48	+58 23 07.5	155.72	11.75
NGC7469	Sy1.5	23 03 15.61	+08 52 26.0	65.23	11.59
IC5298	LINER,HII,SbrstSy2	23 16 00.68	+25 33 24.2	108.19	11.54
NGC7674	HII,Sy2	23 27 56.72	+08 46 44.1	113.64	11.50
IRASF23365+3604	LINER	23 39 01.26	+36 21 08.5	251.84	12.13
IRAS23436+5257	?	23 46 05.51	+53 13 59.5	134.78	11.51
MRK331	HII,Sy2	23 51 26.74	+20 35 10.3	70.46	11.41

TABLE 4.1: Summary of the 42 sources that comprise the whole LIRGI sample

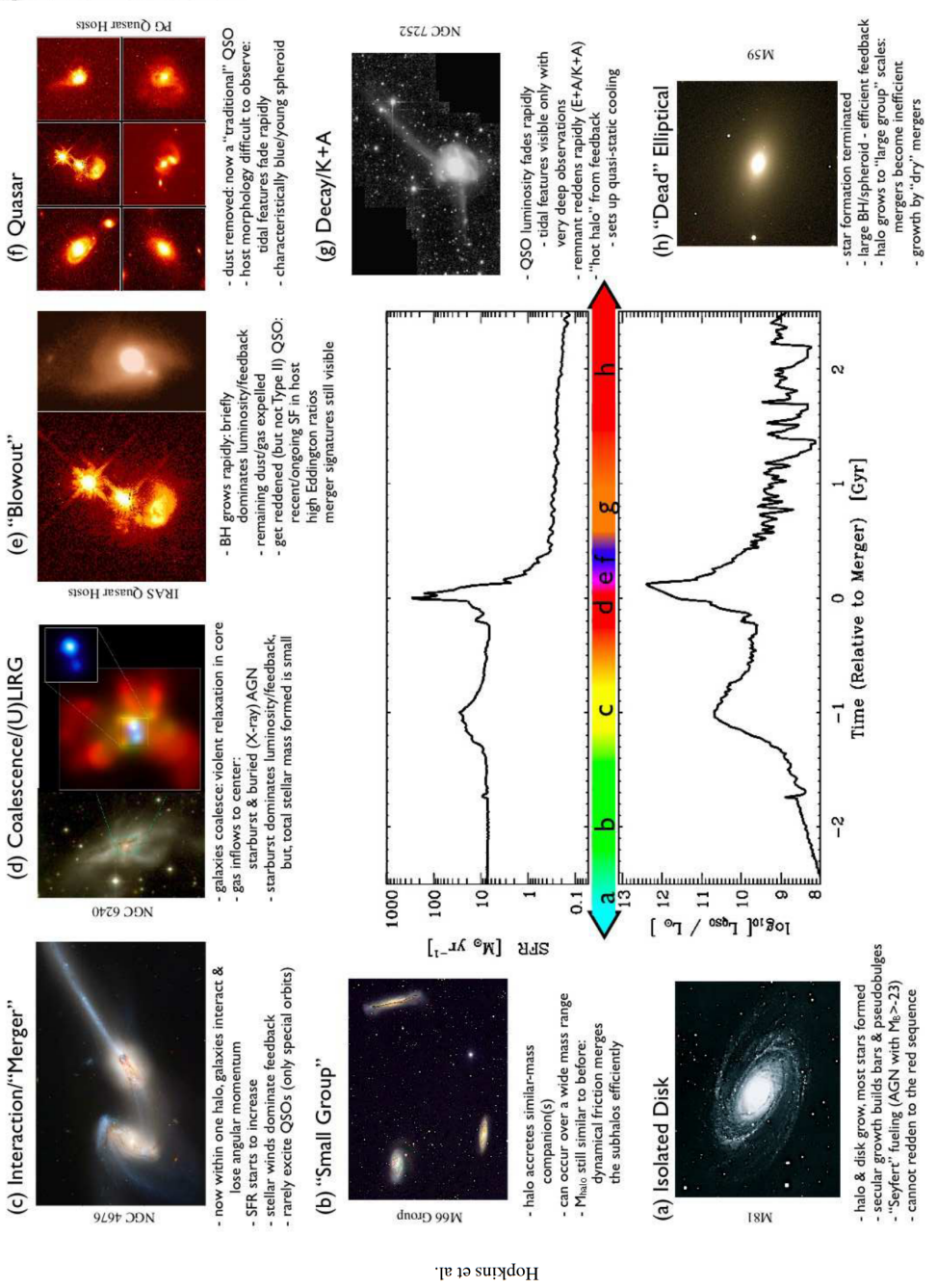

FIGURE 4.1: Evolution sequence from Hopkins et al. (2008)

1995). There are also LINERS and Seyferts (some of them are catalogued as both, Table 4.1), although in a smaller amount than H II galaxies. Many of the properties of the 42 galaxies of LIRGI (e.g., star formation densities, gas and radiation densities) are similar to those of high-redshift star-forming galaxies. Therefore, LIRGI will provide a detailed, resolved view of star-forming galaxies that cannot be obtained at high-redshifts. This is of crucial importance for understanding better star-forming processes, and their impact, in the early stages of galaxy assembly, where LIRGs and ULIRGs where much more common and rival with normal galaxies in their contribution to the star-formation density (Fig. 4.3).

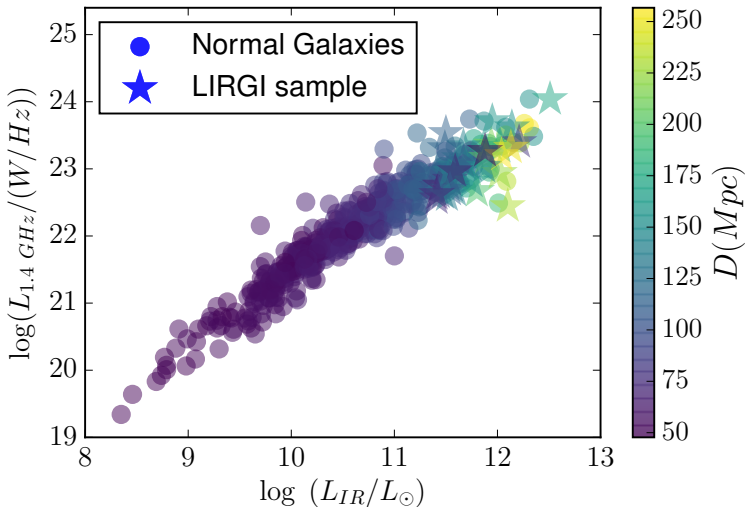

FIGURE 4.2: Far-infrared luminosity versus 1.4 GHz radio emission for normal (i.e., non-AGN dominated) galaxies, from (Yun, Reddy, and Condon, 2001), and the galaxies of the LIRGI sample (stars), which also follow the well-known far-infrared to radio correlation.

I summarize below the immediate goals of LIRGI:

- Observing the morphology and measure the size of the diffuse radio emission regions at 6 and 18 cm (5.0 and 1.4 GHz, respectively). This will trace the star forming regions and their sizes and trace the free-free absorption.
- Detecting core-collapse **R**adio **S**uper**n**ovae (**RSNe**). This will trace the high-mass star-formation rate, which may provide clues about the type of IMF (e.g., normal, Salpeter-like IMF vs. top-heavy).
- Measuring the magnetic field through the analysis of the polarisation and Rotation Measure. This will allow to test whether the magnetic field is weak and in equipartition with relativistic particles or, alternatively, is strong and in equipartition with the thermal gas.

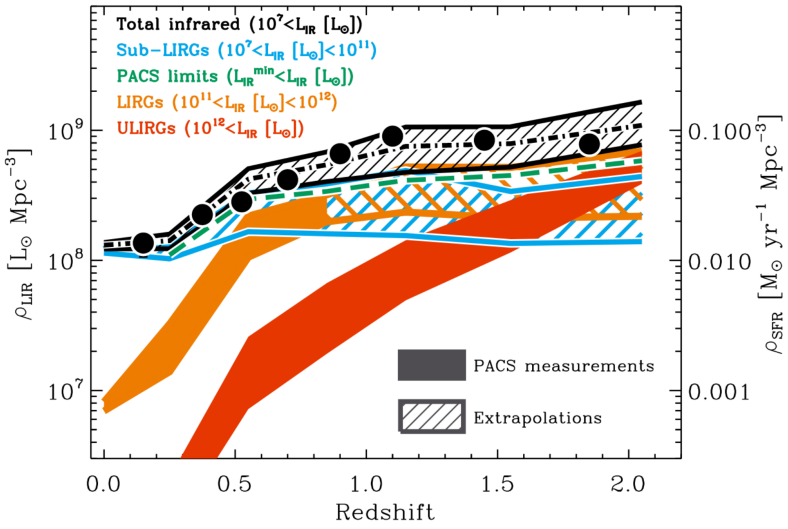

FIGURE 4.3: Figure extracted from Magnelli et al. (2013). Black region represents the evolution of the total comoving IR energy density. Light blue, orange and red regions represents the contribution to this total comoving IR energy density of the "faint" galaxies, LIRGs and ULIRGs, respectively. In this plot, $SFR[M_\odot yr^{-1}] = 10^{-10} \times L_{IR}[L_\odot]$ (more information in Magnelli et al. (2013) and thus vertical left and right axis are directly comparable. Note that U/LIRGs start to contribute >50% in SFR when z>1.

- Determining the gas dynamics and physical conditions through the analysis of the spectral line emission observing absorption/megamaser.
- Detecting jets, lobes and core structures from the dust-enshrouded AGNs at intermediate spatial scales. In this way, eMERLIN perfectly complements the gap between the pc-scales proved by the EVN (e.g., Pérez-Torres et al. 2010), and the hundred-pc scale proved by LOFAR (Ramírez-Olivencia et al., 2018).

More specifically, the scientific contributions coming from eMERLIN include testing standard models of synchrotron/thermal emission from a starburst galaxy, studying the magnetic field of such galaxies to better explain the IR-radio correlation, or the detection of SNe to potentially constrain the IMF. The final goal of LIRGI is to develop a phenomenological sequence of a nuclear starburst. This can be attained by combining the multi-wavelength observations, which include continuum and spectral line information at radio/mm/sub-mm wavelengths, combined with the FIR, optical, and/or X-rays. Since LIRGI includes sources in different merger stages, we should be able to eventually trace the (phenomenological) evolution of a nuclear starburst.

4.1 e-MERLIN - Filling the gap

e-MERLIN has angular resolutions of ∼50 and ∼150 milliarcseconds at C- and L-band, respectively. This fills the gap in angular resolution between JVLA and VLBI observations. We illustrate this in Fig. 4.4, where we show a JVLA image of Arp 299 at C-band, along with, e-MERLIN and EVN imaging of Arp 299 A, also at C-band. Note that eMERLIN fills nicely the gap in between the diffuse structures detected by JVLA and the sharp and compact sources that the EVN is able to detect. We also note that the angular resolution of e-MERLIN results in a range of linear resolutions of ∼11 pc up to ∼61 pc at C-band and of ∼33 pc up to ∼180 pc at L-band, which should allow to disentangle the main dust-heating mechanism in most, if not all, of the LIRGI nuclei: AGN vs. starburst activity. The main indicators of the AGN candidate would be the compactness of the source, its spectral index and the brightness temperature.

As an illustration of the role that e-MERLIN plays in the study of the AGN/starburst phenomenon in LIRGI, we show in Fig. 4.4 a composition of three images of Arp299 at C-band. The JVLA is able to see the whole Arp 299 structure in all configurations, thanks to its large field of view (about 9 arcminutes at C-band). The JVLA is quite sensitive to the extended diffuse emission, and the more sensitive to it, the more compact is the JVLA configuration. However, its resolution at C-band is not good enough, even in its most extended configuration, to unveil the compact, or compact sources responsible for the nuclear radio emission. On the other extreme, VLBI observations filter out all extended emission (beyond just a few milliarcseconds), but can pinpoint very accurately and precisely the location of compact sources in the nuclear regions of LIRGs. e-MERLIN observations complement nicely those extreme cases, by being sensitive to the diffuse emission within the nuclear regions, yet having enough angular resolution to discern the compact emitters. We also note that, although in this image we only focused on the A nucleus (in the e-MERLIN and VLBI images), e-MERLIN has a field of view very similar to that of the JVLA, and therefore all nuclei can be imaged simultaneously.

4.2 Current status of LIRGI observations

e-MERLIN observations of the LIRGI sample at L- and C-band have been performed in the past two years. All of the 42 LIRGI galaxies, except IRAS F23365+3604 and Mrk 331, have been observed at C-band. L-band observations, have been also observed, but the data have not been yet pipelined for most sources. It is expected that the e-MERLIN LIRGI observations will be completed by the end of 2021 or, at the very latest, by spring

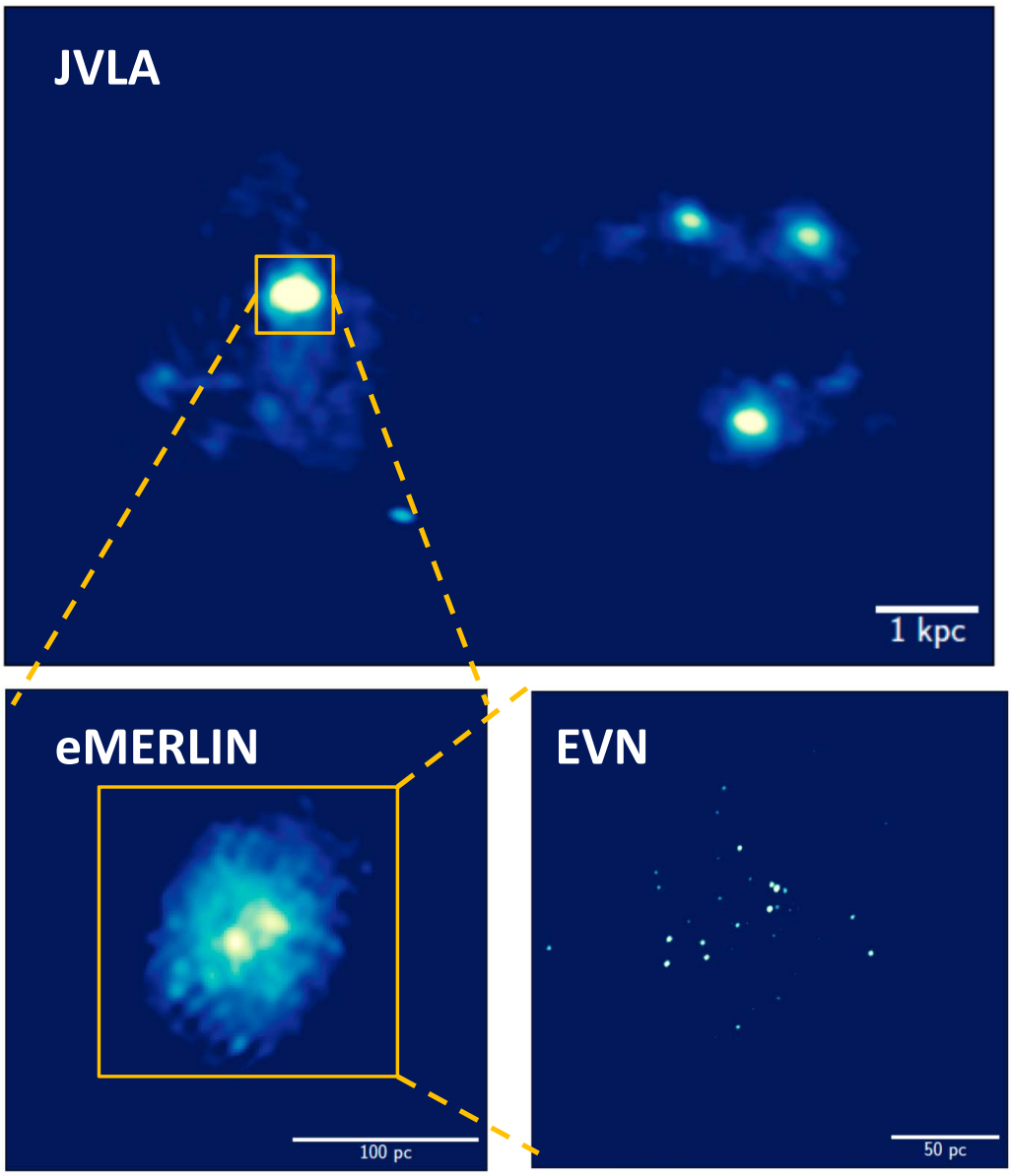

FIGURE 4.4: Composition of three images of Arp299 at C-band. *Top frame:* Whole Arp299 system with the JVLA. *Bottom left:* Central part of Arp299-A with eMERLIN. *Bottom right:* Central part of Arp299-A imaged with EVN (Adapted from Bondi et al. (2012)).

Source	α	δ	State of merger	D	log(L_{IR})
	hh mm ss	$^\circ\ ' \ ''$	Mpc	$L_\odot$	
Arp299	11 28 32.50	+58 33 45.0	III*	44.8	11.89
Mrk273	13 44 42.13	+55 53 13.5	III-IV*	154.7	12.14
Arp220	15 34 57.22	+23 30 11.5	IV*	77.0	12.18
NGC7469	23 03 15.61	+08 52 26.0	II*	65.2	11.59
NGC6670	18 33 37.75	+59 53 22.9	III**	118.4	11.6
IRAS20351	20 37 17.67	+25 31 40.2	IV-V*	134.8	11.54
CGCG448	20 57 24.37	+17 07 39.2	III**	144.1	11.87

TABLE 4.2: e-MERLIN LIRGI sources analysed in this work. * State of merger has been set by its appearance by me, based on the Arribas et al. (2004) approach.** This merger stage is directly taken from Arribas et al. (2004).

2022, including the re-observation of targets that were affected by technical issues or wrong frequency configuration.

The standard calibration procedure of e-MERLIN data involves three different stages.

- Stage 1: Calibration is carried out through the **e**-**M**ERLIN **C**ASA **P**ipeline (**eMCP**) v1.1.19. This out-of-the box calibration allows to ascertain whether the quality is good enough, so that a re-observation of the target sources is not necessary. These data are not suitable for science purposes.
- Stage 2: Manual data flagging and refinement of the pipeline.
- Stage 3: Self-calibration and concatenation of dataset. Data are essentially ready to be used for scientific publication.

We note that e-MERLIN used a mixed observing mode, so that besides obtaining wide-band, continuum C- and L-band products, a number of windows were place around several relevant spectral lines in each band, e.g., around the H I line. However, as is the case for continuum L-band data, all spectral line data (both C- and L-band) remain to be reduced and analyzed.

The continuum C-band images presented in this chapter correspond to observations carried out between December 2019 and March 2020. All C-band observations, together with their co-observed spectral lines, have been calibrated with the pipeline (stage 1), though only a few C-band continuum observations have been also refined (stage 2) and self-calibrated (stage 3).

4.3 Results

In this section and as an example of the potential of the e-MERLIN LIRGI observations, I present the preliminary results of our continuum C-band imaging for seven LIRGI sources, and preliminary results at L-band for two of the sources, NGC 6670 and IRAS 20351.The integrated flux of each compact component (see Table 4.3) has been measured fitting a 2D gaussian with the `fit` tool of CASA viewer over a zoomed region that just contain the compact source one wants to measure. In the case of IRAS20351 and the non-central source of NGC 7469, as there were a diffuse emission with no apparent gaussian look, I have created in CASA viewer a manual ellipse region and I measured the integrated flux inside. As mentioned earlier, C-band e-MERLIN imaging has the power to both resolve most of the compact emission, while tracing to a large extent the diffuse radio emission.

For the classification of the galaxies in terms of their state merger (see Table4.2), I follow the classification addressed in Arribas et al. (2004). The criteria are simplified as following under appearance criteria:

- Class I: the beginning of the interaction. Disks are still intact, and there is no evidence yet of tidal tails or bridges.
- Class II: First contact between galaxies. Disks start to be in contact, but there is no tidal tails.
- Class III: The two nuclei remains identifiable and the structures of tidal tails and bridges are present.
- Class IV: The nuclei are merged in just one nucleus. Tidal tails and bridges still remain.
- Class V: Old merger. Only nuclear turbulence, with just one nucleus and no other sign of the past interaction.

To tell apart thermal from non-thermal radio emitters, I used the brightness temperatures of the unresolved e-MERLIN components in our images, using the following equation:

$$T_b(K) = \left(\frac{S_\nu \nu^{-2}}{\Omega}\right)\left(\frac{c^2}{2k}\right) \approx 1.6\times10^3 \left(\frac{S_\nu}{mJy}\right)\left(\frac{\nu^2}{GHz}\frac{FWHM_a \times FWHM_b}{mas^2}\right)^{-1} \quad (4.1)$$

Here, S_ν is the source peak, Ω is the solid angle, taken as the beam in each image. In this way, $\Omega = \pi\theta_a\theta_b/[4ln(2)]$, where FWHM$_a$ and FWHM$_b$ are the FWHM for the major

and minor axes of the beam ellipse, respectively, measured in mas. ν is the frequency where one is measuring T_b, which is 5.0 GHz in our case, and c and k are the light speed and Boltzmann's constant, respectively, in cgs units. For frequencies ν >1 GHz, $T_b > 10^3$K indicates non-thermal emission, which is fulfilled in all compact components.

4.3.1 Mrk 273: An advanced merger with no radio sign of its second AGN.

Mrk 273 (UGC 8696, IRAS13428+5608) is a ULIRG with $\log(L_{IR}/L_\odot)$=12.21. It is located at D=157 Mpc. It corresponds to a late-merger system with a tidal tail extending over 40 kpc to the south. At near and mid-IR wavelengths, two nuclei are detected (North and South-Western) (Majewski et al., 1993; Knapen et al., 1997; Scoville et al., 2000; Soifer et al., 2000). An additional third nuclear structure, south eastern, emerges at radio wavelengths (Condon et al., 1991; Soifer et al., 2000).

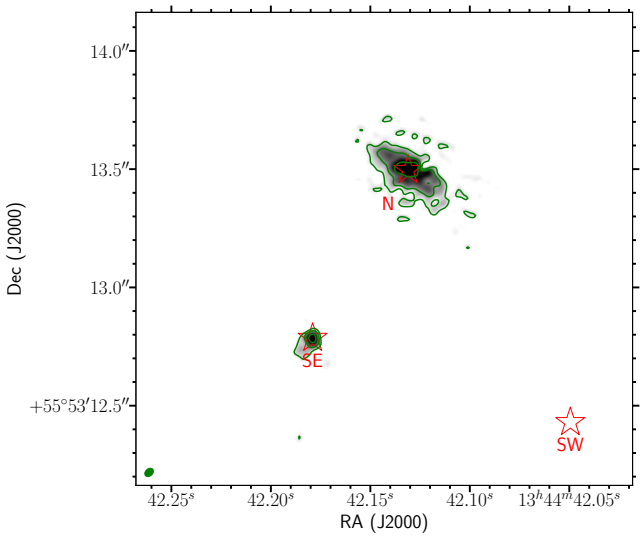

FIGURE 4.5: Mrk 273 at 5.0 GHz with eMERLIN at background and green contours at (5,9,18)×rms. Red stars indicates the peak location of 8.4 GHz observations of Condon et al. (1991). The beam is shown in green (bottom left corner).

In Fig.4.5, I report the detection of the two radio sources previously detected by Condon et al. (1991) with the VLA (A-array) at 8.4 GHz, and by Bondi et al. (2004) [3]. The northern source has an integrated luminosity of L_ν = $35.5\times10^{27} erg\ s^{-1} Hz^{-1}$ and the SE source L_ν=$135\times10^{27} erg\ s^{-1} Hz^{-1}$. Both values are particularly high for a SNR with a certain age. In the case of North source, the emission is diffuse, so the total luminosity can be produced by different SNR of relatively normal values ($L_\nu \sim 10^{27} erg\ s^{-1} Hz^{-1}$).

[3]Coordinates have been previously transformed from B1950.0 to J2000, and finally shifted using the southern eMERLIN source coordinates, since they present a common shift maybe due to an astrometric uncertainty.

Galaxy	Peak	Peak position	T_b	Int. flux	Luminosity	Major axis FWHM	Minor axis FWHM	Beam	rms
	mJy		$\times 10^6$K	mJy	$\times 10^{27} erg\ s^{-1} Hz^{-1}$	mas	mas	mas×mas,deg	μJy
Arp 299-AE	3.8	11:28:33.632, +58.33.46.656	6.7	±2.0	63.9	107±10	102±9		
Arp 299-AW	3.1	11:28:33.620, +58.33.46.698	5.5	29.8±1.5	69.0	126±7	107±6	1.11×9.2,-6.9	57
Mrk 273N	2.4	13:44:42.129, +55.53.13.495	4.5	1.24±0.09	35.5	232±19	112±10	1.14×8.4,-47.7	53
Mrk 273S	1.3	13:44:42.179, +55.53.12.786	2.4	4.72±0.70	135	83±14	59±11		
NGC7469-0	6.3	23:03:15.613, +08.52.26.054	0.5	9.8±1.9	49.8	45±29	31±18	27.4×8.7,24.5	150
NGC7469-jet	2.8	23:03:15.619, +08.52.26.029	0.5	6.2*	31.5	86.7*	55.2*		
Arp 220W	3.0	15:34:57.292, +23.30.11.331	0.4	54.9±2.2	389	316.7±12.9	196.8±8.0	15.1×8.7,-6.9	91
Arp 220E	6.3	15:34:57.222, +23.30.11.498	0.9	65.2±2.5	463	194.1±7.9	132.3±5.9		
CGCG448	0.3	20:57:24.375, +17.07.39.225	0.03	0.89±12	22.1	115±15	41±17	17.7×8.9,25.1	2.6
IRAS20351	0.1	20:37:17.742, +25.31.37.863	0.01	3.82*	83.1	387*	367*	15.3×8.8,27.2	16
NGC6670Ea	0.1	18:33:37.730, +59.53.22.922	0.02	0.25±0.03	4.2	49.0±7.3	25.2±7.7	10.8×9.7,32.7	19
NGC6670Eb	0.1	18:33:37.714, +59.53.22.931	0.02	0.45±0.05	7.6	80.1±10.1	63.7±8.6		

TABLE 4.3: Observational summary. The peak position corresponds to the maximum in the local region. Integrated flux, major axis and minor axis correspond to the fitted flux inside a 2D Gaussian region as obtained in CASA viewer with `tfit`, and luminosity is derived from the integrated flux and the distance in Table 4.1. Note that NGC 6670Ea and NGC 6670Eb refer to the East (a) and West (b) sources detected within the NGC6670E component.

In fact, the north source has been previously reported as a starburst-region (Carilli and Taylor, 2000; Bondi et al., 2005) plus an AGN deeply enshrouded in dust (U et al., 2013). On the other hand, the integrated luminosity found for SE source overcome the typical luminosity values even for the most brightest and recent SN, and present a more compact emission, pointed out to the presence of an AGN. In the image of Mrk273 at 8.4 GHz of Condon et al. (1991), although not reported, there is evidence of some extended emission towards SW, where NIR emission has a clear detection (Scoville et al., 2000). This region, at ∼40 mas of this eMERLIN observations is resolved, with no detection of compact components, pointing to a star forming region with no evidence of AGN, contrary to the scenario of a X-ray absorbed AGN (Iwasawa et al., 2011). The only explanation of the existence of a possible AGN and the non-detection at 5 GHz is a very dense ionised medium that produces a turnover frequency at higher frequencies than 5.0 GHz (see Chap. 2). This scenario would require an EM of $\geq 10^8 pc\ cm^{-6}$, and making the comparison with the EM reached in the study of the SN factory in Arp299-A (see also Chap. 2) with EM$\sim 10^5 pc\ cm^{-6}$, make unlikely the presence of such highly free-free absorbed AGN. So at the light of the observations I can confirm the existence of diffuse emission related with star formation (North source)

4.3.2 NGC7469: A core-jet structure surrounded by a circumnuclear starburst

NGC 7469 (also known as IRAS23007+0836 and Mrk 1514) is an spiral LIRG with log($L_{IR}/L_\odot$)=11.7 (Sanders et al., 2003) located at D = 70.2 Mpc. It is part of a system together with the galaxy IC 5283 (60-70 kpc away, projected distance). It has been reported that the last interaction with this companion happened 1.5×10^8 years ago (Genzel et al., 1995). It contains a luminous Seyfert 1 nucleus surrounded by a dusty circumnuclear starburst of about 1 kpc in size detected at different wavelengths: radio (Colina et al., 2001; Alberdi et al., 2006; Pérez-Torres et al., 2009b), optical (Scoville et al., 2000; Colina et al., 2007) and infrared (Soifer et al., 2003; Díaz-Santos et al., 2007). NGC 7469 is a very luminous infrared galaxy where 2/3 of the luminosity is emitted by the circumnuclear starburst. Moreover, there is evidence for a $10^7\ M_\odot$ central black hole coming from reverberation mapping (Peterson and Wandel, 2000).

NGC 7469 has a SFR[$M_\odot yr^{-1}$]=48 (Pereira-Santaella et al., 2011). On 2000 October 27 a strong compact radio source was detected in the circumnuclear starburst of NGC 7469 (Colina et al., 2001). The flux evolution for the first six months after detection confirmed the source as a radio supernova. It was named SN 2000ft and it was the first radio supernova ever detected in the circumnuclear ring of a Seyfert 1, luminous infrared galaxy and at a distance of 600 pc from the galaxy nucleus. At a distance of

∼65 Mpc, SN 2000ft is one of the most luminous and distant RSNe ever detected. Its flux density evolution was monitored (Alberdi et al., 2006; Pérez-Torres et al., 2009b) and shown to be consistent with the characteristics of a luminous type II supernovae, governed by the interaction between the supernova ejecta and the circumstellar.

Our present observations of eMERLIN at C-band, at the highest angular resolution of 50 mas, show a structure consisting of an elongated galaxy nucleus. The nucleus shows a core-jet structure, with an average integrated flux density of 6.2 mJy within an angular region of 200 mas (64 pc), with the core (probably, the westernmost point-like component) having an average flux density of 9.8±1.9 mJy. The jet consists of two components within diffuse emission abridging both of them. The extended, diffuse emission coming from the circumnuclear starburst is completely resolved out (see Fig. 4.6).

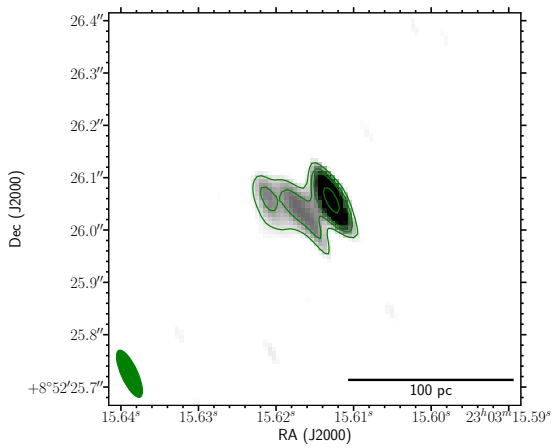

FIGURE 4.6: Both image in background and green contours ([10,15,20,40]×rms, see Table4.3) of NGC7469 observed by eMERLIN at C-band. Beam shape is represented as a green filled ellipse at left corner. The brightest source is named NGC7469-0, and the eastern extended structure, NGC7469-jet (see Table 4.3)

Further observations with eMERLIN at L-band will provide spectral information and confirm the nature of the westernmost component, most probably an AGN. New observations at C-band will permit also to detect proper motions within the relativistc jet. Outflows in this source has been recently reported by Robleto-Orús et al. (2020) and Cazzoli et al. (2020), but none of them has the same orientation than the eMERLIN structure. This will open the door for future discussions on the nature of these outflows.

Alberdi et al. (2008) performed 5 GHz VLBI observations of the nuclear regions of NGC 7469 at 6cm with the European VLBI Network (EVN) (Fig. 4.7) with an angular resolution of 10 mas. The NGC 7469 nucleus consists of at least five compact sources

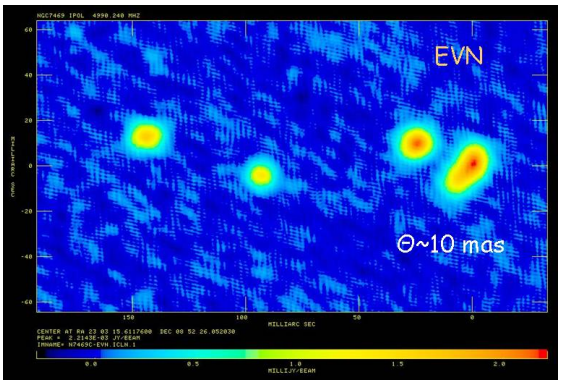

FIGURE 4.7: EVN image of the nucleus of NGC 7469 at 6 cm and 10 mas of resolution. Easternmost source correspond to the eMERLIN C-band brightest source. The other compact sources also correspond to the eastern emission detected with eMERLIN. (*Private communication.*)

located along an east-west line, with no evidence for diffuse emission or a jet-like structure connecting the compact sources. They are contained within a region of 150 mas (50pc) with a total flux density of 10 mJy. Some of the components are unresolved, while the others have evidences for substructure (for example, the westernmost one). It is still unclear whether these components trace the typical core-jet structure of an AGN or, alternatively, we are seeing compact star-forming regions where individual, or clumps of radio supernovae are exploding, or a combination of both, as found in Arp 299. The connection between the east-west core-jet structure mapped with MERLIN at 5 GHz and the milliarcsecond VLBI structure needs further investigation.

4.3.3 NGC 6670E: eMERLIN detection, EVN non-detection.

NGC 6670 consists of two edge-on galaxies (NGC 6670E and NGC 6670W, see both galaxies interacting in Fig.4.8 at background), in a III state of merging, with the two nuclei separated by a distance of 27 arcsec. There is no evidence of tidal tails in the optical (Arribas et al., 2004), being difficult to determine the history of the interaction between both galaxies and the orbital geometry of the system. However, HI tails have been discovered with the JVLA (Wang et al., 1997). In terms of its IR emission is catalogued as LIRG, with a SFR of about $70 M_{\odot} yr^{-1}$. The galaxy is classified as SB or SB/AGN composite (Mudd et al., 2014). Wang et al. (2001) concluded there was no evidence of an AGN neither in West nor East galaxy based on 20 cm radio observations With a 3".1 angular resolution.

Our eMERLIN observations show a slightly distorted disk (the easternmost galaxy, NGC 6670E), tracing a nuclear starburst, and a slightly warped resolved disk (the westernmost galaxy, NGC 6670W), with some faint features within diffuse emission. These

disks are not connected in our eMERLIN images, but appear to touch each other in the sky as seen in images with a lowest angular resolution ((Wang et al., 1997) and HST archive, see i.e. background image in Fig. 4.8). Both galaxies present enhanced star formation in their nuclear regions, as suggested by the high CO brightness temperature, the Far Infrared (FIR) surface brightness and the Star Formation Efficiency (SFE) (see e.g. Wang et al. (1997)).

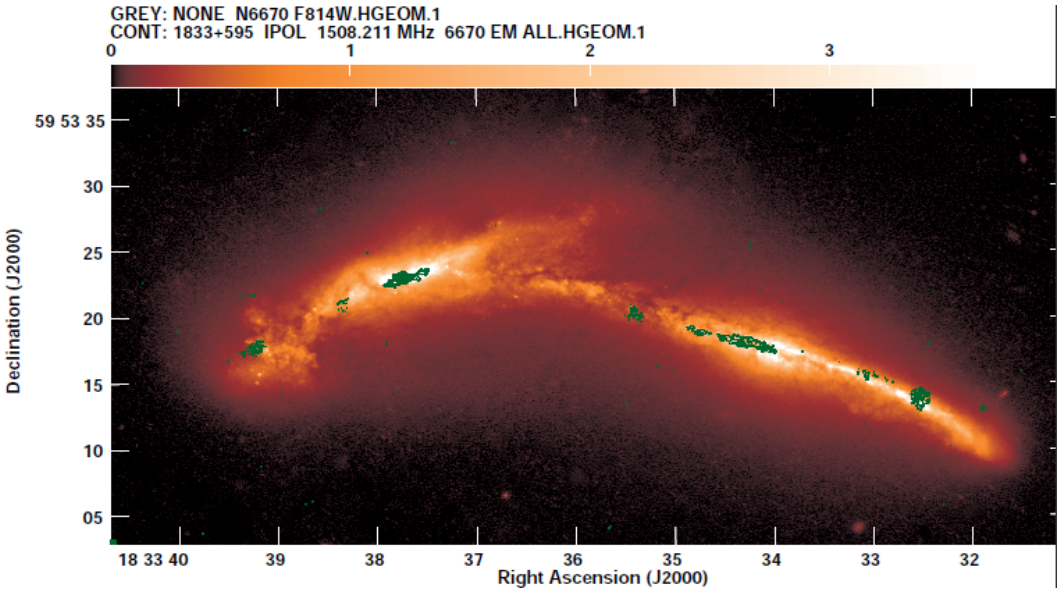

FIGURE 4.8: Optical image (HST) in background of the whole interacting system NGC6670. Contours represent the L-band observations with eMERLIN (*Private communication*).

In Fig.4.9, I present an eMERLIN image of the NGC 6670W disk at L-band where the nuclear diffuse emission and some knots within it are shown. Around 50% of the radio continuum flux comes from the inner 4 Kpc. However, when observing this galaxy with the highest angular resolution provided by the EVN at C-band (three bottom images, corresponding to those regions marked with red boxes in the eMERLIN image), the emission is completely resolved out, with no evidence of any compact source, suggesting that the bulk of the eMERLIN emission is associated with star formation. These EVN observations correspond to an ongoing parallel program to observe the LIRGI sources with the EVN. As mentioned, this EVN program is still pending data reduction and analysis and is not part of this PhD, but I wanted to show these three images since they provide a good example of the final goals to be obtained with this global project. The sensitivity limit of these EVN observations (3σ) is $\sim 30 \mu Jy/beam$, which corresponds to a luminosity of $L[erg\ s^{-1}\ Hz^{-1}] \sim 6 \times 10^{26}$. There could be supernova

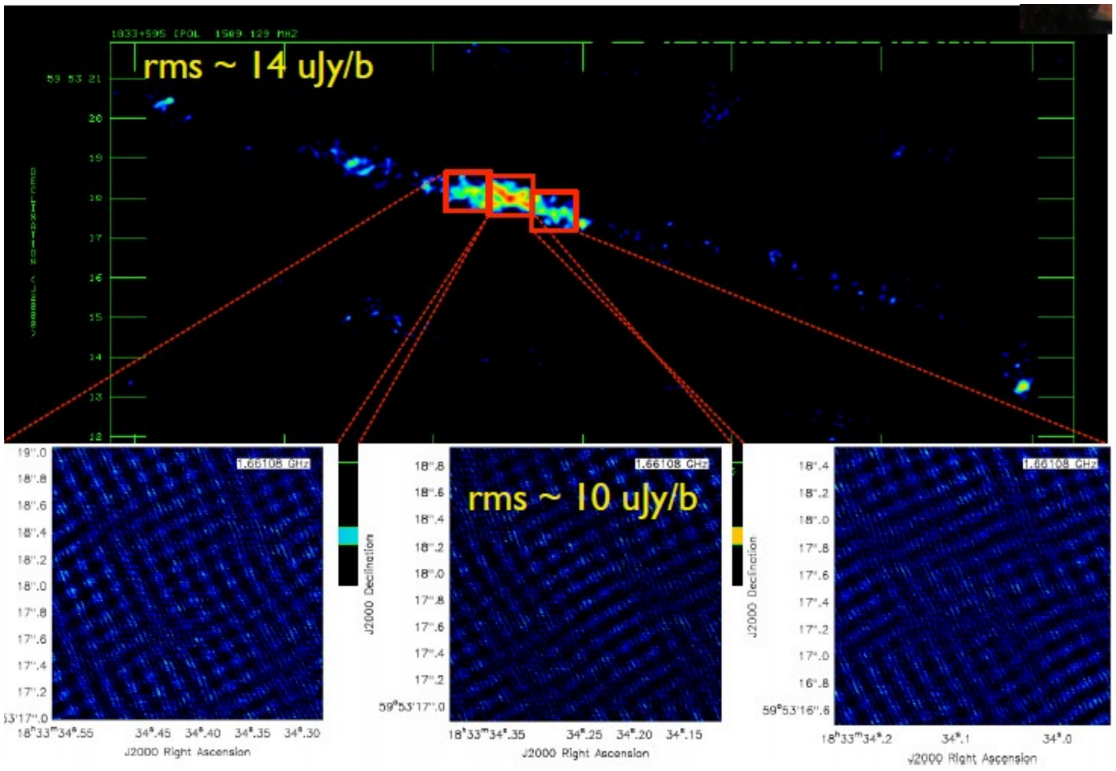

FIGURE 4.9: *Top figure*: eMERLIN at 1.4 GHz image of the East galaxy belonging to NGC6670. *Bottom figure*: EVN observations at 1.4 GHz of the different regions marked with red boxes in the image above. Note that, even when theses images are noisy, there is no hint of sources in the field.

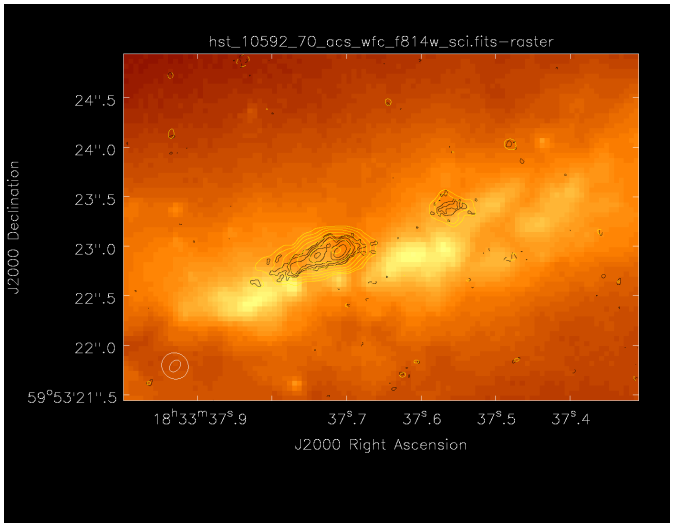

FIGURE 4.10: HST optical image at background and C-band eMERLIN in contours of NGC6670 East (left). Black contours correspond to the mid-resolution and yellow ones to the lower resolution.

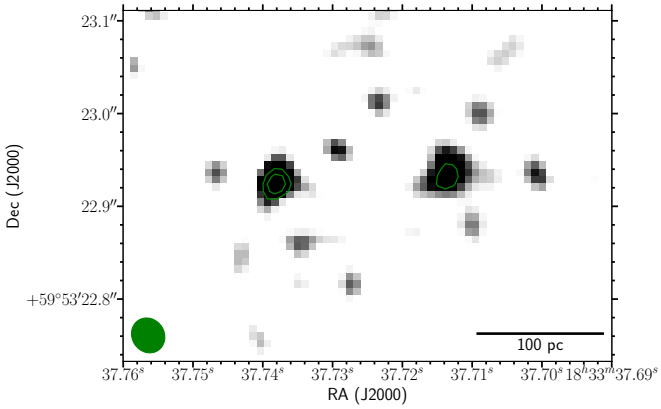

FIGURE 4.11: NGC6670 East at background and green contours ([5,6]×rms, see Table4.3)

remnants with smaller luminosities, that wouldn't have been detected by our observations, but any low-luminosity AGN should have been detected favouring the interpretation that the emission detected with eMERLIN is mostly related with starburst processes.

The eMERLIN image at C-band of the East component of the galaxy system is shown in Fig.4.10 and zoomed in contours and background in Fig.4.11. On the other hand, Fig.4.9 represents the observations at L-band of NGC 6670 West (top frame) and different regions within observed with the high-angular resolution EVN (bottom frames), both images at L-band. In the NGC 6670E nucleus, considering only the signal above 5σ, we detect two emitting regions separated by approximately $\sim$150 pc away, associated with star formation processes.

4.3.4 CGCG448: the nature of the D companion

CGCG448-020, also known as IIZw096, is a Class III interacting galaxy (Arribas et al., 2004) of, at least, two galaxies. It presents an extra-nuclear OH starburst megamaser (Baan, 1989; Baan, Salzer, and LeWinter, 1998; Baan and Klöckner, 2006; Migenes et al., 2011), whose far-IR emission dominates the total far-IR of the whole CGCG448 system ($\sim$80% of the total far-IR emission, Inami et al. 2010). It is one of the most powerful starbursts known until now (120 $M_{\odot}yr^{-1}$Inami et al. 2010) (between the values of SFR for Arp299 and Arp220).

In the region of the observation (see Fig.4.12, zoomed area corresponding to eMERLIN observations at L-band), the main features reported in the literature are the so-called C and D (20:57:24.47,+17.07.39.9 and 20:57:24.34,+17.07.39.1, respectively Goldader et al., 1997), which were firstly traced by R-band. Looking to the C-band eMERLIN

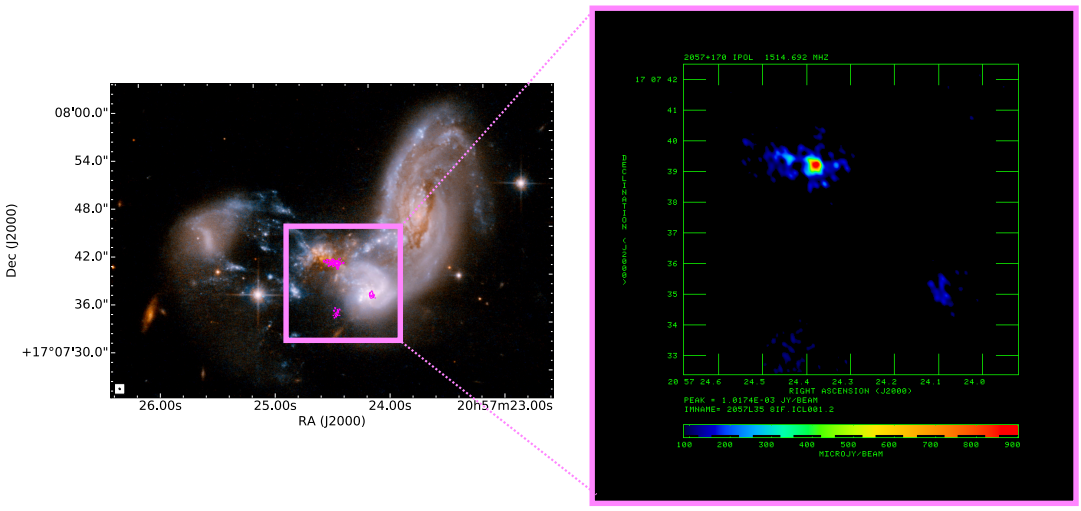

FIGURE 4.12: Images of CGCG448. *Left:* HST image at background, with eMERLIN L-band in red contours. *Right:* L-band image made with eMERLIN of the off-source region (*Private communication*).

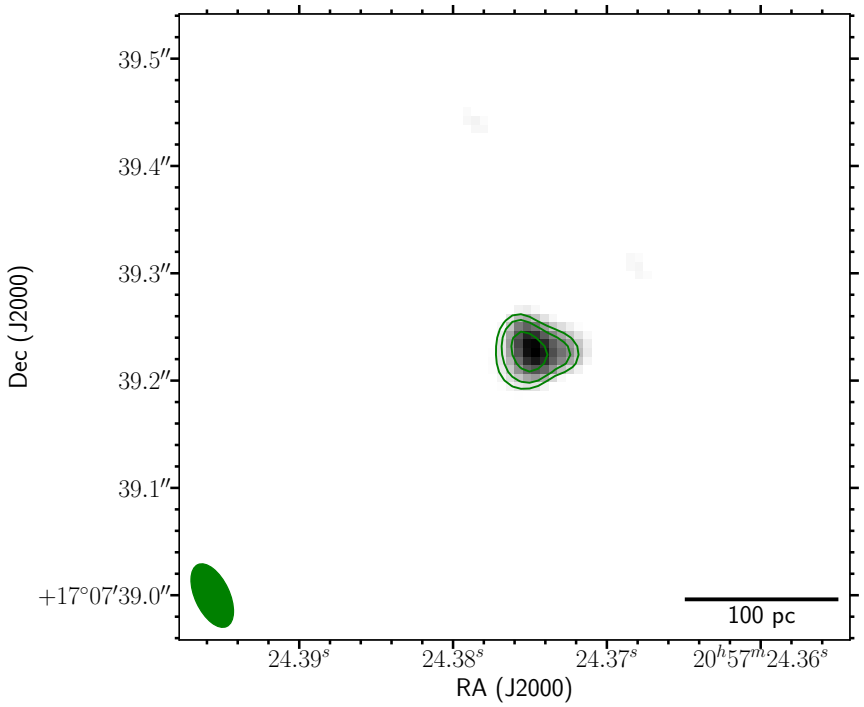

FIGURE 4.13: CGCG448 in background and green contours ([5,6,8]×rms, see Table 4.3) observed by eMERLIN at C-band. Beam shape is represented in green at left corner.

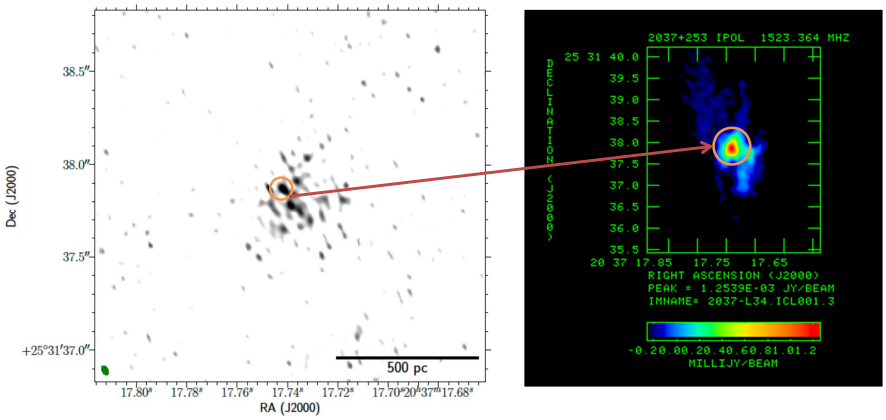

FIGURE 4.14: *Left:* IRAS20351 observed at C-band with EMERLIN. *Right:* IRAS20351 observed at L-band with eMERLIN (*Private communication*). Note that the brightest source detected at C band correspond in location to the L-band brightest source (indicated with two circles related with an arrow).

image (Fig. 4.13), the emission comes from a compact source with some extended emission toward West. This source is located at NE of the R-band D source. The integratd luminosity in the enclosed area shaped by the detected compact component is $L_\nu \geq 10^{28} erg\ s^{-1} Hz^{-1}$, which is a high value for a SNR, although not completely out of the question. The AGN is also a feasible scenario for this luminosity. Future observations with L-band will aid to discern, through the spectral index the nature of this object.

4.3.5 IRAS20351+2521: the nuclear extended emission

IRAS20351+2521 is a LIRG with $\log(L_{IR}/L_\odot)$=11.61. Its optical appearance is that of a spiral galaxy with no companions and is in the end of its merger stage, with numerous blue star knots. The eMERLIN observations at C-band (see Fig.4.14) reveals weak, diffuse emission with some central brighter knots, which is confirmed in by our preliminary L-band imaging of this source. To be conservative, in that case I do not use a gaussian fit, because the total emission clearly do not belong to a single source, and it would be very spurious to deal with the brightest points as completely separate sources. Then, I use an elliptical region in CASA viewer (center at 20:37:17.7378, +25.31.37.7523) that enclose all the extended emission to measure the corresponding integrated flux enclosed in that region. The location and the size of the elliptical region is addressed in Table 4.3.

4.3.6 Arp 220: Evidence of differential absorption in their nuclei

Arp 220 is the closest ULIRG (∼77 Mpc) and consist of two galaxies at a late stage of merger. Due to its proximity, it has been largely studied across the whole electromagnetic spectrum. However, this is the first time this source is observed at C-band with the sensitivity and resolution of eMERLIN (see beam size and rms in Table 4.3). It is known that both nuclei host two AGNs and ongoing star formation (see e.g. Barcos-Muñoz et al., 2015) in these nuclei. The observations presented in this chapter (see Fig.4.15, green contours) clearly detect the two nuclei, East and West, with a extended structure. Arp 220-West is brighter than Arp 220-East, as is also the case with the observations of LOFAR at 150 MHz.

Varenius et al. (2016) found a shift in the Eastern nucleus of Arp220 between the local peaks at 1.4 GHz (eMERLIN + VLA) and at 150 MHz with LOFAR. This shift has been also detected at 5 GHz with our eMERLIN observations (see Fig.4.15) and with the same value (∼300 mas). For the Western nucleus, an offset is also reported between local maximum, but in this case, due to its low value (∼40 mas), Varenius et al. (2016) didn't report it as intrinsic since it was comparable to the the astrometric uncertainty. However, I also find an offset of 80 mas in the same direction (see Fig.4.15) as the 40 mas offset reported by Varenius et al. (2016). If the existence of the shift was due to some systematic, frequency-independent shift, this should remain the same quantity between frequencies. However, although for the Eastern nucleus the shift is the same (∼300 mas), the shift in the Western nucleus, although in the same direction, is larger (∼80 mas). Then, it implies that it is larger between LOFAR and eMERLIN C-band than between LOFAR and JVLA L-band. This behaviour is perfectly explained by free-free absorption in a dense ionised medium (as it is the case, see e.g. Norris (1985)), since the lower the frequency, the greater the absorption, and thus the L-band peak should be closer to the LOFAR peak than the C-band peak, as it is observed in Fig. 4.15.

4.3.7 Arp 299: The first radio supernova in Arp 299A discovered by e-MERLIN

Specially relevant is the case of Arp 299 observed with eMERLIN. Fig. 4.16 (right) shows in background the extended emission detected by eMERLIN of the A nucleus. This extended emission also present some structure inside it. It presents two bright knots (named as Arp 299-AE and Arp 299-AW in Table 4.3). As it is known, this nucleus present a particularly high SFR ($\sim 100 M_{\odot} yr^{-1}$) and several tens of SNRs have been observed in the past with the EVN (Pérez-Torres et al., 2009a; Bondi et al., 2012). Comparing the location of these sources (star markers in Fig. 4.16, right) with the eMERLIN

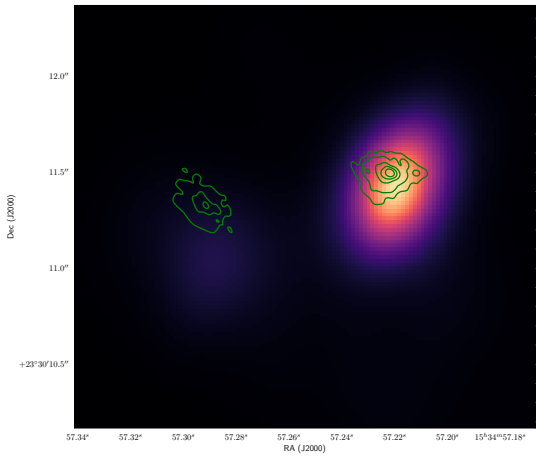

FIGURE 4.15: Background coloured image corresponds to LOFAR at 150 MHz observation (Varenius et al., 2016). Overlapped in contours the eMERLIN at 5.0 GHz image. Note that peaks of emission from both nuclei appear shifted between both images.

observations, one can relate some structures of the extended emission with the location of some EVN sources. Such is the case e.g., of A4,A6,A10,A11,A12 or the AGN+jet A0+A1. Highlighting the good correspondence in the positions between eMERLIN and EVN for all these identified sources, the presence of the brightest emission peak seems not to correspond with any previous detected source. Being that true, I report the discovery of a new radio source in the nucleus of Arp 299-A. The associated luminosity to the integrated flux reported in Table 4.3 is $L = 6.4 \times 10^{28} erg\ s^{-1} Hz^{-1}$. Comparing this value with other typical luminosity values (see e.g. all the SNRs Chomiuk and Wilcots (2009)), one notes that it should be one of the brightest SNRs. For a deeper study, I will propose follow-up observations with eMERLIN at least at C and L-band, as well as sharper observations with the EVN at those frequencies to determine its flux, position and size. This will allow our group to trace the SN light-curve and identify the type of the SN.

4.4 Summary and outlook

I have presented here continuum C-band e-MERLIN observations of seven U/LIRGs. Our observations reveal emission from structures midway between those traced by the VLA and EVN scales. The e-MERLIN LIRGI observations, even if only at C-band and for seven sources, highlight the potential of e-MERLIN to unveil the main dust-heating mechanism in the nuclear regions of local LIRGs. Namely, e-MERLIN's ability to detect both compact objects, as well as diffuse, extended emission around those (compact) objects, in some cases pinpointing the existence of AGN and/or young supernovae and

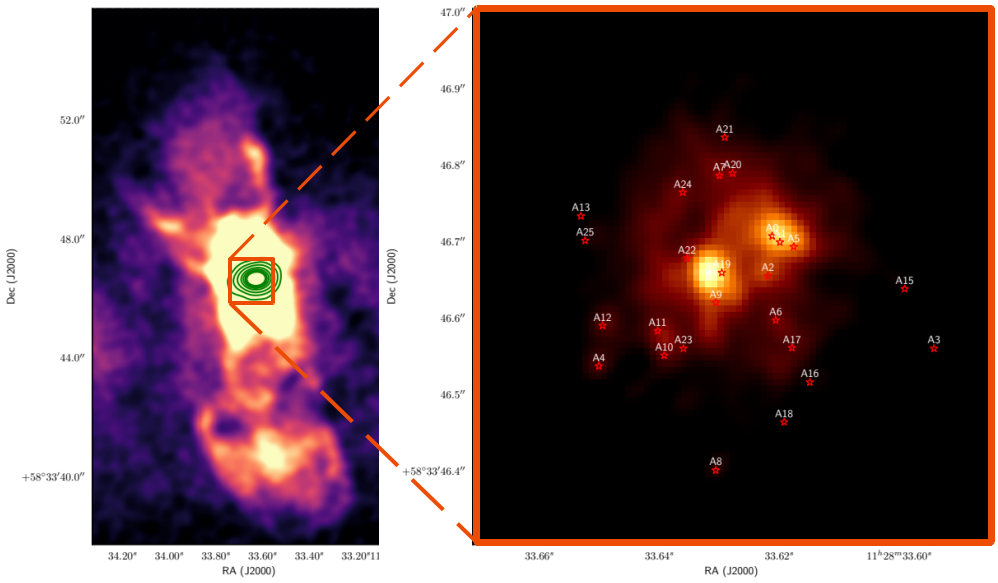

FIGURE 4.16: *Left*: Background image of Arp 299-A and its outflow at 150 MHz with LOFAR and green contours at 8.4 GHz with JVLA (Ramírez-Olivencia et al., 2018). *Right*: Zoom in the A-nucleus. Background image corresponds to eMERLIN observations at 5.0 GHz(C-band); star markers pinpoint the position of the SNRs found in (Pérez-Torres et al., 2009a).

supernova remnants, as demonstrated in the case of Arp 299-A, where we have directly detected a new radio supernova. This is something that is beyond the reach of the JVLA because of its poorer angular resolution, and so far only achieved with VLBI arrays. Similarly, e-MERLIN has demonstrated the existence of a starburst regions with no evidence of AGN (NGC6670-West), or the existence of a strong candidate for the AGN and its associated jet at the nuclear region (NGC 7469). In the case of advanced mergers, such as Arp 220, e-MERLIN resolves the nuclei of both merging galaxies. On the other hand, Mrk273 present extended emission in its North component, pointing out to a starburst region, and the luminosity from its SE compact component is compatible with an AGN scenario with no evident extended emission at these scales. However, SW source, typical in the literature, is no detected in our e-MERLIN observations, suggesting a very strong free-free absorption in case the presence of an AGN in case it exists. Finally, in the case of the most advanced merger, IRAS 20351, e-MERLIN detects one single nucleus, as expected for a source where both AGNs have already merged.

In the near future, once the data for the LIRGI sample are reduced for all sources, we will obtain a robust, statistically relevant inventory of local LIRGs, which should allow us to extrapolate general results to more distant U/LIRGs. The addition of continuum L-band observations, possibly complemented by the currently ongoing observations with LOFAR, will allow us to characterise the insterstellar medium in the nuclear regions of those galaxies, thus estimating such relevant physical parameters as the properties as the density and the magnetic field. Besides a general understanding of the nuclear phenomenon, we will also monitor, or observe in more detail, likely including VLBI observations, some of the most interesting cases, e.g., the new SNR discovered in Arp299, or the AGN jets in NGC 7469 or CGCG 448. In this sense, we note that we have been working also on high-resolution, high-sensitivity EVN observations at C and L-band, which are currently in their last steps of calibration, and hence close to being available for science (as the example shown for NGC6670). When all those data are published, the legacy value of LIRGI will become obvious, as we will be tracing in unprecedented detail the radio emission of local LIRGs at the relevant frequencies of 1.4 and 5.0 GHz, where synchrotron radio emission is dominates, and with angular resolutions ranging from about 1.5 (~ 0.5) arcsecond (JVLA in A configuration at L- and C-band, respectively) to the 0.15 (~ 0.05) arcsecond resolution provided by e-MERLIN at those frequencies, and ending with the $\sim$15 (~ 5) millarcsecond angular resolution provided by the EVN. The superb combination of sensitivity and resolution will allow us to characterize the diffuse extended emission of those merging systems both globally and locally, in their innermost regions, as well as to isolate the compact sources where AGNs, SNe, and SNRs hide.

5 Universal Supernova Remnant Luminosity Function

CORE-COLLAPSE supernovae (CCSNe) are a well-known and robust tracer of recent (≤ 40 Myr) massive star-formation. They have been used to determine star-formation rates (SFR) in, e.g., local LIRGs and ULIRGs, where the bulk of their infrared emission is due to recent bursts of star formation, implying CCSN rates as high as $\sim$(0.8-2.0) SN/yr e.g., Arp 299A (Pérez-Torres et al., 2009a; Bondi et al., 2012) and Arp 220 (Batejat et al., 2010; Varenius et al., 2019). However, most nearby galaxies are "normal", in the sense that they lack a massive burst of star formation and, even for large spiral galaxies, the current production of massive stars, and therefore of SNe, is orders of magnitude lower than for U/LIRGs (for example, the Milky Way with $\sim$0.02 yr^{-1} van den Bergh, McClure, and Evans 1987). Therefore, the use of CCSNe to determine SFRs in normal, local galaxies is not very promising.

Extragalactic supernova remnants (SNRs) offer an alternative and more promising approach for the determination of SFRs in local galaxies than CCSNe. Indeed, all CCSNe evolve into SNRs, whose observable phase has a timescale much larger than their young SN phase, which may allow to detect a significantly larger number of SNRs. Furthermore, the radio emission from SNRs is not hampered by dust, which potentially allows to uncover all the SNR population in a given galaxy, (e.g., in the Milky Way; see Brogan et al. 2006).

The radio emission from young CCSNe has a synchrotron origin, and is governed by the interaction between the SN-ejecta and the circumstellar medium (Chevalier, 1982). The synchrotron radio emission is thought to arise either in the forward shock ($v_{\rm sh} \gtrsim 10000$ km s^{-1}), which would be responsible for the continuous acceleration of relativistic electrons, and/or close to the surface discontinuity, where turbulent eddies would amplify the magnetic fields needed to sustain the synchrotron radio emission

(Chevalier, 1982). In this scenario, the SNR phase starts when the pressure of the interstellar medium, $P_{\rm ISM}$, is approximately equal to the ram pressure of the pre-supernova circumstellar wind (e.g., Chevalier and Fransson 2001, Pérez-Torres et al. 2002)

The young stage of a SNR comprises the free-expansion and the early Sedov phases, in which the particle acceleration is very efficient (Berezhko and Völk, 2004), and the bulk of radio emission continues to be of synchrotron origin, as in the CCSN phase. The typical time for a supernova to enter its SNR phase is in the range $100-1000$ yr in normal galaxies (Berezhko and Völk, 2004), and these values are expected to be even shorter for SNe exploding in very dusty, high-density environments like those encountered in compact starburst regions, since $P_{\rm ISM}$ will be much higher. The implication is that the young SN phase is just a tiny fraction of the radio (synchrotron) lifetime of a SNR, which is in average around 60000 yr (Frail, Goss, and Whiteoak, 1994). Therefore, in any given galaxy one expects to find very few SNRs in their young radio supernova phase, i.e., interacting with the **C**ircum**S**tellar **Medium** (**CSM**) rather than with the ISM. At the end of its life, once the SNR has entered its radiative phase, particle acceleration becomes quite inefficient, the synchrotron radio emission fades away very quickly, and the overall radio emission may be even dominated by thermal free-free emission.

The determination of the **L**uminosity **F**unction (**LF**) permits to gain significant insight into the relevant physical processes by directly relating the most direct observable, the SNR luminosity, with the intrinsic physical properties of the sources under study. In addition, if a LF could be shown to be "universal", then it would become an extremely powerful tool, as this allows to physically characterise the overall source population. In the case of SNRs, the determination of its radio LF is of particular importance, since the luminosity in radio SNRs is related to several properties of both the whole galaxy and the local characteristics of the surrounding SNR medium. For example, the observed radio synchrotron flux depends on the magnetic field according to the expression $\mathrm{S}_\nu \propto \mathrm{B}^{(\mathrm{p}+1)/2}$ (e.g., Pacholczyk 1970), where p is the spectral index for the injected particles distribution. Also, several works (i.e. Hunt and Reynolds, 2006 or Thompson, Quataert, and Murray, 2009), have shown the existence of a close connection between the observed luminosity at radio wavelengths and the local and overall ISM density of the host galaxy.

The present chapter builds upon the work of Chomiuk and Wilcots (2009), (hereafter CW09), who investigated the possible existence of a universal (radio) LF of SNRs using a sample of nearby galaxies hosting SNRs (see section 5.1.1 for further details), excluding the ULIRG Arp220, which will be introduced further together with the LIRG Arp299. Here, I revisit the topic of the possible existence (and its validity) of a radio LF for SNRs, following a different statistical approach, which yields more robust and

confident results. For comparison purposes, I use the same sample as used in CW09 (sect. 5.1.1). Then I describe the method to obtain the radio LF of SNRs (sect. 5.1.2), and add the SNRs from the LIRG Arp 299-A (see Chapter 2 for details on this galaxy). Finally, I discuss the physical implications of the existence of a universal radio LF and its basic parameters in normal galaxies.

I calculated the mass density of the surrounding ISM (ρ_{ISM}) of Arp299-A as follows. First, I used the relation between the surface gas density (Σ_g) and the star formation surface density (Σ_{SFR}) from Kennicutt et al. (2008):

$$\Sigma_g[M_\odot pc^{-2}] = 361\Sigma_{SFR}^{0.71}[M_\odot yr^{-1}kpc^{-2}] \tag{5.1}$$

For the star formation in the A nucleus, I used SFR=90$M_\odot yr^{-1}$ from Mattila et al. (2012). From Bondi et al. (2012), I assume a 150 pc size of the region where the star formation takes place. I then used a constant scale height of 100 pc, as in Chomiuk and Wilcots (2009). In this way, Σ_{SFR}=4$\times10^3 M_\odot yr^{-1}kpc^{-2}$ and the estimated ρ_{ISM}=1300$M_\odot pc^{-3}$ (see Tab.5.1).

5.1 The radio luminosity function of supernova remnants

5.1.1 Galaxy sample

The galaxy sample used in our analysis comprises the SNR data for 18 nearby ($D \leq 8$ Mpc) normal galaxies (Arp220 and Arp299 not included). All those galaxies are taken from CW09. Table 5.1 summarises the relevant information for all of them. The process of collecting the SFR values is described in CW09, who use a combination of Hα and 25 μm fluxes as Calzetti et al., 2007. The Hα flux was taken from Kennicutt et al., 2008 and the 25 μm fluxes from Sanders et al. (2003), Rice et al. (1988), Lisenfeld et al., 2007 and Moshir, Kopman, and Conrow, 1992. CW09 consider an object to be a SNR if it fulfills the following criteria: (i) A flux density value, $S_{1.4GHz} \geq 3\sigma$, where σ is the image rms noise figure, at the reference frequency of 1.4 GHz, (ii) a non-thermal spectral index ($\alpha \leq -0.2$; $S_\nu \propto \nu^\alpha$, and (iii) a counterpart detection at Hα. I refer the reader to CW09 for further details.

Galaxy	Type	Distance Mpc	SFR $M_\odot$ yr^{-1}	ρ_{ISM} $M_\odot pc^{-3}$
LMC	SB(s)m	0.05	0.21	0.03
SMC	SB(s)m spec	0.06	0.03	0.007
IC10	lBm	0.66	0.02	0.1
M33	SA(s)cd	0.84	0.24	0.02
NGC 1569	lBm	1.9	0.28	0.2
NGC 300	SA(s)d	2.00	0.10	0.02
NGC 4214	lAB(s)m	2.92	0.17	0.1
NGC 2366	lB(s)m	3.19	0.08	0.008
M82	I0	3.53	10.4	2
M81	SA(s)ab	3.63	0.48	0.01
NGC 7793	SAB(s)d	3.91	0.26	0.02
NGC 253	SAB(s)c	3.94	6.18	0.2
NGC 4449	IBm	4.21	0.47	0.03
M83	SAB(s)c	4.47	3.00	0.1
NG 4736	(R)SA(r)ab	4.66	0.46	0.2
NGC 6949	SAB(rs)cd	5.9	3.23	0.09
NGC 4258	SAB(s)bc	7.98	1.28	0.01
M51	SAbc	8.00	2.45	0.04
Arp220	ULIRG	77.0	127	100
Arp299-A	LIRG	44.0*	90**	1300***

TABLE 5.2: *Distance from (Heckman et al., 1999).** SFR from Mattila et al. (2012) ***Mass density derived for Arp299 in the same way that (Chomiuk and Wilcots, 2009) (see Sect. 5.1.1 for further details).

5.1.2 Building up the radio luminosity function of supernova remnants

Assuming that the differential LF of the SNRs in each galaxy can be fitted to a power-law

$$n(L_{1.4}) = \frac{dN}{dL_{1.4}} = AL^{\beta} \tag{5.2}$$

where $\mathrm{n(L_{1.4})}$ is the number of SNRs, dN, in the 1.4 GHz luminosity interval, $\mathrm{dL_{1.4}}$; A is a scaling factor and β is the power-law index.

The SNRs luminosities at 1.4 GHz are calculated as $\mathrm{L_{1.4} = 1.20 \cdot S_{1.4}\, D^2}$, where $\mathrm{L_{1.4}}$ is the 1.4 GHz SNR luminosity in units of $10^{24}\mathrm{ergs^{-1}Hz^{-1}}$, D is the galaxy distance in Mpc, and $\mathrm{S_{1.4}}$ is the 1.4 GHz flux density of a SNR in mJy (D is taken from table 5.1, and $\mathrm{S_{1.4}}$ is taken from the source tables 3-21 from CW09).

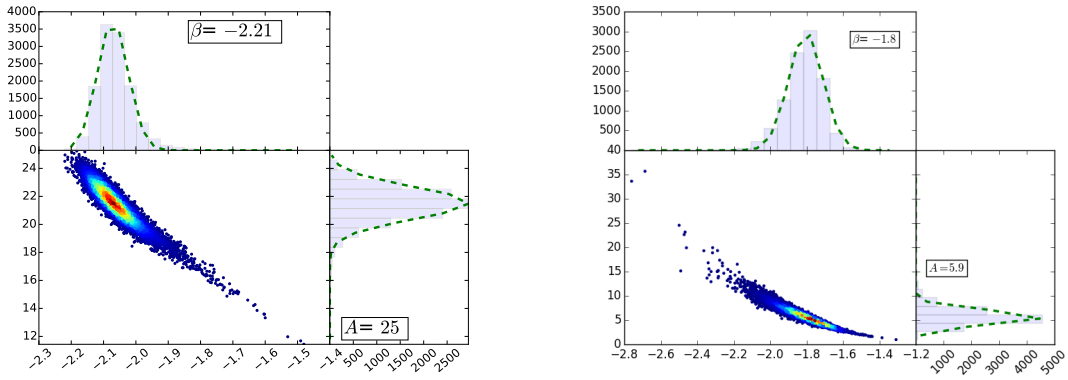

FIGURE 5.1: Left: Results from the Monte Carlo method (see main text) applied to the SNRs in M 33. The upper and right panels represent the distribution of A and β, respectively, while the central panel is the combination of both. The colour scale indicates density points, with warmer (colder) colours representing higher (lower) density values. The A and β values inside the captions correspond to the median. Y-axis in upper and right gaussian fits are the number of iteration (of a total of 10000). Right: the same than left, but in this case with NGC2366, which the dealing of a gaussian distribution for A is not completely justified. This is the general behaviour for the rest of the galaxies.

Since the number of SNRs in each galaxy is in general rather small, a cumulative LF is better suited than a differential LF, which almost inevitably would have dips. In fact, a cumulative LF prevents the presence of dips in the LF (see, e.g., Rodríguez-González et al., 2015), unlike a differential LF. Those dips usually can be confused with sample incompleteness in the resulting fits of A and β, and do not add any real physical information, beyond the fact that there is a lack of objects. Further, the cumulative LF

is handled in a logarithmic form, which simplifies the data analysis:

$$\begin{aligned} \log N_i &= \log\left[\frac{A}{\beta+1}\left(L_i - \Delta L/2\right)^{\beta+1}\right] \\ &= \log\left(\frac{A}{\beta+1}\right) + (\beta+1)\log L \end{aligned} \tag{5.3}$$

where $L = L_i - \Delta L/2$. One of the novel aspects of the treatment of the LF in this work is the use of non-uniform size binning. It is well known that, for uniformly-size bins, the smaller the source sample, the larger the bias (Maíz Apellániz and Úbeda, 2005). I therefore sampled the LF using a non-uniform size binning to prevent the above bias. To adequately track the growth of the cumulative LF, I chose the bin size for each individual galaxy in such a way that each bin increased the total SNR number just by one. I then determined A and β via a Monte Carlo method. Namely, for each galaxy I introduced random luminosity values according to a Gaussian distribution centered at the luminosity obtained from the flux densities listed in Table 1 from CW09, and with a variance equal to the 1-σ luminosity uncertainty, and repeated this process 10000 times. In general, the resulting distributions are well fit by a Gaussian distribution, although there are a few cases where the distribution departed from Gaussianity (Fig. 5.1). For this reason, here I use as statistic the median value for each parameter, and the 95.4-percentile (associated with a 2σ of a Gaussian distribution) as the uncertainty. As an example of the approach, I show in Figure 5.1 the results of applying the Monte Carlo method to the SNRs in M33. The upper and right panels represent the distribution of the β and A parameters, respectively. In this example, the distribution can be well fitted by a Gaussian (green dashed line over the distribution of A and β, upper and right figures in Fig. 5.1. However, as discussed above, the value indicated in the legend of the figure is the median of the distribution.

5.2 Results and discussion

5.2.1 The radio luminosity function of SNRs as a universal tool.

I have revisited the existence of a universal radio luminosity function (RLF) of SNRs by stacking all 347 SNRs (excluding Arp299 to follow the same procedure as CW09 and compare in the same conditions the results) into a single cumulative histogram of luminosities, as if all of them belonged to a single, "universal" galaxy. This "stacking" approach has two main advantages over a "galaxy-by-galaxy" approach: First, the results are more robust than those obtained by fitting separate power-laws to the SNRs

in individual galaxies and then deriving average (or median) values for A and β; second, this allows to have a statistically large sample so as to study in detail differences that may arise from intrinsic physical properties which are difficult to tackle with small samples.

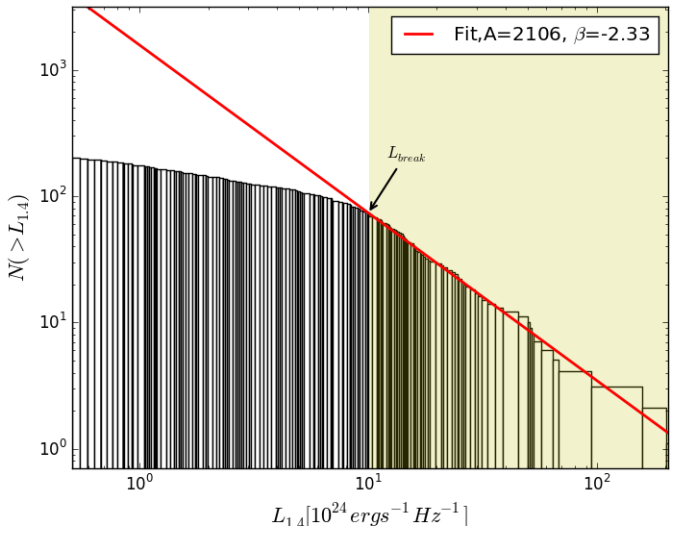

FIGURE 5.2: Cumulative histogram of all (205) SNRs included in the final sample (considered to be complete after having removed the SNRs that are below the true completeness limit of each galaxy; see main text). The red fit corresponds to a single power-law as in Eq. 5.3. It represents the fit considering just the SNRs above L_{break}. The yellow shadowed area indicates the luminosity range taken into account to determine the universal β value.

The initial cumulative histogram, adding up the SNRs of all galaxies, consisted of 347 SNRs. I then followed CW09 to deal with the true completeness limit, i.e., the luminosity value above which the SNR sample of a given galaxy can be reliably considered as complete. In practice, this is determined by the 3-σ upper limit in luminosity for each galaxy, due to the limited sensitivity of the observations. This reduced the total number of SNRs available for our analysis to 237. The best-fit parameters that characterise the RLF for this sample are $A = 137^{+4}_{-4}$ and $\beta = -1.53^{+0.01}_{-0.01}$. However, this "universal" RLF with a single power-law index fails to fit the luminosities of SNRs, specially at low luminosities. Therefore, the power-law index $\beta \approx -1.5$ does not seem to properly represent the number of SNRs per luminosity range.

The reason for this change of slope at low luminosities lies most likely in the fact that the data included in the cumulative histogram takes into account only the completeness limit of each individual galaxy. Therefore, low-luminosity SNRs can only be detected in nearby galaxies. There is thus a transition from an incomplete (at low luminosities) to a

complete sample (at high luminosities), which implies a change, a "break", in the slope of the luminosity function. This "break" value corresponds to the "true" completeness limit of the (stacked) sample of SNRs.

Despite the stacked sample is large, uniform binning is not the best approach. First uniform binning produces a bias, as mentioned earlier. Second, it does not allow to adequately probe some regions of the luminosity function that are poorly sample. For this reason, we applied non-uniform binning, which allowed us to robustly identify this "break" value, $L_{\rm break}$, where the RLF changes its slope, and indicating that below this value the sample is incomplete. Therefore, we fitted the data to a two-slope power-law, which yielded the luminosity break, i.e., the "true" completeness limit, and the "true" power-law index of the LF. The best-fit parameter values were $\mathrm{L_{break}} = (10.1 \pm 0.4) \times 10^{24}\mathrm{erg^{-1}Hz^{-1}}$, $\mathrm{A} = 641^{+53}_{-67}$ and $\beta = -1.83 \pm 0.02$. I emphasize here that the use of SNRs with luminosities $L < L_{\rm break}$ could lead to wrong, or at least unreliable values of the power-law index of the LF.

At high luminosities, there is still a mismatch between the fitted slope and the data, which is caused by the remnants of the starbursting galaxies M82 and NGC 253, where current star formation is much enhanced. This results in a significantly higher number of bright SNRs, in comparison with the rest of the other, normal galaxies in the sample. Therefore, I excluded the starburst galaxies M82 and NGC 253 from the final sample and fitted the final dataset, which included 205 SNRs, to a two-slope power-law to determine the luminosity break, its corresponding value of A, and the "true" power-law index of the LF. The best-fit parameter values are $\mathrm{L_{break}} = (6.9 \pm 0.4) \times 10^{24}$, $\mathrm{A} = 2106^{+346}_{-426}$ and $\beta = -2.33 \pm 0.04$ (Fig. 5.2). Therefore, in view of the exercise of excluding some kind of galaxies and individual SNRs done before, I can conclude that the universality of the luminosity function exists provided that all the galaxies considered are normal galaxies (i.e., non-starbursting) and it is ensured the true completeness limit in the whole stacked sample (taking into account that the considered SNRs have the same possibility of being observed at any of the distances considered).

5.2.2 Starburst galaxies and the SNR distribution in their host galaxies

As I mentioned above, a flatter power-law index is obtained when starbursts (M82 and NGC 253) are included, due to the much more likely detection of very bright radio SNRs in starbursts compared to normal galaxies. This naturally results in a flattening of the power-law at high-luminosities with respect to normal galaxies, as I find in the data. It would be desirable to have additional data from other starburst galaxies, so as to ascertain these differences in a more robust way, which will become feasible with more sensitive radio telescope arrays.

To further understand the differences between M82 and NGC253 with respect to the other galaxies, I plotted the location of the SNRs within their host galaxies. This could unveil some true physical reason, e.g., if the luminosity of the SNRs is likely dependent on the density of the interstellar medium (ISM; I will study the relation in Eq. 5.13 and 5.17); the nuclear starbursts should show a concentration towards their central regions where the nuclear starbursts are located, while in normal galaxies one would expect that the SNRs are located along the spiral arms (in spiral galaxies; (Johnson and MacLeod, 1963), (van den Bergh, McClure, and Evans, 1987), or (van Dyk, Hamuy, and Filippenko, 1996)). Figure 5.3 shows the results for three representative normal galaxies: M33, M51, and M81. The SNRs of M51 and M81 are found in their well-defined spiral arms; in M33 the SNRs also appear to follow the spiral arms, but SNRs are actually distributed all over the galaxy. I also show in Fig. 5.3 the distribution of SNRs in the starbursts M82 and NGC 253. The image for M82, the prototypical starburst galaxy, displays only the inner ≈ 500pc, where essentially all of this star forming activity takes place. Correspondingly, all SNRs reside in the nuclear region, not in the spiral arms. The image of NGC253 also shows that all its SF activity takes place in the central kpc of the galaxy. In fact, several superstar clusters have been formed in its center (Watson et al., 1996), probably due to a merger that happened in the past (Davidge, 2010). The SNR distribution shows a clear concentration of the remnants in its center, as expected. The brightest SNRs are located in the nuclear regions ($\leq$1 kpc), where the local ISM density is expected to be higher.

I applied the same scheme above to each individual SNR sample, i.e., I used a Monte Carlo method to determine the median value of A and β for each galaxy. I show the results in Table 5.3 and two examples in Fig. 5.6. The dashed blue line corresponds to the fit to each galaxy.

I highlight that M33 is the galaxy that contributes with a larger number of SNRs (49 out of 205) to the stacked sample, which potentially could bias the results. To this end, but also to take into account any potential bias from any other galaxy, I applied a bootstrap method to determine the power-law index of the universal RLF. More specifically, I iteratively removed one galaxy at a time from the sample and run the Montecarlo code to determine A and β. The results are shown in Fig. 5.5. All values are within a 6% of the nominal value of $\beta = -2.33$, indicating that there is no single galaxy that affects significantly the final value found for the "universal" RLF.

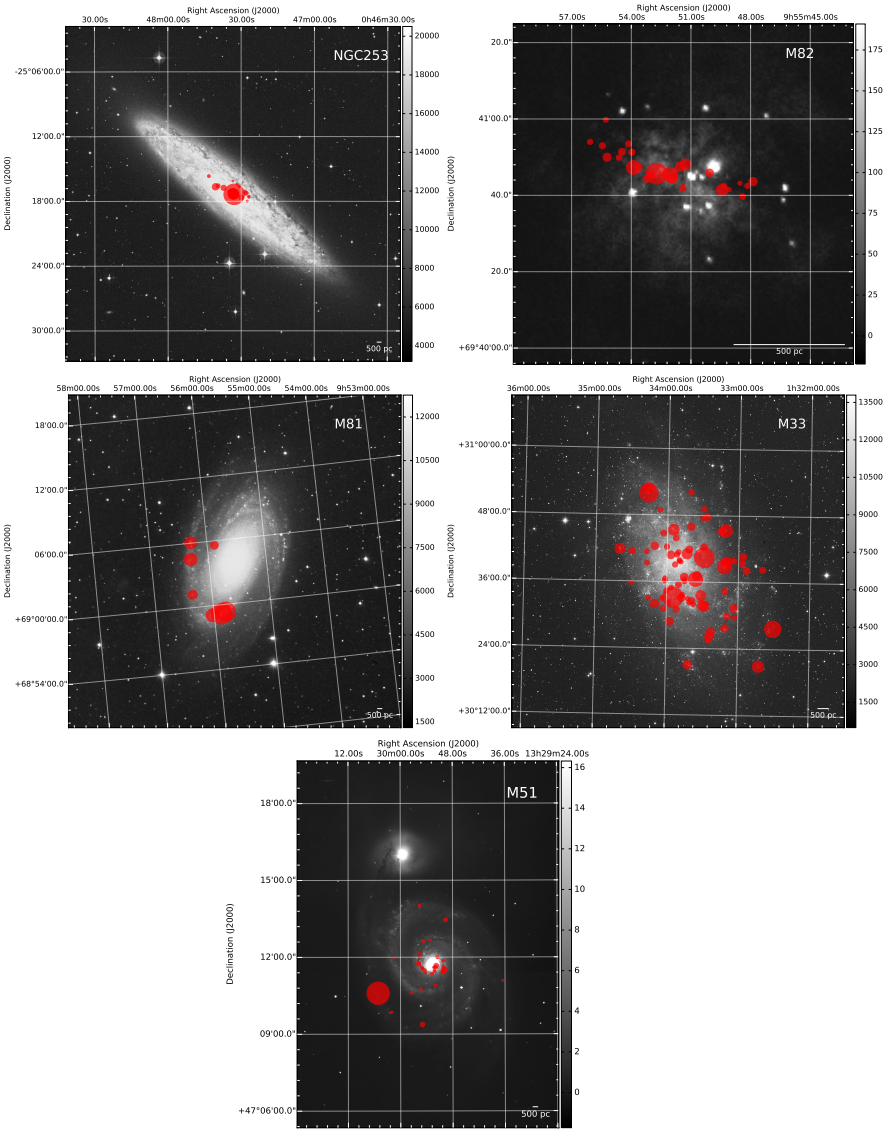

FIGURE 5.3: Location of the SNRs in five galaxies from our sample. Circles indicate the position of the respective SNRs, with circle size proportional to the SNR radio luminosity. The M82 background image is from the Chandra telescope; the M33 background image has been taken at 6450 Å (Palomar48-inchSchmidt); the M51 background image has been taken at at 8800 Å; the M81 background image has been taken at 6450Å (Palomar48-inchSchmidt); the NGC253 background image has been taken at 4680Å (UKSchmidt).

Galaxy	β	A
IC10	$-1.32^{+0.01}_{-0.01}$	$1.28^{+0.08}_{-0.08}$
LMC	$-2.16^{+0.30}_{-0.19}$	24^{+9}_{-21}
M33	$-2.21^{+0.09}_{-0.19}$	25^{+4}_{-3}
M51	$-2.49^{+0.17}_{-0.22}$	728^{+368}_{-559}
M81	$-2.21^{+0.33}_{-0.28}$	98^{+49}_{-176}
M82	$-2.02^{+0.07}_{0.12-}$	1073^{+561}_{-594}
M83	$-2.41^{+0.15}_{-0.14}$	492^{+204}_{-362}
NGC 253	$-1.87^{+0.16}_{-0.34}$	645^{+505}_{-1060}
NGC 300	$-2.47^{+0.46}_{-0.47}$	23^{+11}_{-19}
NGC 1569	$-2.11^{+0.12}_{-0.16}$	31^{+11}_{-12}
NGC 2366	$-1.82^{+0.20}_{-0.14}$	$5.9^{+2.0}_{-3.5}$
NGC 4214	$-2.22^{+0.64}_{-0.37}$	114^{+24}_{-173}
NGC 4258	$-1.96^{+0.18}_{-0.14}$	173^{+79}_{-233}
NGC 4449	$-1.43^{+0.02}_{-0.03}$	$4.7^{+0.9}_{-0.8}$
NGC 4736	$-3.30^{+0.80}_{-0.48}$	29012^{+2880}_{-39561}
NGC 6946	$-2.16^{+0.08}_{-0.10}$	338^{+117}_{-134}
NGC 7793	$-1.53^{+0.07}_{-0.09}$	$5.4^{+2.0}_{-2.5}$
SMC	$-3.05^{+0.65}_{-0.42}$	$9.7^{+2.9}_{-5.3}$
Arp 220	$-1.92^{+0.10}_{-0.13}$	13456^{+35277}_{-8759}
Arp 299	$-2.32^{+0.01}_{-0.02}$	42696^{+2135}_{-4413}

TABLE 5.3: A and β parameters for each galaxy (median value of the resulting Monte Carlo distribution), taking into account the true incompleteness limit, except for Arp220 and Arp299 (see text). The β and A individual values for Arp220 and Arp299 come from the entire sample; for the universal LF Arp299 is not considered, and Arp220 contributes with the 4 SNRs considered as the true complete sample in CW09. Uncertainties correspond to the percentile 95.

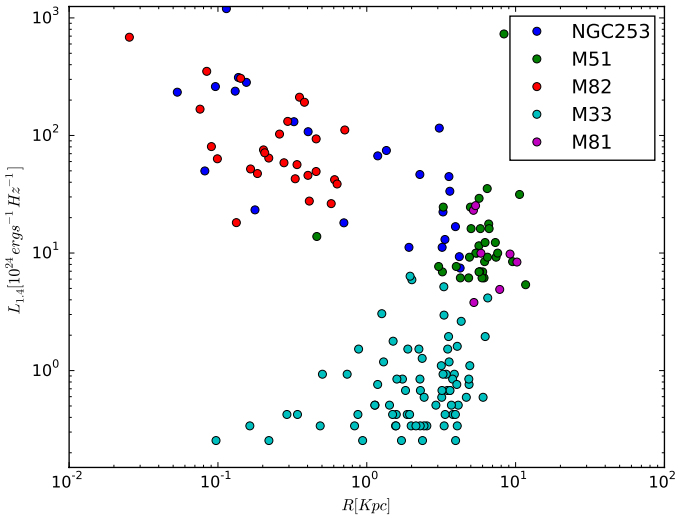

FIGURE 5.4: Comparison of the radial distribution of SNRs in NGC253, M82, M81, M33 and M51. Each point represents one SNR, and the color indicates the host galaxy (see legend).

5.2.3 Physical implications of the luminosity function

Luminosity functions always reflect intrinsic, fundamental physical properties of the objects under study. In this case, the radio luminosity function (RLF) of SNRs yields an excellent opportunity to investigate the connection between the SNRs and the different physical processes and models proposed to account for the specific properties of SNRs, and even some general properties of their host galaxies.

I showed in the previous section that a universal β radio luminosity function (RLF) for SNRs in nearby normal, i.e. non-starbursting galaxies, exists. Since the sample can be considered complete (at higher luminosities), the power-law index of the RLF is $\beta \approx -2.33$.

I also found that the inclusion of starbursting galaxies (M82 and NGC 253 in the sample) results in a significantly flatter RLF ($\beta \approx -1.8$),likely due to a larger population of bright SNRs than in normal galaxies. While the number of starburst galaxies is not large, the use of the cumulative data indicates that this trend seems to be real. It is well known that the ISM density in starburst regions is much higher–often thousand of times–than in normal galaxies. While there aren't enough starburst and/or U/LIRGs galaxies in the sample to draw any statistical confirmation, it is possible that the different slopes of the RLF for normal and starburst galaxies may be related to the huge difference in the ISM densities of normal and starbursting galaxies, which may result in an overproduction of massive stars, and hence of a larger amount of CCSNe and SNRs (see, e.g., Klessen, Spaans, and Jappsen, 2007.) The power-law index, β, is thus a

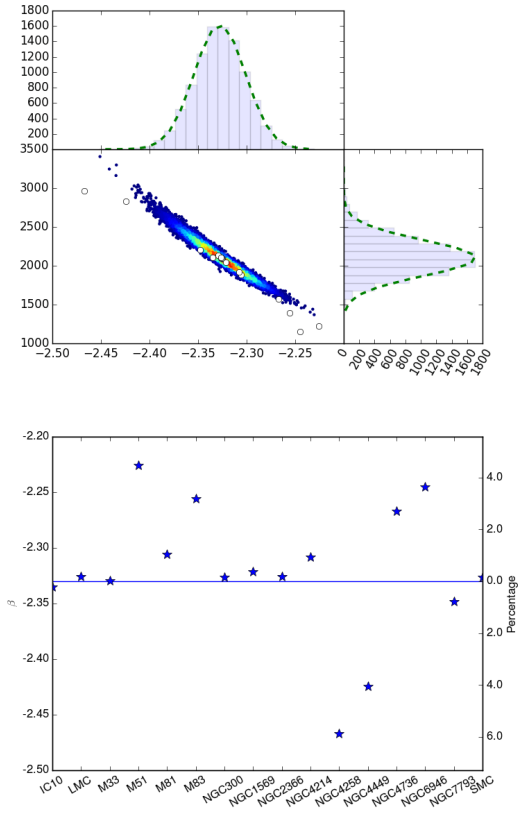

FIGURE 5.5: *Upper*: Monte Carlo distribution for the SNRs in the stacked sample. Each white dot represents the (median) value of the universal β having removed the SNRs from one of the galaxies. *Lower*: Blue stars correspond to the universal β value excluding the SNRs of the indicated galaxy (the excluded galaxy is shown in the x-axis). Blue line represents the universal value for the whole sample ($\beta_{univ} = -2.33$). The right y-axis is shown to compare the percentage of the difference between these values and the universal value.

very important parameter that characterises overall properties of the entire SNR population. The other parameter that, together with β, defines the radio luminosity function is A, and the relevant question is with which intrinsic properties of the galaxies can be related.

The value of $\beta_{univ} = -2.33$ is statistically different from the value $\beta_{CW09} = -2.07$ obtained by CW09. The results are more robust mainly due to the following reasons: (i) I used a variable size binning to build up the cumulative SNR histograms, unlike CW09, which used a fixed bin width. As discussed earlier in this paper, a variable bin size is a more appropriate approach, and it shapes better the luminosity function. (ii) I determined the overall true completeness limit from the presence of a break in the global LF (L_{break}), thanks in part to the use of non-uniform binning; CW09, on the other

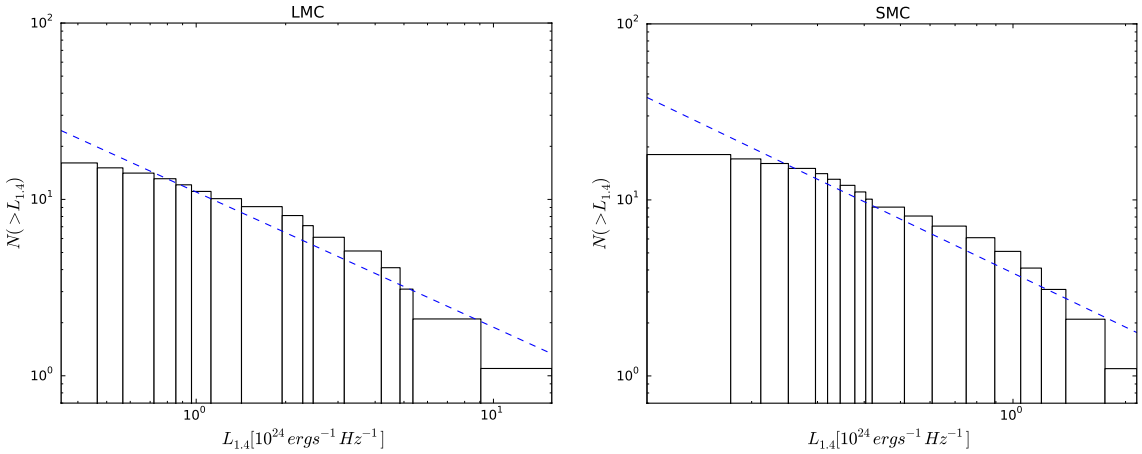

FIGURE 5.6: SNR Luminosity Function of LMC (left) and SMC (right) in a cumulative diagram. Blue dashed line correspond to the best fit.

hand, compensated the variable completeness of the sample for each galaxy by scaling each SNR with the host galaxy SFR taken from the literature, whose determination is strongly dependent on the tracer of the SFR, and hence is likely to bias the final results. (iii) I excluded the starburst galaxies (M82 and NGC253) and the U/LIRGs (Arp220 and Arp299) from this analysis, since these objects are intrinsically different and do not belong to the same SNRs-host galaxy kind. In fact, the inclusion of the starburst galaxies significantly bias, as expected, the final value of the universal β for normal galaxies.

5.2.4 Relationship between the radio luminosity function of SNRs and the magnetic field

Now I turn to study the relation of the RLF of SNRs with the magnetic field, as well as with other physical properties of the galaxies, following a similar discussion as presented in CW09, so as to facilitate comparison with their work.

For the sake of simplicity, I consider the SNR as an optically thin synchrotron radio emitting source. In this case, $S_\nu \propto \nu^{\frac{1-p}{2}}$, where p is the power-law index of the injected relativistic particle distribution. The p parameter is directly related to the observed spectral index $\alpha = \frac{1-p}{2}$). Further, the synchrotron (radio) emission of an optically thin source depends on the magnetic field as follows (see, e.g., Rybicki and Lightman, 1986):

$$\mathrm{L}_\nu \propto \mathrm{K(p)V\ N_0\ B}^{\frac{1+\mathrm{p}}{2}} \nu^{\frac{1-\mathrm{p}}{2}} \tag{5.4}$$

where L_ν is the luminosity at a given frequency, ν; $\mathrm{K(p)}$ is a slowly varying function

of the power-law index of the particle distribution p; V is the volume of the emitting region; B is the magnetic field strength in the SNR; and N_0 is the scaling factor of the relativistic electron energy distribution, $N(E)\,dE = N_0\ E^{-p}dE$. The value of $\mathrm{V\,N_0}$ depends on the energy of the supernova explosion E_{SN}.

I assume a standard electron energy spectrum, proportional to E^{-2}, i.e., $p = 2$, so that $\alpha = -0.5$. I also assume that all radio SNRs are in their Sedov phase. This is the longest phase in the life of an SNR, and hence most SNRs at any given time are likely to be found in this evolutionary stage. During the Sedov phase, the kinetic energy is transferred into internal energy, but the total energy stays roughly constant. The supernova size, velocity and temperature only depend on the energy of the supernova explosion (E_{SN}). Thus, the cosmic ray energy is independent of time and interstellar medium (ISM) density. Assuming a constant value for the energy in a supernova explosion, $\mathrm{E_{SN}}$, the synchrotron emission depends then only on the magnetic field strength, B.

In what follows, I discuss how the RLF of SNRs in local galaxies can contribute to test which scenario (or scenarios) explain better the amplification of the magnetic field that is needed to explain the observed luminosity of SNRs, and which are in turn related to fundamental properties of galaxies, such as the ISM. Namely, I discuss two of the most plausible scenarios: the compression and the turbulent scenarios.

Amplification of the magnetic field by compression

When a shock interacts with the ISM, the initial ISM magnetic field, $\mathrm{B_{ISM}}$, is amplified by a factor f. If a strong shock passes through a randomly oriented magnetic field, then $f = 3.32$ (Reynolds and Chevalier, 1981). The amplification of the magnetic field strength in a SNR that is in its Sedov phase can be approximated by the case above, and therefore the amplification of the magnetic field is given by f, which is a constant value. Further, since $V\,K \propto E_{SN}$, then Eq. (5.4) results in

$$L_\nu \propto B_{ISM}^{1.5} f^{1.5} E_{SN} \tag{5.5}$$

Defining the LF in terms of magnetic field strength:

$$\frac{dN}{dL_{1.4}} = \frac{dN}{dB_{\mathrm{ISM}}} \left(\frac{dL_{1.4}}{dB_{\mathrm{ISM}}} \right)^{-1} \tag{5.6}$$

To solve the second term, Eq. (5.5) turns to:

$$\frac{dL}{dB_{\rm ISM}} \propto E_{SN} B_{\rm ISM}^{1/2} f^{3/2} \tag{5.7}$$

Now I write the number of SNRs within some range of magnetic field strengths, as a power law of $B_{\rm ISM}$

$$\frac{dN}{dB_{\rm ISM}} = D\, B_{\rm ISM}^{\eta} \tag{5.8}$$

where D is a constant factor and η a constant index. From Eq. (5.5), one obtains $\rm B_{ISM}$ as a function of L_ν:

$$B_{\rm ISM} \propto f^{-1} L_\nu^{2/3} E_{SN}^{-2/3} \tag{5.9}$$

So finally

$$\frac{dN}{dL_{1.4}} \propto E_{SN}^{-2/3(\eta+1)} f^{-(\eta+1)} L_{1.4}^{2/3(\eta-1/2)} \tag{5.10}$$

From Eqs. (5.2) and (5.10), it then follows that , $\eta = (3\beta + 1)/2$, which relates the index of the observed radio LF of SNRs, β, with the index of the amplified magnetic field, η. I show in table 5.4 the η values found for each galaxy. For the universal value of $\beta = -2.33$, this yields $\eta \simeq -3.0$. Therefore, within the compression scenario, the number of SNRs would decrease roughly as $B_{\rm ISM}^{(\eta+1)} \simeq B_{\rm ISM}^{-2}$. This result has clear implications for the expected number of SNRs for two different galaxies, provided the average value of $B_{\rm ISM}$ is known for each galaxy.

I note here that the compression scenario fails to adequately explain the radio emission from young SNe (see, e.g., Pérez-Torres, Alberdi, and Marcaide, 2001, Pérez-Torres et al., 2005). However, the radio emission from young SNe is driven by the interaction with the circumstellar medium (CSM) rather than with the ISM, which is the relevant case here. The differences in luminosities for a given galaxy, or among them (excluding the starburst galaxies), are not larger than a factor of ∼100. Therefore, the variations in the local magnetic field need to be at least $\sim 100^{2/3} \approx 22$, as I am not taking into account the low-luminosity SNRs that are undetected. (This factor is even larger if starburst galaxies are taken into account, but it seems well established also that starburst galaxies have a significantly larger $B_{\rm ISM}$ (e.g. Thompson et al. 2006). Therefore, although this scenario is unlikely to apply for most galaxies, one cannot rule out completely due to the lack of information at low luminosity.

Galaxy	β	η
IC10	-1.32	-1.48
LMC	-2.16	-2.74
M33	-2.21	-2.81
M51	-2.49	-3.24
M81	-2.21	-2.81
M82	-2.02	-2.53
M83	-2.41	-3.11
NGC253	-1.87	-2.30
NGC300	-2.47	-3.20
NGC1569	-2.11	-2.67
NGC2366	-1.81	-2.21
NGC4214	-2.22	-2.83
NGC4258	-1.96	-2.44
NGC4449	-1.44	-1.66
NGC4736	-3.30	-4.45
NGC6946	-2.16	-2.63
NGC7793	-1.53	-2.74
SMC	-3.05	-4.08

TABLE 5.4: β and associated η parameters for each galaxy

Turbulent amplification of the magnetic field

An alternative scenario for the amplification of the magnetic field is the turbulent one, where turbulences amplify the magnetic field by a fraction ($f \equiv \delta B/B$) of the SNR pressure via the mechanism of Lucek and Bell, 2000, in which the amplification is carried out by Alfvén waves:

$$(\delta B/B)^2 = 2\frac{v_s}{v_A}\frac{P_{CR}}{\rho_{\rm ISM} v_s^2}$$

where B and δB are the initial and amplified magnetic field, respectively; v_s and v_A are the velocities of the shock and the Alfvén waves, respectively; P_{CR} is the cosmic ray pressure; and $\rho_{\rm ISM}$ is the ISM density. If the amplification mechanism is efficient (Voelk, Drury, and McKenzie, 1984; Bell, 1987; Falle and Giddings, 1987) then $P_{CR} \sim \rho_{\rm ISM} v_s^2$, and hence the (amplified) magnetic field can be rewritten as follows:

$$B^2 = 8\pi\, f\, \rho_{\rm ISM} v_s^2 \tag{5.11}$$

On the other hand, the Sedov self-similar solution implies that $v_s \propto (E_{SN}/\rho_{\rm ISM})^{1/5}\, t^{-3/5}$, resulting:

$$B \propto f^{1/2} E_{SN}^{1/5} \rho_{\rm ISM}^{3/10} t^{-3/5} \tag{5.12}$$

Thus, the synchrotron luminosity decreases with time during the Sedov phase, assuming that f is constant with time. It is related E_{SN} and synchrotron luminosity through 5.9, and 5.12:

$$L_\nu \propto E_{SN}^{13/10}\, {\rho_{\rm ISM}}^{9/20}\, t^{-9/10} \tag{5.13}$$

Now, the luminosity varies with time, and this, brought to the SNR LF (eq. 5.2), translates to:

$$\frac{dN}{dL_{1.4}} = \frac{dN}{dt}\left(\frac{dL_{1.4}}{dt}\right)^{-1}$$

For the second term, (5.13):

$$\frac{dL}{dt} \propto E_{SN}^{13/10}\, \rho_{\rm ISM}^{9/20} t^{-19/10} \tag{5.14}$$

One can write the previous equation in terms of the luminosity, using again the Equation 5.13 obtaining $t \propto L_\nu^{-10/9}\, {E_{\rm SN}}^{13/9}\, {\rho_{\rm ISM}}^{1/2}$. Then, Equation 5.14 turns into:

$$\frac{dL_{1.4}}{dt} \propto E_{SN}^{-13/9} \rho_{\rm ISM}^{-1/2} L_\nu^{19/9} \tag{5.15}$$

On the other hand, as it has been discussed in other sections, most radio SNRs are CCSN. If the Initial Mass Function (IMF) for all the galaxies in the sample is similar, then it is obtained in a natural way that $dN/dt \propto$ SFR. Hence, using the previous relation and equation 5.15, the radio LF of SNRs can be described as a function of their luminosity as follows:

$$\frac{dN}{dL_{1.4}} \propto E_{SN}^{13/9} \rho_0^{1/2} L_\nu^{-2.1}\ \text{SFR} \tag{5.16}$$

The value for the $\beta = -2.1$ parameter is, in agreement with CW09, closer to the corrected universal β parameter I have determined ($\beta = -2.33 \pm 0.03$). This suggests that the turbulent scenario looks very appropriate for the interpretation of the amplification mechanism of the magnetic fields in nearby normal galaxies.

Amplification of the magnetic field via saturation

In the case of very young SNRs, Bell (2004) has found, via non-linear simulations, that it is possible to reach a saturated magnetic field, which is driven by the highest CR energy. This magnetic field is expected to be caused by a large shock velocity as $B^2 \propto \rho v_s^3$. This saturated magnetic field is of the order of

$$B_{sat}^2 \sim \mu_0 \frac{v_s}{c} P_{CR}$$

where μ_0 is the permeability of the vacuum, v_s is the shock velocity, c is the speed of light and P_{CR} is the cosmic ray energy density. Therefore, if one follows the predictions for the amplified magnetic fields of Bell, 2004 and Vink, 2008, i.e., $B^2 \propto \rho_{\rm ISM} v_s^3$, instead of equation 5.11, the luminosity can be described as:

$$L_\nu \propto E_{SN}^{29/20} \rho_{\rm ISM}^{3/10} t^{-27/20} \tag{5.17}$$

And the new expression of the SNR LF becomes:

$$\frac{dN}{dL_{1.4}} \propto E_{SN}^{1.1} \rho_{\rm ISM}^{2/9} L_{1.4}^{-1.7}\ \text{SFR} \tag{5.18}$$

This implies $\beta = -1.7$, which is far from the universal $\beta = -2.33 \pm 0.03$. If the saturation model applies, it seems to be an extreme and particular case, and thus is very unlikely to be of general validity for SNRs.

5.2.5 The relation of A with the SFR

I now explore the possible relation of the parameter A in Eq. (5.2) with the physical properties of the SNRs and their host galaxies. For that purpose I use the individual A value from table 5.3, including the U/LIRGs, Arp299 and Arp220. The SNRs considered for Arp299-A were selected from Bondi et al. (2012) and their deep VLBI observations. Namely, I pre-selected SNRs that were detected above 7-σ in a stacked image including several epochs at C-band (5.0 GHz) spanning several years, and then selected only those SNRs that were detected at least above 3σ, excluding the confirmed AGN together with its jet (A1 and A5 in the nomenclature of Bondi et al. 2012). These considerations resulted in a total of 24 SNRs for Arp 299-A. The use of 5.0 GHz for these SNRs, instead of the 1.4 GHz flux used in the rest of galaxies, should not present a problem since in SNRs they trace just different evolutionary stages. The 5.0 GHz will trace more recent SNRs. I have considered sources present in different epochs, with little variation, suggesting they are, indeed, in a SNR phase. This ensure the completeness of the sample used. From Eq. (5.16), it follows that A should be proportional to the SFR (assuming E_{SN} and $\rho_{\rm ISM}$ are approximately constant). In Figure 5.7 we plot A vs. SFR from Tab.5.1. In the top panel are represented the normal and starburst galaxies, and in the bottom panel, the same galaxies including the U/LIRGs Arp220 and Arp299. For normal and starburst galaxies, the best fit corresponds to $A = (97 \pm 14) \times SFR^{0.82\pm0.10}$. Both for normal and starburst galaxies, and for the example including U/LIRGs, some of the galaxies lie outside the 95% confidence region (yellow region in Fig.5.7) but in general both of them tends to the expected linear dependence between A and SFR from Eqs. 5.16 and 5.18.

There are two galaxies that show a large departure from the slope, NGC7793 and NGC4449. Both galaxies have a rather small number of SNRs, so low-number statistics is very likely affecting them. Alternatively, there might be intrinsic reasons that could account for those results. For example, one implicitly assumed a constant explosion energy of 10^{51} erg for all CCSNe. However, E_{SN} can show values of up to (2-5)$\times 10^{52}$ erg (Woosley and Bloom, 2006). Even one or two cases which could account for the observed differences if a larger value of E_{SN} translates into an upward shift of A, and the reverse).

Moreover, it is worth mentioning that the dispersion is larger at low SFRs (and/or low A) due to the use of logarithmic scales. Thereby, taking the SNRLF A parameter

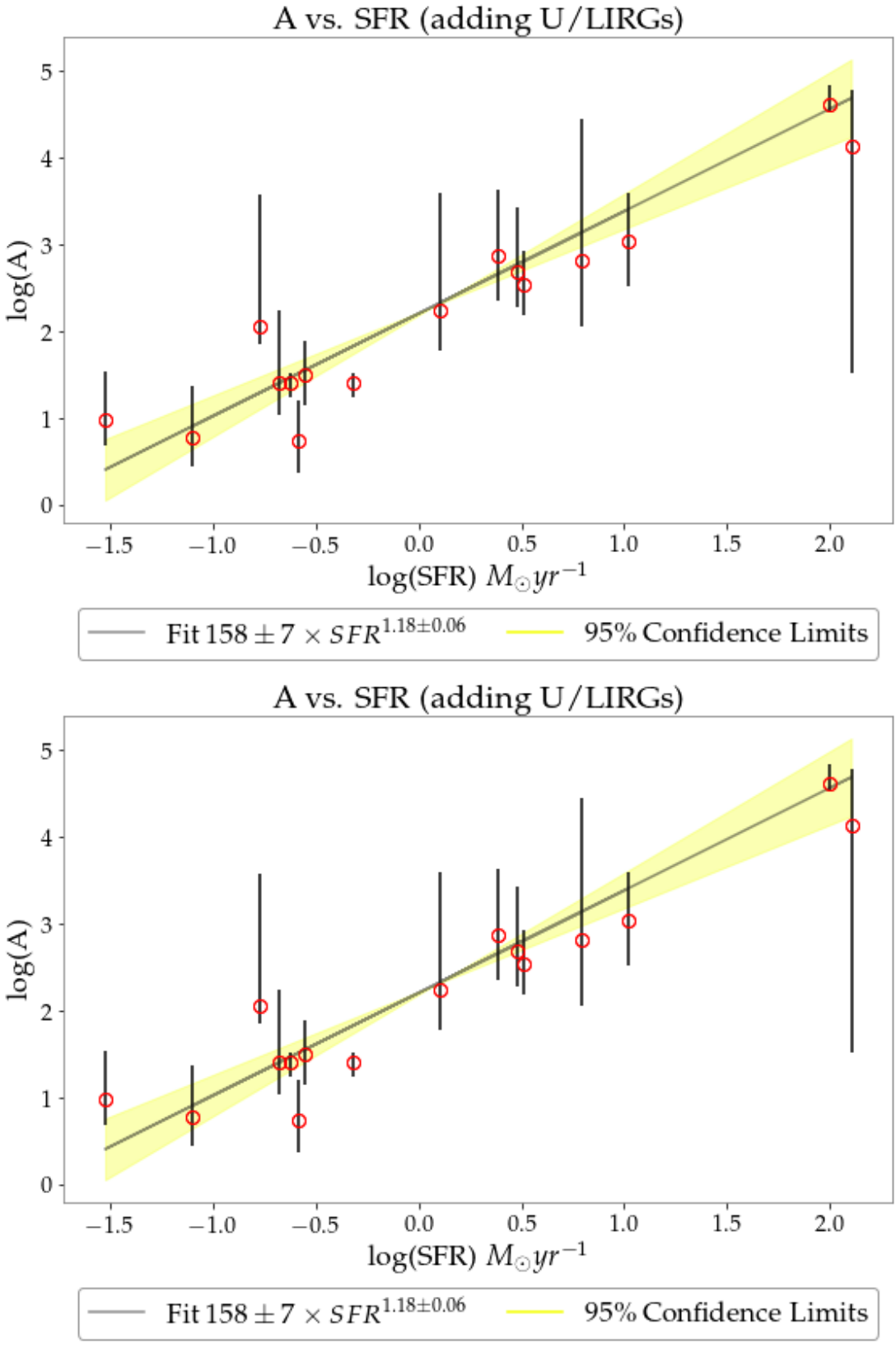

FIGURE 5.7: LF scaling factor A as a function of SFR (red open circles) represented in logarithmic scale and fitted by a power law through least squares. The black continuous line is the best fit to the data and yellow shadow corresponds to the 95% confidence region. *Top*: without the U/LIRGs, and *Bottom*: A vs. SFR including the U/LIRGs.

for a given galaxy, one is able to obtain the SFR, thus becoming in a new SFR estimator.

5.3 Summary

I have revisited the relevant topic of the universality of the radio luminosity function (LF) for SNRs in local galaxies. I used publicly available data from the literature to determine the radio LF of SNRs at 1.4 GHz, considering normal galaxies.

I used a novel approach in the statistical treatment of the data, namely the use of non-uniform bins. This approach is of general applicability, and helps to track and recognize different features of the LF (i.e. the L_{break}). Moreover, the treatment of the function with the cumulative histogram prevents the appearance of biases in the results. It is thus a more robust and confident approach than the widespread use of uniform binning and the differential LF.

The main conclusion is the confirmation of the existence of a universal (radio) luminosity function for SNRs in galaxies, provided that, apart for the true completeness limit for each galaxy SNR sample, a global true completeness limit is taken into account in the stacked sample. This meant removing starbursting galaxies and U/LIRGs from our sample, so as to avoid adding very bright SNRs, non existing (for probability) in normal galaxies. In other words, we show the existence of a universal radio luminosity function for normal, non-starbursting galaxies. Indeed, the radio LF of SNRs in the normal, non-starbursting galaxies of the sample is well described by a single power law ($n(L_{1.4}) = \frac{dN}{dL_{1.4}} = A\,L^{\beta}$) with an index $\beta = -2.33 \pm 0.03$. It would be very useful to obtain a statistically significant and complete sample of SNRs for starbursting and/or U/LIRGs to test whether a universal LF applies for SNRs in those galaxies.

I also found that A is close to being linearly proportional to the star formation rate (SFR), both for normal and starbursting galaxies, together with U/LIRGs ($A \propto \mathrm{SFR}^{0.82}$ and $A \propto \mathrm{SFR}^{1.20}$, respectively) and therefore A is a direct proxy of the recent star formation in a galaxy.

Finally, I discussed several scenarios for the amplification of the magnetic field that could account for the radio emission from SNRs. I agree with others in the sense that the compression scenario seems to be unrealistic, as it would require variations of the local ISM magnetic field in excess of a factor of 20. An amplification of the magnetic field via saturation (see section 3.3.3) seems also unrealistic. I therefore conclude that the most likely mechanism responsible of driving the radio emission from SNRs in the ISM is turbulent amplification of the magnetic field, which is also the most natural explanation for the radio emission from young SNe. This scenario predicts both a β

value close to the universal value, as well as a linear proportionality with the SFR, in agreement with the expectations of the universal radio luminosity function.

6 Summary and outlook

The general aim of this thesis has been to improve our understanding of the radio emission and absorption processes that take place in local U/LIRGs, using state-of-the-art radio interferometers that yield both high angular resolution (better than 1 arcsec) and high sensitivity at multiple frequencies. Such radio interferometric observations permit the characterization of the spectral energy distribution in the relevant GHz frequency range where non-thermal, synchrotron emission, as well as thermal free-free emission are known to contribute significantly.

I have presented preliminary results from the e-MERLIN LIRGI sample that, in spite of the sample being incomplete, show the potential of the sample. I have used LOFAR observations of our own, obtained for the first time for the well-known LIRGI Arp299, which led to a number of very important results thanks to the ability to probe emission and absorption processes at the largely unexplored frequency range of 100-200 MHz. Finally, I have studied the luminosity function of supernova remnants in a sample of nearby normal galaxies.

I highlight below the main results of this Thesis, and provide an outlook for future radio interferometric studies of U/LIRGs.

- I studied for the first time the very low-frequency ($\sim$150 MHz) radio brightness distribution of Arp 299 at subarcsecond resolution (0.4"$\sim$100 pc) using the Low-Frequency Array (LOFAR), and complemented these observations with 1.4, 5.0, and 8.4 GHz Very Large Array (VLA) observations. The high-surface brightness sensitivity of our LOFAR observations ($\sim$100 μJy/beam) allowed us to detect all of the nuclear components detected at higher frequencies, as well as the extended,

steep-spectrum emission surrounding the nuclei. I obtained spatially resolved, two-point spectral index maps for the whole galaxy: the compact nuclei show relatively flat spectra nuclei, while the extended, diffuse component shows a steep spectrum. Namely, The diffuse emission shows a two-point synchrotron spectral index between 150 MHz and 1.4 GHz, $\alpha \approx$ -0.7, typical of star-forming regions.

- I fitted the radio SED of the nuclear regions using two different models of the free-free absorbing/emitting thermal gas: in one model, the distribution of the free-free emitting particles is assumed to be a smooth continuous medium, whereas in the second, a clumpy medium is assumed. Both models fit well the existing data. The smooth, continuous model can explain the SED of the nuclei by a standard injected population of relativistic electrons subjected to synchrotron, Bremsstrahlung and ionization losses, which are expected due to the large densities encountered in the central regions of U/LIRGs. The clumpy model can explain the data by a population of relativistic electrons with negligible energy losses, and yields thermal fractions that are more typical of star-forming galaxies, compared to the continuous model. LOFAR observations at frequencies shorter than 100 MHz, or uGMRT observations at $\sim$600 MHz can unambiguously discern among those two competing models, and highlight the relevance of low-frequency, high-angular resolution observations in tracing the diffuse interstellar medium in galaxies.

- We made a specific study of the nucleus Arp 299A using only our LOFAR observations at 150 MHz. Our main finding is the presence of a two-sided, wide filamentary structure emanating from the A-nucleus, which we interpreted as an outflow that extends up to at least $\simeq$ 3 kpc from the A-nucleus along the N-S direction. Published HST/NICMOS [FeII] 1.64μm and H_2 at 2.12 μm images of Arp 299-A (Alonso-Herrero et al., 2000) show very similar features to those obtained by us with LOFAR at 150 MHz, leaving essentially no doubt about the existence of an outflow in Arp 299-A. From energy arguments, we ruled out a scenario where the AGN in Arp 299A is driving the outflow. On the other hand, the mechanical energy available from the starburst in the central regions of Arp 299-A is very large, which led us to conclude that the outflow in Arp 299-A is driven by the powerful starburst in its central regions. We estimate that the starburst wind can support a mass-outflow rate up to $\sim$60 $\mathrm{M_{\odot} yr^{-1}}$, and that it is relatively recent, with an estimated kinematic age of $(3-7)$ Myr.

  I found tentative evidence of the presence of another outflow in the B nucleus, from our 150 MHz LOFAR observations. From energy considerations, this possible outflow is more likely to be AGN-driven, unlike the case of the starburst-driven outflow in Arp 299-A.

Our results indicate that sub-arcsecond imaging with LOFAR may be an excellent new tool for unveiling outflows in the central regions of local LIRGs.

- I have presented preliminary results for 7 of the 42 U/LIRGs in LIRGI, observed with eMERLIN at 5.0 GHz. All of the images show suggestive evidence for the existence of an AGN, a starburst, or both. The angular resolution of e-MERLIN is intermediate between that provided by the JVLA and the EVN at the same frequencies. It is therefore a very useful tool to trace the several arcsecond extended radio emission down to compact radio components of about 60 milliarcsecond in size at 5 GHz. Although the main goal of LIRGI is to provide a legacy value to the community, the current data set, even if small, gives a taste of what can be expected once the sample is completely observed.

  Just to focus on an example, I highlight here the detection with eMERLIN at C-band of a new SN in the A nucleus of Arp299. The radio luminosity of this SN is $L \approx 6 \times 10^{28} erg\, s^{-1} Hz{-}1$, a value that puts this SN among the brightest radio supernovae ever discovered in a starburst. Further observations will allow us to trace the evolution of its luminosity, and we will submit an EVN proposal at both C- and L-bands to trace the evolution of this and other compact radio sources in Arp 299.

- I have studied the luminosity function of supernova remnants (SNRs) in normal galaxies, aimed at building up a Universal luminosity function. To this end, I wrote a code that uses a non-uniform binning size, which avoids introducing biases in the survey due to the small size of some of the SNR samples. To calculate the parameters A and β of the luminosity function, I used a Monte Carlo approach. The main result is the detection of a new (true) completeness limit in the overall sample due to the presence of starbursting galaxies.

  The value of A is linearly proportional to the star-formation rate (SFR) for normal galaxies ($A \propto$SFR$^{0.82}$), as well as for the total sample of normal, starbursting galaxies and U/LIRGs ($A \propto$SFR$^{1.20}$). Future SNRs samples of starbursting galaxies and U/LIRGs are necessary to statistically confirm this linear trend.

  Using the new values found of the Universal luminosity function, I confirm that the most likely scenario for the magnetic field to accelerate electrons to relativistic velocities is the turbulent amplification of the magnetic field.

The results obtained on Arp 299A confirm the usefulness of combining spatially resolved radio imaging in the ∼100-200 MHz up to about 1-8 GHz frequencies to characterize in detail the radio emission properties of LIRGs from the central 100 pc out to the kiloparsec, galaxy-wide scales. In particular, the frequency range from ∼100 MHz

up to ∼1.4 GHz is crucially important to discern which free-free absorber dominates in the interstellar medium of the nuclei in LIRGs, as well as to inform about the dominant energy loss mechanisms. Similarly, the discovery of an starburst-driven outflow in Arp 299A, and a possible one in Arp 299B, thanks to our LOFAR observations, opens the avenue to the detection, or confirmation, of more outflows in such systems.

The SKA, which is expected to become a reality during this decade, will allow to obtain a continuous frequency range from ∼100 MHz up to at least 5-8 GHz (and possibly up to around 20 GHz), so the perspectives of detecting outflows, and characterizing in detail the radio emission and absorption processes in local U/LIRGs, will be done in a systematic way.

A Spectral models for a clumpy free-free medium

The derivation of an expression for the spectrum emerging from a mixed synchrotron emitting and clumpy free-free absorbing/emitting medium is explained here. This derivation is based on the clumpy medium formalism of Conway, Elitzur, and Parra (2018). Similar spectra are predicted by Lacki (2013) who considered the detailed physical properties of the HII regions that likely comprise the free-free absorbing clumps in Luminous Infra-Red Galaxies (LIRGs). An advantage of the more phenomenological based derivation presented here is that the final expression has the same free parameters as the continuous free-free model (Eq. 2.3) with the addition of N_{cl} the mean number of clumps intercepted per LOS. A detailed comparison of the phenomenological and physical approaches of respectively Conway, Elitzur, and Parra (2018) and Lacki (2013) is deferred to a future paper in preparation (Conway et al. in prep.).

For the mixed medium under consideration there are two components of emission comprising respectively; (A) clumpy free-free emission and (B) smooth synchrotron emission mixed with a clumpy free-free absorbing medium. Although in LIRGs it is invariably the B component that dominates the radio spectrum below 10 GHz it is convenient to consider first the A component. An expression for emission from this component is given in Eq. 15 of Conway, Elitzur, and Parra (2018). Converting to radio astronomy units the brightness in mJy/arcsec^2 is given by

$$7.22\nu^2(T_e/10^4)(1-e^{-\tau_{eff,\nu}}) \tag{A.1}$$

where the frequency ν is in units of GHz, T_e is in Kelvin and the *effective opacity* $\tau_{eff,\nu}$, incorporating all clumping effects, is defined by

$$\tau_{eff,\nu} = N_{cl} < 1 - exp(-\tau_{cl,\nu}) > \tag{A.2}$$

In this expression, N_{cl} is the mean number of clumps intercepted per LOS and $\tau_{cl,\nu}$ represents the opacity at frequency ν along a LOS through an individual clump. The diagonal brackets denote an average over all impact parameters through all types of clumps within the clump population. Here, it is assumed for simplicity one type of identical uniform emissivity spherical clump[1] so the average is taken only over impact parameter.

The effective opacity $\tau_{eff,\nu}$, once the clump geometry is defined, is exactly determined via Eq. A.2 by the values of N_{cl} and of $< \tau_{cl,\nu} >$, the mean clump opacity averaged over all impact parameters at a frequency ν. If ν_t is defined as the frequency at which the *total opacity* (the mean opacity through all clumps along a LOS) equals unity then $< \tau_{cl,\nu} >= {N_{cl}}^{-1}(\nu/\nu_t)^{-2.1}$. For a spherical clump with uniform internal emissivity the opacity across a diameter (zero impact parameter) at frequency ν is $(3/2) < \tau_{cl,\nu} >$ (Conway, Elitzur, and Parra, 2018). The value of $\tau_{cl,\nu}$ in Eq. A.2 for other impact parameters simply scales with path length through the clump. Given the above then after taking the average in Eq. A.2 over all impact parameters the value of $\tau_{eff,\nu}$ versus frequency is fully determined by the choice of ν_t and N_{cl}.

An expression for the second (B) emission component, of synchrotron emission modified by clumpy free-free absorption, is given by Equation 42 of Conway, Elitzur, and Parra (2018) as

$$S_\nu \frac{(1 - e^{-\tau_{eff,\nu}})}{\tau_{eff,\nu}} \tag{A.3}$$

Where S_ν is the unabsorbed synchrotron spectrum. Following Condon et al. (1991) we assume this underlying synchrotron emission is a power law with spectral index α which can be linked to the free-free emission by the parameter f_{th} the thermal to synchrotron ratio at 1 GHz. This parameter is defined as the ratio of the *unabsorbed* free-free to *unabsorbed* synchrotron emission at 1 GHz. Defining the thermal/synchrotron ratio in this way makes it proportional to the ratio of respectively the efficiencies of thermal emission per unit star-formation and of synchrotron emission per unit star-formation.

The unabsorbed free-free emission at 1 GHz extrapolated from high frequency can

[1] Lacki (2013) investigated models involving a distribution of non-identical clumps (i.e. HII regions) showing only small spectral effects. Additionally, Conway, Elitzur, and Parra (2018) shows that the exact clump shape also has little effect.

be calculated by taking the high frequency limit of Eq. A.2 for which $\tau_{cl,\nu} << 1$ and then setting ν= 1 GHz. This approach gives an extrapolated unabsorbed thermal brightness at 1 GHz of $7.22\,(T_e/10^4)\,{\nu_t}^{2.1}$ with the unabsorbed synchrotron emission at this frequency being, by definition, ${f_{th}}^{-1}$ times this value. Using this normalisation for S_ν in Eq. A.3 and adding the expression for the free-free clumpy emission component from Eq. A.1 the total emerging spectrum is

$$7.22\nu^2(T_e/10^4)(1-e^{-\tau_{eff,\nu}})\left[1+{\tau_{eff,\nu}}^{-1}{f_{th}}^{-1}{\nu_t}^{2.1}\nu^{\alpha-2}\right] \tag{A.4}$$

in units of mJy/arcsec^2, where ν and ν_t are measured in GHz and T_e in Kelvin. The effective free-free opacity $\tau_{eff,\nu}$ in the above equation, as described earlier, is a function of N_{cl} and ν_t.

It is interesting to consider Eq. A.4 in the limits of very high or very low frequencies. At high frequencies, when the opacity through individual clumps ($\tau_{cl,\nu}$) is much less than unity, $\tau_{eff,\nu} \approx N_{cl} < \tau_{\nu_{cl}} >= \tau_\nu$; i.e. the effective opacity is the same as the total mean opacity through all clumps along a line of sight. In this case $\tau_{eff,\nu} = (\nu/\nu_t)^{-2.1}$; where ν_t is the frequency at which total opacity equals unity. Substituting this expression into Eq. A.4 we recover Eq. 2.3 which in turn describes a spectrum peaking close to frequency ν_t. If one now considers very low frequencies such that individual clumps are completely optically thick then $\tau_{eff,\nu} \approx N_{cl}$, i.e. the effective opacity is a constant versus frequency and so (ignoring the very small contribution at low frequencies from free-free emission) from Eq. A.4, the spectrum follows the intrinsic synchrotron power-law shape after multiplication by a constant factor equal to $(1 - exp(-N_{cl}))/N_{cl}$).

The high and low frequency limits above give rise, for interesting cases with mean number of clumps intercepted per LOS $N_{cl} > 1$, to a characteristic clump model spectrum shape (see clump models in top two panels of Fig. 2.4 and Conway, Elitzur, and Parra (2018) Fig 6). At high frequencies this spectrum is identical to that of the continuous model spectrum (Eq. 2.3) calculated for the same values of f_{th}, T_e, α and ν_t, i.e. a spectrum showing a spectral peak close to frequency ν_t. Below this turnover frequency the spectrum at first decreases rapidly until a local minimum is reached below which the spectrum turns up again. This spectral turn-up occurs at the frequency at which the opacity of individual clumps becomes unity; this occurs at $N_{cl}^{-1/2.1}$ times the turnover frequency, ν_t, at which the total opacity through the medium is unity. In fitting observed data, given a low turnover frequency and a sufficiently high mean number of clumps the spectral turn-up can occur at a frequency below that of the lowest observed frequency data point. In such cases, the continuous model can provide a good fit to the data even if the free-free medium is in fact clumpy in nature. A truly continuous free-free absorbing medium is one in which the effective number of clumps goes to

infinity, in which case the turn-up frequency goes to zero and the continuous free-free medium spectral model then applies at all frequencies. The work of Conway, Elitzur, and Parra (2018) wrongly claimed in a footnote that the expression in Condon et al. (1991), leaving out a factor of $1/\tau_\nu$. In fact, as shown above, the general expression (Eq. A.4), which does include this factor, reduces to the expression of Condon et al. (1991) in the limit of an infinite number of clumps and hence of a continuous medium.

B Calculation of the equipartition magnetic field parameters

I am going to itemize the needs for each value and parameter of the magnetic field expression, Eq. 2.2:

- c_{12}: it depends on the synchrotron spectral index,α_{nth}^{cont} (see Sec.2.4.1 for deep explanation), derived from the Eq. 2.3 fit between the two frequencies I am using to calculate L_R (150 MHz and 8.4 GHz). c_{12} also directly depends on these two frequencies.
- R: As described above, I will take the area which enclose up to the 50% of the peak in the convolved image at 1.4 GHz.
- L_R: This is the integrated radio luminosity between two frequencies (150 MHz and 8.4 GHz in this case). This radio luminosity has to be of non-thermal (synchrotron) nature, so:
  - I first calculate the synchrotron contribution in flux at 8.4 GHz,$S_{nth,X}$, through the non-thermal fraction,$f_{nth,X}$, at this frequency.

$$S_{nth,X} = f_{nth,X} \cdot S_X \tag{B.1}$$

    where S_X is the total flux in X band (thermal and non-thermal emission). This value is the total flux for each component reported in Tab. 2.3. For $f_{nth,X}$, I turn to the Eq. 2.3 fit parameter $f_{th,1\,GHz}^{cont}$ at 1 GHz(see Table 2.3) and I apply the Eq. 7 from Condon et al. (1991) for galaxies with a free-free optical depth of $\tau_{ff} << 1$. The resulting general expression to obtain it at

any frequency is:

$$f_{nth,\nu} = 1 - \left[1 + f^{cont}_{th,1\,GHz} \left(\frac{\nu}{1\,GHz}\right)^{0.1+\alpha^{cont}_{nth}}\right]^{-1} \tag{B.2}$$

– Then, I extrapolate the synchrotron flux above calculated at 8.4 GHz to 150 MHz:

$$S_{nth,150\,MHz} = S_{nth,X} \left(\frac{\nu_{150\,MHz}}{\nu_X}\right)^{\alpha^{cont}_{nth}} \tag{B.3}$$

With this information ($S_{nth,X}$ and $S_{nth,150\,MHz}$) one can measure the L_R between 8.4 GHz and 150 MHz (the biggest range of frequencies I have). For a luminosity in a given frequency (L_ν), the relation with the flux in a given frequency (S_ν) can be expressed in useful units as:

$$\frac{L_\nu}{\mathrm{erg \cdot s^{-1} Hz^{-1}}} = \underbrace{1.19 \times 10^{24} \left(\frac{D}{\mathrm{Mpc}}\right)^2}_{\mathrm{A}_L} \left(\frac{S_\nu}{\mathrm{mJy}}\right) \tag{B.4}$$

where D is the distance to the galaxy in Mpc, S_ν is given in mJy, and L_ν is given in units of $erg \cdot s^{-1} Hz^{-1}$. The constant factor before S_ν is renamed as A_L. Then, I integrate the luminosity between both frequencies. The final expression for this total radio luminosity between 150 MHz and 8.4 GHz is:

$$L_R = \frac{\Delta\nu}{2} A_L \left[1 + \left(\frac{\nu_{150\ MHz}}{\nu_X}\right)^{\alpha^{cont}_{nth}}\right] \left[1 - \left[1 + \left(f^{cont}_{th,1\ GHz}\right)^{-1} \left(\frac{\nu}{1\ GHz}\right)^{0.1+\alpha^{cont}_{nth}}\right]\right] S_{tot,X} \tag{B.5}$$

where $\Delta\nu$ is the width in frequency between 8.4 GHz and 150 MHz. With this value one can calculate the magnetic field for each nuclear region by following the prescription of Eq. 2.2.

I note that these values correspond to the continuous case discussed in Sec. 2.4.1, since in the clumpy model (Sec. 2.4.1) the size of each clump is not considered, and hence the fitting process cannot be carried out.

liography

Aalto, S. et al. (Feb. 1997). "Variation of Molecular Line Ratios and Cloud Properties in the ARP 299 Galaxy Merger". In: *ApJ* 475.2, pp. L107–L110. DOI: 10.1086/310475. arXiv: astro-ph/9701005 [astro-ph].

Alberdi, A. et al. (Feb. 2006). "Evolution of the Circumnuclear Radio Supernova SN 2000ft in NGC 7469". In: *ApJ* 638.2, pp. 938–945. DOI: 10.1086/498859.

Alberdi, A. et al. (Oct. 2008). "High resolution radio observations of nuclear and circumnuclear regions of luminous infrared galaxies (LIRGs)". In: *Journal of Physics Conference Series*. Vol. 131. Journal of Physics Conference Series, p. 012037. DOI: 10.1088/1742-6596/131/1/012037.

Alonso-Herrero, A. et al. (Apr. 2000). "Extreme Star Formation in the Interacting Galaxy Arp 299 (IC 694+NGC 3690)". In: *ApJ* 532, pp. 845–866. DOI: 10.1086/308622. eprint: astro-ph/9911534.

Alonso-Herrero, A. et al. (Dec. 2013). "Uncovering the Deeply Embedded Active Galactic Nucleus Activity in the Nuclear Regions of the Interacting Galaxy Arp 299". In: *ApJ* 779, L14, p. L14. DOI: 10.1088/2041-8205/779/1/L14. arXiv: 1311.3446.

Alonso-Herrero, Almudena et al. (Mar. 2003). "The [Fe II] 1.644 Micron Emission in M82 and NGC 253: Is It a Measure of the Supernova Rate?" In: *AJ* 125.3, pp. 1210–1225. DOI: 10.1086/367790. arXiv: astro-ph/0212142 [astro-ph].

Arribas, Santiago and Luis Colina (July 2003). "INTEGRAL Spectroscopy of IRAS 17208-0014: Implications for the Evolutionary Scenarios of Ultraluminous Infrared Galaxies". In: *ApJ* 591.2, pp. 791–800. DOI: 10.1086/375417. arXiv: astro-ph/0304138 [astro-ph].

Arribas, Santiago et al. (May 2004). "Optical Imaging of Very Luminous Infrared Galaxy Systems: Photometric Properties and Late Evolution". In: *AJ* 127.5, pp. 2522–2543. DOI: 10.1086/386352. arXiv: astro-ph/0402375 [astro-ph].

Baan, W. A. and H. R. Klöckner (Apr. 2006). "Radio properties of FIR-megamaser nuclei". In: *A&A* 449.2, pp. 559–568. DOI: 10.1051/0004-6361:20042331.

Baan, Willem A. (Mar. 1989). "Infrared Properties of OH Galaxies". In: *ApJ* 338, p. 804. DOI: 10.1086/167237.

Baan, Willem A., John J. Salzer, and Robin D. LeWinter (Dec. 1998). "Optical Classification of Megamaser Galaxies". In: *ApJ* 509.2, pp. 633–645. DOI: 10.1086/306504.

Barcos-Muñoz, L. et al. (Jan. 2015). "High-resolution Radio Continuum Measurements of the Nuclear Disks of Arp 220". In: *ApJ* 799.1, 10, p. 10. DOI: 10.1088/0004-637X/799/1/10. arXiv: 1411.0932 [astro-ph.GA].

Barcos-Muñoz, L. et al. (July 2017). "A 33 GHz Survey of Local Major Mergers: Estimating the Sizes of the Energetically Dominant Regions from High-resolution Measurements of the Radio Continuum". In: *ApJ* 843.2, 117, p. 117. DOI: 10.3847/1538-4357/aa789a. arXiv: 1705.10801 [astro-ph.GA].

Basu, Aritra et al. (June 2015). "Synchrotron spectral index and interstellar medium densities of star-forming galaxies". In: *MNRAS* 449.4, pp. 3879–3888. DOI: 10.1093/mnras/stv510. arXiv: 1503.02420 [astro-ph.GA].

Batejat, F. et al. (2010). "Compact source resolution and rapid variability in Arp220". In: *10th European VLBI Network Symposium and EVN Users Meeting: VLBI and the New Generation of Radio Arrays*, p. 59. arXiv: 1011.4063 [astro-ph.CO].

Bell, A. R. (Jan. 1978a). "The acceleration of cosmic rays in shock fronts - I." In: *MNRAS* 182, pp. 147–156. DOI: 10.1093/mnras/182.2.147.

— (Feb. 1978b). "The acceleration of cosmic rays in shock fronts - II." In: *MNRAS* 182, pp. 443–455. DOI: 10.1093/mnras/182.3.443.

— (Apr. 1987). "The non-linear self-regulation of cosmic ray acceleration at shocks". In: *MNRAS* 225, pp. 615–626. DOI: 10.1093/mnras/225.3.615.

— (Sept. 2004). "Turbulent amplification of magnetic field and diffusive shock acceleration of cosmic rays". In: *MNRAS* 353, pp. 550–558. DOI: 10.1111/j.1365-2966.2004.08097.x.

Berezhko, E. G. and H. J. Völk (Nov. 2004). "The theory of synchrotron emission from supernova remnants". In: *A&A* 427, pp. 525–536. DOI: 10.1051/0004-6361:20041111. eprint: astro-ph/0408121.

Bingham, Richard G. et al. (1994). "Fiber-fed spectrograph for the 4.2-m William Herschel Telescope". In: *Proc. SPIE Vol. 2198, p. 56-64, Instrumentation in Astronomy VIII, David L. Crawford; Eric R. Craine; Eds.* Ed. by David L. Crawford and Eric R. Craine. Vol. 2198. Society of Photo-Optical Instrumentation Engineers (SPIE) Conference Series, pp. 56–64. DOI: 10.1117/12.176776.

Bondi, M. et al. (Jan. 2004). "A detailed study of the nuclear region of Mrk273". In: *European VLBI Network on New Developments in VLBI Science and Technology*, pp. 121–124. arXiv: astro-ph/0412659 [astro-ph].

Bondi, M. et al. (Aug. 2005). "A supernova factory in Mrk 273?" In: *MNRAS* 361.2, pp. 748–752. DOI: 10.1111/j.1365-2966.2005.09206.x. arXiv: astro-ph/0505370 [astro-ph].

Bondi, M. et al. (Mar. 2012). "The nuclear starburst in Arp 299-A: from the 5.0 GHz VLBI radio light-curves to its core-collapse supernova rate". In: *A&A* 539, A134, A134. DOI: 10.1051/0004-6361/201118446. arXiv: 1201.3220.

Brogan, C. L. et al. (Mar. 2006). "Discovery of 35 New Supernova Remnants in the Inner Galaxy". In: *ApJ* 639, pp. L25–L29. DOI: 10.1086/501500. eprint: astro-ph/0601451.

Calzetti, D. et al. (Sept. 2007). "The Calibration of Mid-Infrared Star Formation Rate Indicators". In: *ApJ* 666, pp. 870–895. DOI: 10.1086/520082. arXiv: 0705.3377.

Carilli, C. L. and G. B. Taylor (Apr. 2000). "The Extreme Compact Starburst in Markarian 273". In: *ApJ* 532.2, pp. L95–L99. DOI: 10.1086/312584. arXiv: astro-ph/0002186 [astro-ph].

Casasola, V. et al. (Oct. 2007). "Molecular clouds in the center of M 81". In: *A&A* 473.3, pp. 771–781. DOI: 10.1051/0004-6361:20077883. arXiv: 0707.4234 [astro-ph].

Cazzoli, S. et al. (Apr. 2020). "NGC 7469 as seen by MEGARA: new results from high-resolution IFU spectroscopy". In: *MNRAS* 493.3, pp. 3656–3675. DOI: 10.1093/mnras/staa409. arXiv: 2002.04031 [astro-ph.GA].

Chandrasekhar, S. (Mar. 1931). "The highly collapsed configurations of a stellar mass". In: *MNRAS* 91, pp. 456–466. DOI: 10.1093/mnras/91.5.456.

Chevalier, R. A. (Aug. 1982). "The radio and X-ray emission from type II supernovae". In: *ApJ* 259, pp. 302–310. DOI: 10.1086/160167.

Chevalier, R. A. and C. Fransson (Oct. 2001). "Supernova Interaction with a Circumstellar Medium". In: *ArXiv Astrophysics e-prints*. eprint: astro-ph/0110060.

Chomiuk, L. and E. M. Wilcots (Sept. 2009). "A Universal Luminosity Function for Radio Supernova Remnants". In: *ApJ* 703, pp. 370–389. DOI: 10.1088/0004-637X/703/1/370. arXiv: 0907.4783.

Colina, L. et al. (Feb. 2001). "Probable Radio Supernova in NGC 7469". In: *IAU Circ.* 7587, p. 1.

Colina, L. et al. (May 2007). "Optical detection of the radio supernova SN 2000ft in the circumnuclear region of the luminous infrared galaxy NGC 7469". In: *A&A* 467.2, pp. 559–564. DOI: 10.1051/0004-6361:20067043. arXiv: astro-ph/0703481 [astro-ph].

Combes, F. et al. (Oct. 2013). "ALMA observations of feeding and feedback in nearby Seyfert galaxies: an AGN-driven outflow in NGC 1433". In: *A&A* 558, A124, A124. DOI: 10.1051/0004-6361/201322288. arXiv: 1309.7486 [astro-ph.CO].

Condon, J. J., M. L. Anderson, and G. Helou (July 1991). "Correlations between Far-Infrared, Radio, and Blue Luminosities of Spiral Galaxies". In: *ApJ* 376, p. 95. DOI: 10.1086/170258.

Condon, JJ (1992). "Radio emission from normal galaxies". In: *Annual review of astronomy and astrophysics* 30.1, pp. 575–611.

Condon, JJ et al. (1991). "Compact starbursts in ultraluminous infrared galaxies". In: *The Astrophysical Journal* 378, pp. 65–76.

Conway, John E., Moshe Elitzur, and Rodrigo Parra (Sept. 2018). "Continuum and Spectral Line Radiation from a Random Clumpy Medium". In: *ApJ* 865.1, 70, p. 70. DOI: 10.3847/1538-4357/aadcf9. arXiv: 1808.07538 [astro-ph.GA].

Cox, T. J. et al. (Feb. 2008). "The effect of galaxy mass ratio on merger-driven starbursts". In: *MNRAS* 384.1, pp. 386–409. DOI: 10.1111/j.1365-2966.2007.12730.x. arXiv: 0709.3511 [astro-ph].

Davidge, T. J. (Dec. 2010). "Shaken, Not Stirred: The Disrupted Disk of the Starburst Galaxy NGC 253". In: *ApJ* 725, pp. 1342–1365. DOI: 10.1088/0004-637X/725/1/1342. arXiv: 1011.3006.

Della Ceca, R. et al. (Dec. 2002). "An Enshrouded Active Galactic Nucleus in the Merging Starburst System Arp 299 Revealed by BeppoSAX". In: *ApJ* 581.1, pp. L9–L13. DOI: 10.1086/345925. arXiv: astro-ph/0211077 [astro-ph].

Díaz-Santos, T. et al. (May 2007). "Resolving the Stellar Populations in the Circumnuclear Ring of NGC 7469". In: *ApJ* 661.1, pp. 149–164. DOI: 10.1086/513089. arXiv: astro-ph/0701557 [astro-ph].

Falle, S. A. E. G. and J. R. Giddings (Mar. 1987). "Time-dependent cosmic ray modified shocks". In: *MNRAS* 225, pp. 399–423. DOI: 10.1093/mnras/225.2.399.

Farrah, D. et al. (Aug. 2003). "Starburst and AGN activity in ultraluminous infrared galaxies". In: *MNRAS* 343.2, pp. 585–607. DOI: 10.1046/j.1365-8711.2003.06696.x. arXiv: astro-ph/0304154 [astro-ph].

Frail, D. A., W. M. Goss, and J. B. Z. Whiteoak (Dec. 1994). "The radio lifetime of supernova remnants and the distribution of pulsar velocities at birth". In: *ApJ* 437, pp. 781–793. DOI: 10.1086/175038. eprint: astro-ph/9407031.

García-Burillo, S. et al. (July 2014). "Molecular line emission in NGC 1068 imaged with ALMA. I. An AGN-driven outflow in the dense molecular gas". In: *A&A* 567, A125, A125. DOI: 10.1051/0004-6361/201423843. arXiv: 1405.7706 [astro-ph.GA].

García-Marín, M. et al. (Oct. 2006). "Integral Field Spectroscopy of the Luminous Infrared Galaxy Arp 299 (IC 694 + NGC 3690)". In: *ApJ* 650.2, pp. 850–871. DOI: 10.1086/507411. arXiv: astro-ph/0606585 [astro-ph].

Gehrz, R. D., R. A. Sramek, and D. W. Weedman (Apr. 1983). "Star bursts and the extraordinary galaxy NGC 3690". In: *ApJ* 267, pp. 551–562. DOI: 10.1086/160892.

Genzel, R. et al. (May 1995). "Infrared Imaging and Spectroscopy of NGC 7469". In: *ApJ* 444, p. 129. DOI: 10.1086/175588.

Goldader, Jeffrey D. et al. (May 1997). "Heavily Obscured Star Formation in the II ZW 96 Galaxy Merger". In: *AJ* 113, pp. 1569–1579. DOI: 10.1086/118374.

Greenhouse, Matthew A. et al. (Feb. 1997). "Infrared Fabry-Perot Imaging of M82 [Fe II] Emission. II. Tracing Extragalactic Supernova Remnants". In: *ApJ* 476.1, pp. 105–112. DOI: 10.1086/303599.

Heckman, T. M. et al. (May 1999). "An X-Ray and Optical Investigation of the Starburst-driven Superwind in the Galaxy Merger ARP 299". In: *ApJ* 517.1, pp. 130–147. DOI: 10.1086/307193. arXiv: astro-ph/9812317 [astro-ph].

Heckman, Timothy M. et al. (Aug. 2000). "Absorption-Line Probes of Gas and Dust in Galactic Superwinds". In: *ApJS* 129.2, pp. 493–516. DOI: 10.1086/313421. arXiv: astro-ph/0002526 [astro-ph].

Herrero-Illana, R., M. Á. Pérez-Torres, and A. Alberdi (Apr. 2012). "Evidence of nuclear disks in starburst galaxies from their radial distribution of supernovae". In: *A&A* 540, L5, p. L5. DOI: 10.1051/0004-6361/201118545. arXiv: 1203.2927.

Herrero-Illana, Rubén et al. (Oct. 2017). "Star formation and AGN activity in a sample of local luminous infrared galaxies through multiwavelength characterization". In: *MNRAS* 471.2, pp. 1634–1651. DOI: 10.1093/mnras/stx1672. arXiv: 1705.09663 [astro-ph.GA].

Ho, Luis C., Alexei V. Filippenko, and Wallace L. W. Sargent (Oct. 1997). "A Search for "Dwarf" Seyfert Nuclei. III. Spectroscopic Parameters and Properties of the Host Galaxies". In: *ApJS* 112.2, pp. 315–390. DOI: 10.1086/313041. arXiv: astro-ph/9704107 [astro-ph].

Hopkins, Philip F. et al. (Apr. 2008). "A Cosmological Framework for the Co-Evolution of Quasars, Supermassive Black Holes, and Elliptical Galaxies. I. Galaxy Mergers and Quasar Activity". In: *ApJS* 175.2, pp. 356–389. DOI: 10.1086/524362. arXiv: 0706.1243 [astro-ph].

Hopkins, Philip F. et al. (Sept. 2009). "Are most low-luminosity active galactic nuclei really obscured?" In: *MNRAS* 398.1, pp. 333–349. DOI: 10.1111/j.1365-2966.2009.15136.x. arXiv: 0901.2936 [astro-ph.GA].

Hunt, L. K. and S. P. Reynolds (June 2006). "Environment and luminosity of supernova remnants". In: *Astronomische Nachrichten* 327, p. 448. DOI: 10.1002/asna.200610554.

Inami, H. et al. (July 2010). "The Buried Starburst in the Interacting Galaxy II Zw 096 as Revealed by the Spitzer Space Telescope". In: *AJ* 140.1, pp. 63–74. DOI: 10.1088/0004-6256/140/1/63. arXiv: 1004.3543 [astro-ph.CO].

Iwasawa, K. et al. (Apr. 2011). "The location of an active nucleus and a shadow of a tidal tail in the ULIRG Mrk 273". In: *A&A* 528, A137, A137. DOI: 10.1051/0004-6361/201015872. arXiv: 1101.3659 [astro-ph.CO].

Johnson, H. L. (Jan. 1966). "Infrared Photometry of Galaxies". In: *ApJ* 143, p. 187. DOI: 10.1086/148489.

Johnson, H. M. and J. M. MacLeod (Apr. 1963). "The Spatial Distribution of Supernovae in Galaxies". In: *PASP* 75, p. 123. DOI: 10.1086/127915.

Juneau, Stephanie (Jan. 2011). "Connecting galaxy and supermassive black hole growth during the last 8 billion years". PhD thesis. The University of Arizona.

Kaufman, Michele et al. (Oct. 1989). "A Comparison of Spiral Tracers in M81". In: *ApJ* 345, p. 674. DOI: 10.1086/167941.

Keel, W. C. and W. Wu (July 1995). "The Local Merger Rate of Disk Galaxies". In: *AJ* 110, p. 129. DOI: 10.1086/117501.

Kennicutt Jr., R. C. et al. (Oct. 2008). "An Hα Imaging Survey of Galaxies in the Local 11 Mpc Volume". In: *ApJS* 178, pp. 247–279. DOI: 10.1086/590058. arXiv: 0807.2035.

Kim, Jae-Young and Sascha Trippe (Oct. 2014). "VIMAP: an Interactive Program Providing Radio Spectral Index Maps of Active Galactic Nuclei". In: *Journal of Korean Astronomical Society* 47.5, pp. 195–199. DOI: 10.5303/JKAS.2014.47.5.195. arXiv: 1410.5141 [astro-ph.IM].

Kim, Woong-Tae and Eve C. Ostriker (May 2007). "Gravitational Runaway and Turbulence Driving in Star-Gas Galactic Disks". In: *ApJ* 660.2, pp. 1232–1245. DOI: 10.1086/513176. arXiv: astro-ph/0701755 [astro-ph].

Klessen, R. S., M. Spaans, and A.-K. Jappsen (Jan. 2007). "The stellar mass spectrum in warm and dusty gas: deviations from Salpeter in the Galactic centre and in circumnuclear starburst regions". In: *MNRAS* 374, pp. L29–L33. DOI: 10.1111/j.1745-3933.2006.00258.x. eprint: astro-ph/0610557.

Knapen, J. H. et al. (Nov. 1997). "Resolved Structure in the Nuclear Region of the Ultraluminous Infrared Galaxy Markarian 273". In: *ApJ* 490.1, pp. L29–L32. DOI: 10.1086/311015. arXiv: astro-ph/9709234 [astro-ph].

Lacki, B. C. (Oct. 2014). "The Fermi bubbles as starburst wind termination shocks." In: *MNRAS* 444, pp. L39–L43. DOI: 10.1093/mnrasl/slu107. arXiv: 1304.6137 [astro-ph.HE].

Lacki, Brian C. (June 2013). "Interpreting the low-frequency radio spectra of starburst galaxies: a pudding of Strömgren spheres". In: *MNRAS* 431.4, pp. 3003–3024. DOI: 10.1093/mnras/stt349. arXiv: 1206.7100 [astro-ph.CO].

Lacki, Brian C., Todd A. Thompson, and Eliot Quataert (July 2010). "The Physics of the Far-infrared-Radio Correlation. I. Calorimetry, Conspiracy, and Implications". In:

ApJ 717.1, pp. 1–28. DOI: 10.1088/0004-637X/717/1/1. arXiv: 0907.4161 [astro-ph.CO].

Lagache, Guilaine, Jean-Loup Puget, and Hervé Dole (Sept. 2005). "Dusty Infrared Galaxies: Sources of the Cosmic Infrared Background". In: *ARA&A* 43.1, pp. 727–768. DOI: 10.1146/annurev.astro.43.072103.150606. arXiv: astro-ph/0507298 [astro-ph].

Lambrides, Erini et al. (Feb. 2020). "A Large Population of Obscured AGN in Disguise as Low Luminosity AGN in Chandra Deep Field South". In: *arXiv e-prints*, arXiv:2002.00955, arXiv:2002.00955. arXiv: 2002.00955 [astro-ph.GA].

Leitherer, Claus et al. (July 1999). "Starburst99: Synthesis Models for Galaxies with Active Star Formation". In: *ApJS* 123.1, pp. 3–40. DOI: 10.1086/313233. arXiv: astro-ph/9902334 [astro-ph].

Lisenfeld, U. et al. (Feb. 2007). "The AMIGA sample of isolated galaxies. III. IRAS data and infrared diagnostics". In: *A&A* 462, pp. 507–523. DOI: 10.1051/0004-6361:20066144. eprint: astro-ph/0610784.

Lucek, S. G. and A. R. Bell (May 2000). "Non-linear amplification of a magnetic field driven by cosmic ray streaming". In: *MNRAS* 314, pp. 65–74. DOI: 10.1046/j.1365-8711.2000.03363.x.

Magnelli, B. et al. (Mar. 2009). "The 0.4 < z < 1.3 star formation history of the Universe as viewed in the far-infrared". In: *A&A* 496.1, pp. 57–75. DOI: 10.1051/0004-6361:200811443. arXiv: 0901.1543 [astro-ph.CO].

Magnelli, B. et al. (May 2013). "The deepest Herschel-PACS far-infrared survey: number counts and infrared luminosity functions from combined PEP/GOODS-H observations". In: *A&A* 553, A132, A132. DOI: 10.1051/0004-6361/201321371. arXiv: 1303.4436 [astro-ph.CO].

Maíz Apellániz, J. and L. Úbeda (Aug. 2005). "Numerical Biases on Initial Mass Function Determinations Created by Binning". In: *ApJ* 629, pp. 873–880. DOI: 10.1086/431458. eprint: astro-ph/0505012.

Majewski, S. R. et al. (Jan. 1993). "Subarcsecond Near-Infrared Imaging of Ultraluminous IRAS Galaxies". In: *ApJ* 402, p. 125. DOI: 10.1086/172117.

Mattila, S. et al. (Sept. 2012). "Core-collapse Supernovae Missed by Optical Surveys". In: *ApJ* 756.2, 111, p. 111. DOI: 10.1088/0004-637X/756/2/111. arXiv: 1206.1314 [astro-ph.CO].

Mattila, S. et al. (Aug. 2018). "A dust-enshrouded tidal disruption event with a resolved radio jet in a galaxy merger". In: *Science* 361.6401, pp. 482–485. DOI: 10.1126/science.aao4669. arXiv: 1806.05717 [astro-ph.GA].

McKinley, B. et al. (Mar. 2018). "The jet/wind outflow in Centaurus A: a local laboratory for AGN feedback". In: *MNRAS* 474.3, pp. 4056–4072. DOI: 10.1093/mnras/stx2890. arXiv: 1711.01751 [astro-ph.GA].

Mezger, P. G. and A. P. Henderson (Feb. 1967). "Galactic H II Regions. I. Observations of Their Continuum Radiation at the Frequency 5 GHz". In: *ApJ* 147, p. 471. DOI: 10.1086/149030.

Migenes, V. et al. (Sept. 2011). "Optical and OH megamaser observations of the starburst galaxy IIZw 096". In: *MNRAS* 416.2, pp. 1267–1273. DOI: 10.1111/j.1365-2966.2011.19124.x.

Moorwood, A. F. M. and E. Oliva (Nov. 1990). "H2 emission in galaxies : observational constraints on ultraviolet excitation." In: *A&A* 239, p. 78.

Moshir, M., G. Kopman, and T. A. O. Conrow (1992). *IRAS Faint Source Survey, Explanatory supplement version 2*.

Mudd, Dale et al. (May 2014). "XMM-Newton Observations of Three Interacting Luminous Infrared Galaxies". In: *ApJ* 787.1, 40, p. 40. DOI: 10.1088/0004-637X/787/1/40. arXiv: 1211.1674 [astro-ph.CO].

Murphy, E. J. et al. (Aug. 2011). "Calibrating Extinction-free Star Formation Rate Diagnostics with 33 GHz Free-free Emission in NGC 6946". In: *ApJ* 737.2, 67, p. 67. DOI: 10.1088/0004-637X/737/2/67. arXiv: 1105.4877 [astro-ph.CO].

Nakashima, Shinya et al. (July 2018). "Spatial Distribution of the Milky Way Hot Gaseous Halo Constrained by Suzaku X-Ray Observations". In: *ApJ* 862.1, 34, p. 34. DOI: 10.3847/1538-4357/aacceb. arXiv: 1806.04832 [astro-ph.GA].

Neff, Susan G., James S. Ulvestad, and Stacy H. Teng (Aug. 2004). "A Supernova Factory in the Merger System Arp 299". In: *ApJ* 611.1, pp. 186–199. DOI: 10.1086/383608. arXiv: astro-ph/0406421 [astro-ph].

Niklas, S., U. Klein, and R. Wielebinski (June 1997). "A radio continuum survey of Shapley-Ames galaxies at λ 2.8cm. II. Separation of thermal and non-thermal radio emission." In: *A&A* 322, pp. 19–28.

Norris, R. P. (Oct. 1985). "The nature of the megamaser galaxy IC 4553 (Arp 220)." In: *MNRAS* 216, pp. 701–711. DOI: 10.1093/mnras/216.3.701.

Pacholczyk, A. G. (1970). *Radio astrophysics. Nonthermal processes in galactic and extragalactic sources*.

Paladino, R., M. Murgia, and E. Orrù (Sept. 2009). "Radio spectral index images of the spiral galaxies NGC 0628, NGC 3627, and NGC 7331". In: *A&A* 503, pp. 747–754. DOI: 10.1051/0004-6361/200911870. arXiv: 0905.3643.

Pereira-Santaella, M. et al. (June 2010). "Local Luminous Infrared Galaxies. I. Spatially Resolved Observations with the Spitzer Infrared Spectrograph". In: *ApJS* 188, pp. 447–472. DOI: 10.1088/0067-0049/188/2/447. arXiv: 1004.1364.

Pereira-Santaella, M. et al. (Nov. 2011). "The X-ray emission of local luminous infrared galaxies". In: *A&A* 535, A93, A93. DOI: 10.1051/0004-6361/201117420. arXiv: 1109.0921 [astro-ph.CO].

Pérez-Torres, M. A., A. Alberdi, and J. M. Marcaide (Aug. 2001). "The role of synchrotron self-absorption in the late radio emission from SN 1993J". In: *A&A* 374, pp. 997–1002. DOI: 10.1051/0004-6361:20010774. arXiv: astro-ph/0106177 [astro-ph].

Pérez-Torres, M. A. et al. (Sept. 2002). "A distorted radio shell in the young supernova SN 1986J". In: *MNRAS* 335, pp. L23–L28. DOI: 10.1046/j.1365-8711.2002.05809.x. eprint: astro-ph/0202514.

Pérez-Torres, M. A. et al. (July 2005). "High-resolution observations of SN 2001gd in NGC 5033". In: *MNRAS* 360.3, pp. 1055–1062. DOI: 10.1111/j.1365-2966.2005.09102.x. arXiv: astro-ph/0504647 [astro-ph].

Pérez-Torres, M. A. et al. (Nov. 2009a). "An extremely prolific supernova factory in the buried nucleus of the starburst galaxy IC 694". In: *A&A* 507.1, pp. L17–L20. DOI: 10.1051/0004-6361/200912964. arXiv: 0909.3959 [astro-ph.CO].

Pérez-Torres, M. A. et al. (Nov. 2009b). "Radio monitoring of NGC 7469: late-time radio evolution of SN 2000ft and the circumnuclear starburst in NGC 7469". In: *MNRAS* 399, pp. 1641–1649. DOI: 10.1111/j.1365-2966.2009.15389.x. arXiv: 0907.2644.

Pérez-Torres, M. A. et al. (Sept. 2010). "Serendipitous discovery of the long-sought active galactic nucleus in Arp 299-A". In: *A&A* 519, L5, p. L5. DOI: 10.1051/0004-6361/201015462. arXiv: 1008.4466.

Pérez-Torres, Miguel et al. (Dec. 2021). "Star formation and nuclear activity in luminous infrared galaxies: an infrared through radio review". In: *A&A Rev.* 29.1, 2, p. 2. DOI: 10.1007/s00159-020-00128-x. arXiv: 2010.05072 [astro-ph.GA].

Peterson, Bradley M. and Amri Wandel (Sept. 2000). "Evidence for Supermassive Black Holes in Active Galactic Nuclei from Emission-Line Reverberation". In: *ApJ* 540.1, pp. L13–L16. DOI: 10.1086/312862. arXiv: astro-ph/0007147 [astro-ph].

Phillips, Andrew C. (Feb. 1993). "Nuclear and large-Scale Outflows in NGC 1808". In: *AJ* 105, p. 486. DOI: 10.1086/116447.

Ramírez-Olivencia, N. et al. (Mar. 2018). "Sub-arcsecond imaging of Arp 299-A at 150 MHz with LOFAR: Evidence for a starburst-driven outflow". In: *A&A* 610, L18, p. L18. DOI: 10.1051/0004-6361/201732543. arXiv: 1802.03226.

Randriamanakoto, Z. et al. (Jan. 2019). "Young massive clusters in the interacting LIRG Arp 299: evidence for the dependence of star cluster formation and evolution on environment". In: *MNRAS* 482.2, pp. 2530–2554. DOI: 10.1093/mnras/sty2837. arXiv: 1810.09897 [astro-ph.GA].

Reynolds, S. P. and R. A. Chevalier (May 1981). "Nonthermal Radiation from Supernova Remnants in the Adiabatic Stage of Evolution". In: *ApJ* 245, p. 912. DOI: 10.1086/158868.

Reynolds, Stephen P., B. M. Gaensler, and Fabrizio Bocchino (May 2012). "Magnetic Fields in Supernova Remnants and Pulsar-Wind Nebulae". In: *Space Sci. Rev.* 166.1-4, pp. 231–261. DOI: 10.1007/s11214-011-9775-y. arXiv: 1104.4047 [astro-ph.GA].

Rice, W. et al. (Oct. 1988). "A catalog of IRAS observations of large optical galaxies". In: *ApJS* 68, pp. 91–127. DOI: 10.1086/191283.

Robleto-Orús, A. C. et al. (Aug. 2020). "A MUSE study of the Seyfert 1 galaxy NGC 7469: Spatially resolved star-formation and AGN-driven winds". In: *Boletin de la Asociacion Argentina de Astronomia La Plata Argentina* 61C, pp. 66–66.

Rodríguez-González, A. et al. (Mar. 2015). "A two-mode planetary nebula luminosity function". In: *A&A* 575, A1, A1. DOI: 10.1051/0004-6361/201423713. arXiv: 1411.0986.

Romero-Cañizales, C. et al. (Aug. 2011). "The core-collapse supernova rate in Arp 299 revisited". In: *MNRAS* 415.3, pp. 2688–2698. DOI: 10.1111/j.1365-2966.2011.18886.x. arXiv: 1104.1955 [astro-ph.CO].

Rothberg, Barry et al. (Apr. 2013). "Unveiling the σ-discrepancy. II. Revisiting the Evolution of ULIRGs and the Origin of Quasars". In: *ApJ* 767.1, 72, p. 72. DOI: 10.1088/0004-637X/767/1/72. arXiv: 1302.1680 [astro-ph.CO].

Rupke, David (Dec. 2018). "A Review of Recent Observations of Galactic Winds Driven by Star Formation". In: *Galaxies* 6.4, p. 138. DOI: 10.3390/galaxies6040138. arXiv: 1812.05184 [astro-ph.GA].

Rupke, David S., Sylvain Veilleux, and D. B. Sanders (Oct. 2005a). "Outflows in Active Galactic Nucleus/Starburst-Composite Ultraluminous Infrared Galaxies1," in: *ApJ* 632.2, pp. 751–780. DOI: 10.1086/444451. arXiv: astro-ph/0507037 [astro-ph].

— (Sept. 2005b). "Outflows in Infrared-Luminous Starbursts at z < 0.5. I. Sample, Na I D Spectra, and Profile Fitting". In: *ApJS* 160.1, pp. 87–114. DOI: 10.1086/432886. arXiv: astro-ph/0506610 [astro-ph].

Rybicki, G. B. and A. P. Lightman (June 1986). *Radiative Processes in Astrophysics*, p. 400.

Sanders, D. B. and I. F. Mirabel (1996). "Luminous Infrared Galaxies". In: *ARA&A* 34, p. 749. DOI: 10.1146/annurev.astro.34.1.749.

Sanders, D. B. et al. (Feb. 1988). "Ultraluminous Infrared Galaxies and the Origin of Quasars". In: *ApJ* 325, p. 74. DOI: 10.1086/165983.

Sanders, D. B. et al. (Oct. 2003). "The IRAS Revised Bright Galaxy Sample". In: *AJ* 126, pp. 1607–1664. DOI: 10.1086/376841. eprint: astro-ph/0306263.

Schure, K. M. et al. (Nov. 2012). "Diffusive Shock Acceleration and Magnetic Field Amplification". In: *Space Sci. Rev.* 173.1-4, pp. 491–519. DOI: 10.1007/s11214-012-9871-7. arXiv: 1203.1637 [astro-ph.HE].

Scoville, N. Z. et al. (Mar. 2000). "NICMOS Imaging of Infrared-Luminous Galaxies". In: *AJ* 119.3, pp. 991–1061. DOI: 10.1086/301248. arXiv: astro-ph/9912246 [astro-ph].

Seo, Woo-Young et al. (Feb. 2019). "Effects of Gas on Formation and Evolution of Stellar Bars and Nuclear Rings in Disk Galaxies". In: *ApJ* 872.1, 5, p. 5. DOI: 10.3847/1538-4357/aafc5f. arXiv: 1901.02021 [astro-ph.GA].

Shklovskii, I. S. (Oct. 1960). "Secular Variation of the Flux and Intensity of Radio Emission from Discrete Sources". In: *Soviet Ast.* 4, p. 243.

Smith, Beverly J. et al. (Apr. 1994). "Far-Infrared Emission from the Bulges of Early-Type Spirals: KAO Observations of NGC 4736 (M94) and NGC 3627 (M66)". In: *ApJ* 425, p. 91. DOI: 10.1086/173965.

Soifer, B. T. et al. (Feb. 2000). "High Resolution Mid-Infrared Imaging of Ultraluminous Infrared Galaxies". In: *AJ* 119.2, pp. 509–523. DOI: 10.1086/301233. arXiv: astro-ph/9911045 [astro-ph].

Soifer, B. T. et al. (July 2003). "High Spatial Resolution Mid-Infrared Observations of Three Seyfert Galaxies". In: *AJ* 126.1, pp. 143–152. DOI: 10.1086/375647. arXiv: astro-ph/0304105 [astro-ph].

Su, Kung-Yi et al. (Jan. 2020). "Cosmic rays or turbulence can suppress cooling flows (where thermal heating or momentum injection fail)". In: *MNRAS* 491.1, pp. 1190–1212. DOI: 10.1093/mnras/stz3011. arXiv: 1812.03997 [astro-ph.GA].

Su, Kung-Yi et al. (Feb. 2021). "Which AGN Jets Quench Star Formation in Massive Galaxies?" In: *arXiv e-prints*, arXiv:2102.02206, arXiv:2102.02206. arXiv: 2102.02206 [astro-ph.GA].

Su, Meng, Tracy R. Slatyer, and Douglas P. Finkbeiner (Dec. 2010). "Giant Gamma-ray Bubbles from Fermi-LAT: Active Galactic Nucleus Activity or Bipolar Galactic Wind?" In: *ApJ* 724.2, pp. 1044–1082. DOI: 10.1088/0004-637X/724/2/1044. arXiv: 1005.5480 [astro-ph.HE].

Telesco, C. M., R. Decher, and I. Gatley (Dec. 1985). "Near-infrared mapping of ARP 299 (IC 694-NGC 3690) - Colliding galaxies unveiled". In: *ApJ* 299, pp. 896–904. DOI: 10.1086/163756.

Telles, Eduardo and Roberto Terlevich (July 1995). "The environment of HII galaxies". In: *MNRAS* 275.1, pp. 1–8. DOI: 10.1093/mnras/275.1.1. arXiv: astro-ph/9501084 [astro-ph].

Thompson, T. A., E. Quataert, and N. Murray (Aug. 2009). "Radio emission from supernova remnants: implications for post-shock magnetic field amplification and the magnetic fields of galaxies". In: *MNRAS* 397, pp. 1410–1419. DOI: 10.1111/j.1365-2966.2009.14889.x. arXiv: 0902.1755 [astro-ph.HE].

Thompson, T. A. et al. (July 2006). "Magnetic Fields in Starburst Galaxies and the Origin of the FIR-Radio Correlation". In: *ApJ* 645, pp. 186–198. DOI: 10.1086/504035. eprint: astro-ph/0601626.

Thornton, K. et al. (June 1998a). "Energy Input and Mass Redistribution by Supernovae in the Interstellar Medium". In: *ApJ* 500.1, pp. 95–119. DOI: 10.1086/305704. arXiv: astro-ph/9706175 [astro-ph].

— (June 1998b). "Energy Input and Mass Redistribution by Supernovae in the Interstellar Medium". In: *ApJ* 500.1, pp. 95–119. DOI: 10.1086/305704. arXiv: astro-ph/9706175 [astro-ph].

U, Vivian et al. (Oct. 2013). "The Inner Kiloparsec of Mrk 273 with Keck Adaptive Optics". In: *ApJ* 775.2, 115, p. 115. DOI: 10.1088/0004-637X/775/2/115. arXiv: 1307.8440 [astro-ph.CO].

Ulvestad, James S. (Nov. 2009). "Radio Emission from Young Supernovae and Supernova Remnants in Arp 299". In: *AJ* 138.5, pp. 1529–1538. DOI: 10.1088/0004-6256/138/5/1529. arXiv: 0909.3534 [astro-ph.CO].

van den Bergh, S., R. D. McClure, and R. Evans (Dec. 1987). "The supernova rate in Shapley-Ames galaxies". In: *ApJ* 323, pp. 44–53. DOI: 10.1086/165806.

van Dyk, S. D., M. Hamuy, and A. V. Filippenko (May 1996). "Supernovae and Massive Star Formation Regions". In: *AJ* 111, p. 2017. DOI: 10.1086/117937.

van Haarlem, M. P. et al. (Aug. 2013). "LOFAR: The LOw-Frequency ARray". In: *A&A* 556, A2, A2. DOI: 10.1051/0004-6361/201220873. arXiv: 1305.3550 [astro-ph.IM].

Varenius, E. et al. (Feb. 2015). "Subarcsecond international LOFAR radio images of the M82 nucleus at 118 MHz and 154 MHz". In: *A&A* 574, A114, A114. DOI: 10.1051/0004-6361/201425089. arXiv: 1411.7680 [astro-ph.GA].

Varenius, E. et al. (Sept. 2016). "Subarcsecond international LOFAR radio images of Arp 220 at 150 MHz. A kpc-scale star forming disk surrounding nuclei with shocked outflows". In: *A&A* 593, A86, A86. DOI: 10.1051/0004-6361/201628702. arXiv: 1607.02761 [astro-ph.GA].

Varenius, E. et al. (Mar. 2019). "The population of SNe/SNRs in the starburst galaxy Arp 220. A self-consistent analysis of 20 years of VLBI monitoring". In: *A&A* 623, A173, A173. DOI: 10.1051/0004-6361/201730631. arXiv: 1702.04772 [astro-ph.GA].

Veilleux, Sylvain, Gerald Cecil, and Joss Bland-Hawthorn (Sept. 2005). "Galactic Winds". In: *ARA&A* 43.1, pp. 769–826. DOI: 10.1146/annurev.astro.43.072103.150610. arXiv: astro-ph/0504435 [astro-ph].

Vink, J. (Dec. 2008). "Multiwavelength Signatures of Cosmic Ray Acceleration by Young Supernova Remnants". In: *American Institute of Physics Conference Series*. Ed. by F. A. Aharonian, W. Hofmann, and F. Rieger. Vol. 1085. American Institute of Physics Conference Series, pp. 169–180. DOI: 10.1063/1.3076632. arXiv: 0810.3680.

Voelk, H. J., L. O. Drury, and J. F. McKenzie (Jan. 1984). "Hydrodynamic estimates of cosmic ray acceleration efficiencies in shock waves". In: *A&A* 130, pp. 19–28.

Wang, Jing et al. (Jan. 1997). "An X-Ray and Optical Investigation of the Infrared-luminous Galaxy Merger Markarian 266". In: *ApJ* 474.2, pp. 659–674. DOI: 10.1086/303499.

Wang, Wei-Hao et al. (July 2001). "Gas Distribution and Starburst Activity in the Widely Separated Interacting Galaxy Pair NGC 6670". In: *AJ* 122.1, pp. 140–162. DOI: 10.1086/321112. arXiv: astro-ph/0103280 [astro-ph].

Watson, A. M. et al. (Aug. 1996). "The Discovery of Young, Luminous, Compact Stellar Clusters in the Starburst Galaxy NGC 253". In: *AJ* 112, p. 534. DOI: 10.1086/118032.

Woosley, S. E. and J. S. Bloom (Sept. 2006). "The Supernova Gamma-Ray Burst Connection". In: *ARA&A* 44, pp. 507–556. DOI: 10.1146/annurev.astro.43.072103.150558. eprint: astro-ph/0609142.

Yun, Min S., Naveen A. Reddy, and J. J. Condon (June 2001). "Radio Properties of Infrared-selected Galaxies in the IRAS 2 Jy Sample". In: *ApJ* 554.2, pp. 803–822. DOI: 10.1086/323145. arXiv: astro-ph/0102154 [astro-ph].

"Si contemplo el cielo, obra de tus manos,
la Luna y las estrellas que has creado,
¿qué es el hombre para que te acuerdes de él,
el ser humano para darle poder?
Sal 8, 4s "